Constrained segmentation of cardiac MR image sequences

Üzümcü, M.

Constrained Segmentation of Cardiac MR Image Sequences

Colophon

This thesis was typeset by the author using LaTeX2$_\epsilon$. The text was set using a 10 points Palatino font (© Adobe Systems Inc.). Images were included formatted as Encapsulated Postscript. The output was converted to PDF and transferred to film for printing.

About the quotes
The texts on the titlepages of each chapter are quotes from Mevlana Celâleddin Rumi (1207 - 1273). Mevlana (*'Our guide'*) is a Turkish mystic of Islam, philosopher and poet, who lived in the city Konya in central Anatolia. The text on the titlepage of chapter 1 is taken from his most famous poem. The texts on the titlepages of the remaining 7 chapters are known as the *Seven Advices of Mevlana*.
Mevlana addressed people of all religions and ethnic origins and advocated unlimited tolerance, positive reasoning, goodness and awareness through love. In honour of his 800^{th} birthday, UNESCO has declared 2007 the 'Year of Mevlana Rumi'.

About the cover
The front and back covers were designed by Sandra Batelaan. The covers show an abstraction of the cost matrix used in the Multidimensional Dynamic Programming based method in chapter 6. When the front and back covers are seen together, a connective path that gets darker from left to right is observed, which represents an optimal path with increasing cumulative cost. Corresponding segmentation results are shown within the tiles. From left to right a time-continuous segmentation of the cardiac left ventricle from ED to ES phase is shown.

Constrained Segmentation of Cardiac MR Image Sequences
Üzümcü, Mehmet

Printed by: Universal Press, Veenendaal, The Netherlands
ISBN 978-90-9022186-1

Constrained Segmentation of Cardiac MR Image Sequences

PROEFSCHRIFT

ter verkrijging van

de graad van Doctor aan de Universiteit Leiden,

op gezag van Rector Magnificus prof.mr. P.F. van der Heijden,

volgens besluit van het College voor Promoties

te verdedigen op woensdag 12 september 2007

klokke 16.15 uur

door

Ir. Mehmet Üzümcü
geboren te Breda
in 1976

Promotiecommissie

promotor:	Prof. dr. ir. J.H.C. Reiber
co-promotor:	Dr. ir. B.P.F. Lelieveldt
referent:	Prof. dr. A.M. Vossepoel
	Erasmus Universiteit Rotterdam
overige leden:	Prof. dr. A. de Roos
	Ir. R.J. van der Geest
	Dr. A.F. Frangi
	Universitat Pompeu Fabra, Barcelona, Spanje

The research described in this thesis was financially supported by IOP (Innovative Research Program of The Netherlands), grant IOP-BV00303

Financial support for the publication of this thesis was kindly provided by:
Nucletron B.V.
Stichting Beeldverwerking Leiden
Medis *medical imaging systems* B.V.
Foundation Imago Oegstgeest

Contents

1

Introduction

Come, come again, whoever you are, come!
Heathen, fire worshipper or idolatrous, come!
Come even if you broke your penitence a hundred times,
Ours is the portal of hope, come as you are.

1.1 Background

Cardiovascular diseases (CVD) are the number one cause of death in the western world. According to the European Heart Network, over 4 million deaths in Europe and nearly 2 million deaths in the European Union occur due to causes related to cardiovascular diseases [1]. This accounts for nearly 50% of natural deaths in Europe. According to the American Heart Association [2], in the U.S.A. CVD was an underlying or contributing cause of death in an estimated 1.4 million people in the year 2002, which accounted for 58% of all deaths in that year. Almost 60 million Americans, i.e. 25% of the population, suffer from some form of heart disease.

Major types of cardiovascular disease are coronary heart disease (CHD), arrhythmia, acute myocardial infarction (MI or heart attack) and congestive heart failure (CHF). The next section briefly describes cardiac physiology and function, after which the above-mentioned types of CVD are explained.

1.2 Cardiac physiology

The heart is a muscular organ with specialized cells for automaticity of contraction and electrical conduction [3]. It is located in the center of the chest, between the lungs, and has the size of a closed fist. The apex of the heart - the lower end - is tilted slightly towards the left. Despite the relatively small size of the heart, 5 to 6 liters of blood can be pumped per minute.

The heart consists of four chambers (see Fig. 1.1), two atria and two ventricles. Deoxygenated blood enters the right atrium. When the right atrium is filled, it injects the blood into the right ventricle, which in turn contracts and pumps the blood into the pulmonary circulation. In the lungs, carbon dioxide and water are excreted from the blood and oxygen is absorbed. Oxygenated blood returns to the left atrium and is injected into the left ventricle through the bicuspid or mitral valve. Next, blood is pumped into the aorta and the systemic circulation, i.e. the rest of the body.

The cardiac contraction cycle is triggered by an electrical pulse in the sino-atrial node, which propagates through the heart through a dedicated electrical conduction system: the His - Purkinje system. This controlled propagation causes an alternating pattern of phases of diastole and systole of each chamber. In the end-diastolic phase, the chambers are maximally relaxed and filled with blood. In the end-systolic phase, the chambers are maximally contracted and most of the blood is ejected. The rate of the contractions is influenced by neural stimuli and hormones. The coronary system supplies the heart muscle itself with oxygen and nutrients, whereas the valves ensure a unidirectional flow through the different compartments in the heart.

Since the cardiac contraction is an intricate balance of electrical signal propagation, muscle contraction, muscle perfusion and valves opening and closing, a disturbance in one of these elements may affect other functions. This may cause the following main types of cardiac pathologies.

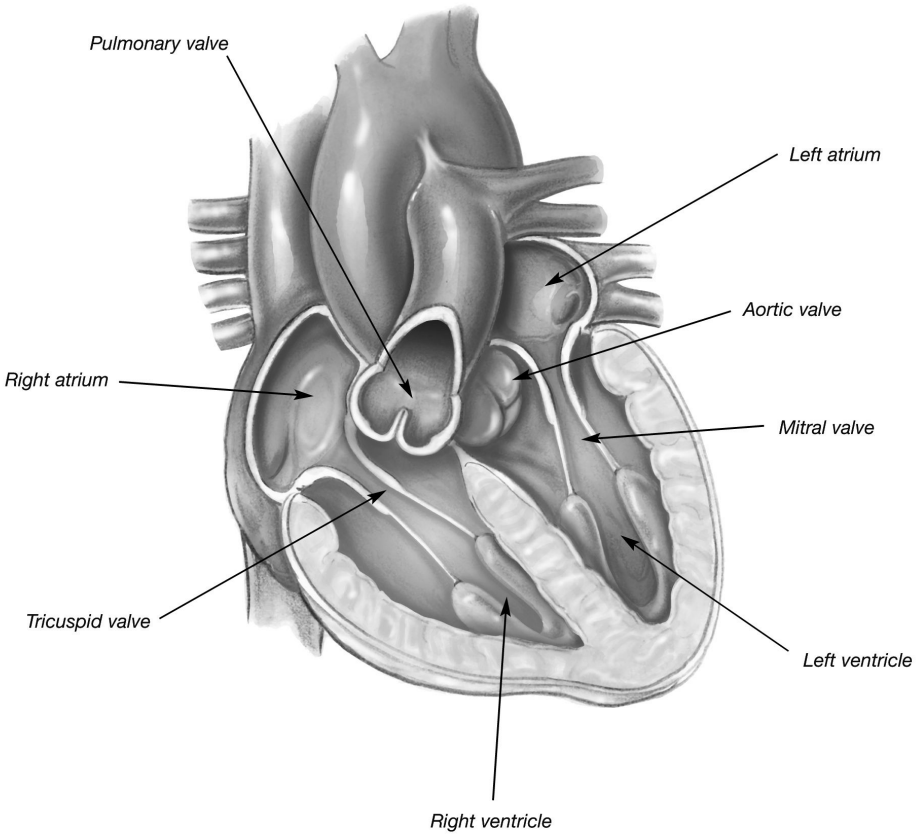

Figure 1.1: Cross Section of the human heart. (© Edwards Lifesciences Corporation)

Coronary heart disease (CHD) is caused by narrowing of the coronary arteries that perfuse the cardiac muscle. When the coronary arteries are narrowed or clogged by cholesterol and fat deposits (atherosclerosis), the supply of oxygenated blood to the heart muscle is insufficient, causing myocardial ischemia, particularly at exercise. If blood supply to a part of the heart is completely cut off by total blockage of a coronary artery, a heart attack occurs.

Arrhythmias are abnormalities in the electrical activation of the heartbeat. They can be caused by several factors such as a previous myocardial infarction, nerve conduction blocks in the His - Purkinje system, or pulses originating from ectopic locations outside the sino-atrial node. Examples of arrhythmias are: a too high heart rate due to re-entrant currents looping around the ventricles (tachycardia), a too low heart rate due to a conduction block (bradycardia) and an irregular heart rate due to ectopic stimulation.

A *myocardial infarction* (MI) is defined as death (necrosis) of myocardial cells and occurs due to myocardial ischemia. Ischemia is a result of increased demand for

and/or decreased delivery of oxygen. An increased myocardial demand for oxygen may be caused by an extreme physical effort or severe hypertension. Decreased delivery of oxygenated blood to the myocardium is in general caused by coronary heart diseases. Ischemia exceeding a critical threshold for an extended period of time yields irreversible myocardial cell damage or death.
Valve dysfunction may cause retrograde flow in the heart, which reduces the effectiveness of the cardiac contraction. Also, the increased pressure on the atria during systole may cause structural changes in the heart, and eventually even heart failure. Valve dysfunction may be caused by e.g. stenoses, inflammation or tumor growth.
Congestive heart failure (CHF) reflects the inefficiency of the cardiac function due to a complex of causes, such as hypertension or combinations of the aforementioned conditions. In CHF patients, the cardiac output is decreased, i.e. the heart is not effective in pumping sufficient oxygenated blood to meet the metabolistic demand.

1.3 Relevant clinical parameters

There is an increasing demand for a quantitative assessment of cardiac function, and several indicators are considered relevant in the analysis of cardiac function. These parameters can be divided in two categories: local and global parameters. Local parameters refer to a pathology that occurs in a specific region of the myocardium, whereas global parameters describe overall cardiac function. As described above, blood is pumped into the systemic circulation by the left ventricle of the heart. Therefore, the left ventricle is most important for cardiac function and the parameters that are described below are related to the left ventricle. Examples of global parameters are the following:
The *end-diastolic (ED)* and *end-systolic (ES)* volumes are the ventricular volumes when the ventricle is maximally filled with blood and when the ventricle is maximally contracted, respectively. The *Stroke Volume (SV)* is defined as the difference between the ED and ES volumes of the ventricle. The *Ejection Fraction (EF)* is the relative difference in volumes in end-diastolic and end-systolic phases and one of the most frequently used clinical parameters in cardiac function analysis. *Peak ejection rate* is the steepest downward slope in the volume curve, and represents the effectiveness of the contraction, i.e. the systolic function. *Peak filling rate* is the steepest slope upward in the volume curve, and describes the diastolic function of the ventricles (Fig. 1.2).
The following parameters describe cardiac function in a specific region: *Wall thickness* is the thickness of the cardiac muscle (myocardium). Figure 1.3 shows an MR image of the cardiac left ventricle. The endocardial border is the inside wall of the ventricle and the epicardial border is the outside edge of the ventricle. The muscle between the endo- and epicardial borders is the myocardium. The wall thickness parameter describes the thickness of the cardiac muscle in a specific region. *Wall thickening* is the difference between end-systolic and end-diastolic wall thickness.

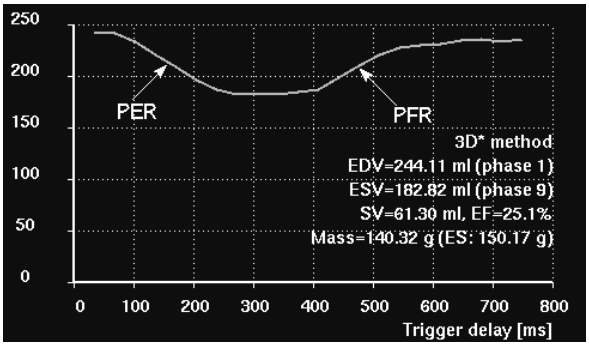

Figure 1.2: Volume curve of left ventricle. The PER and PFR are annotated.

This expresses the ability of the myocardial muscle to contract in a specific region. The value of this parameter is reduced at the site of an infarction. The *wall motion* is a robust indicator of cardiac function. When necrosis exists in a specific region of the myocardium, no contraction of the cardiac muscle occurs and therefore, the cardiac wall in this region does not move as seen in healthy subjects. Little residual motion can be observed in the infarcted area due to the contraction of the healthy myocardium. Wall motion can be classified as hypo-functional (less than normal), hyper-functional (more than normal), a-functional (no motion) and dysfunctional (in the opposite direction of the rest of the myocardium) motion. The *infarct transmurality* is the extent of necrosis through the myocardial wall; this is an important indicator of the viability of the damaged cardiac muscle. A transmural MI is characterized by necrosis of the full thickness of the myocardial segment(s), extending from the endocardium through the myocardium towards the epicardium. In case of a non-transmural MI, the area of ischemic necrosis does not extend through the full thickness of the myocardial wall. An infarcted wall segment with a transmurality less than 50% of the myocardial wall thickness is clinically considered as viable, i.e. the effects of the MI are reversible.

1.4 Cardiac magnetic resonance imaging

One of the most versatile and accurate methods to quantitatively assess cardiac function is Magnetic Resonance Imaging (MRI). MRI was clinically introduced in the early 1980's, and is based on the fact that biological tissues mainly consists of water molecules, which contain protons. When a subject is placed in a strong magnetic field, the small magnetic fields caused by the proton spins, which are distributed randomly, align with the applied magnetic field. They align both parallel and anti-parallel to the magnetic field, with a slight surplus anti-parallel, resulting in a net magnetization in the order of one per million, according to Boltzmann statistics for the difference in energy between the parallel and anti-parallel states.

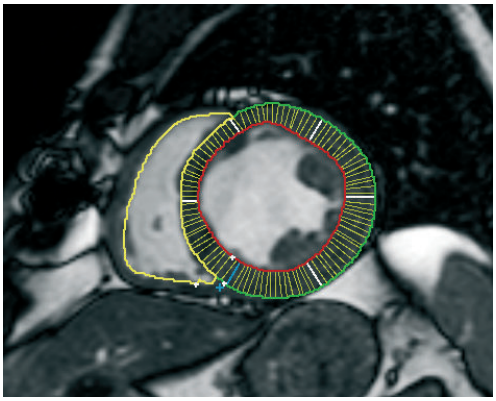

Figure 1.3: Short axis MR image of the left ventricle. The endo- and epicardial contours of the left ventricle and the right ventricular contour are shown.

By applying pulses in the radio-frequency (RF) range, the alignment of the protons is disturbed. During relaxation, the precession of the net magnetization in the static field generates signals that can be measured externally, from which images can be reconstructed. The relaxation time and amplitude of the signals depend on the tissue type, and are different for e.g. fat, muscular tissue, etc. By altering the timing of the applied pulses, different tissue types and structures can be emphasized, and imaged with high quality. A major advantage of MRI over other imaging modalities is the possibility of visualizing soft tissues, e.g. the heart, the brain, kidneys, lungs, etc. A more detailed account of the physics of MRI can be found in [4].

MRI enables acquisition of two-dimensional sectional images under any orientation (short axis view, long axis view, sagittal, transversal, coronal, etc), three-dimensional volumetric images and four-dimensional images representing spatial-spectral distributions. Unlike CT, where radiation is transmitted through the subject's body (transmission tomography), MRI is a form of emission tomography, i.e. the signals originate from within the subject. Contrary to other emission tomography techniques such as PET and SPECT, which require the injection of radioactive isotopes into the subject, magnetic resonance images are reconstructed from signals that are in the radio-frequency (RF) range. MRI is therefore a non-invasive imaging modality, i.e. injection of contrast media is not needed for the standard acquisition procedures and ionizing radiation is not involved in the image acquisition. Therefore, no harmful side effects are associated with this technique during or after image acquisition.

Due to cardiac motion, image blurring occurs when acquisition requires more than 50 ms in systole and more than 200 ms in diastole phase of the cardiac cycle. Acquiring a complete image in these time frames is only possible with ultra-fast MR techniques. To minimize motion artifacts, generally cardiac gating is applied in the acquisition of cardiac MR images. Using gating, the MR acquisition can be timed to cardiac physiological motion, by synchronizing the beginning of the relaxation of the

proton spins with a cardiac trigger, which is obtained by means of an ECG. This way, a limited number of lines in k-space is acquired per cardiac cycle and image information is accumulated over multiple cardiac cycles for imaging one cardiac phase. This enables 4D image acquisition, i.e. Cine MRI, which allows for a temporal analysis of cardiac function. More details on cardiac MR protocols can be found in [5].
MRI enables imaging and visualization of cardiac anatomy and morphology, from which information about cardiac function and physiology can be derived. Both the global and regional parameters elaborated above can be determined with cardiac MRI, therefore in recent years MRI has developed into one of the most accurate and reliable imaging modalities for quantitative cardiac analysis.

1.5 Model-based segmentation

MR images are intrinsically acquired three-dimensionally. Acquisition is performed slice by slice and the tissue is sampled into voxels (volume elements). Volumetric imaging modalities such as MRI and CT produce large amounts of patient data; a typical acquisition consists of ± 1000 images. However, both anatomical and functional information can be obtained this way.
Imaging and visualization only, however, are not sufficient to quantitate cardiac function. Image processing is needed to perform measurements in the images. Specifically in case of cardiac function analysis, contours of the myocardium are required to determine the above described clinically relevant parameters. In general, the contours are drawn manually and due to the large size of the datasets, this is a time-consuming, tedious and also subjective task.
One of the goals of medical image processing is to provide tools and methods for automation of measurement in digital images, to increase understanding of medical images and to classify and detect abnormalities. Important criteria for evaluation of these tools are accuracy, degree of automation, robustness, reproducibility and objectivity. Low-level image processing techniques, such as thresholding and region growing, generally do not meet the above-mentioned criteria. In the medical domain, prior knowledge about the organ of interest is often essential to reach the robustness required for clinical practice. This can be knowledge about the organ shape, intensity, but also the specific motion of the heart.
This thesis investigates different methods for automatic segmentation of cardiac contours in volumetric image datasets. It builds upon a previously developed method to integrate such prior knowledge into the segmentation: the so-called Active Appearance Models (AAMs). These models were introduced by Cootes *et al.* [6, 7] and have been applied to a variety of image segmentation problems, such as facial recognition. AAMs are statistical models, built upon the Point Distribution Models (PDMs) and Active Shape Models (ASMs), which were introduced by Cootes in [8].
PDMs describe statistical variations seen in the location of landmark points and no information of the underlying image data is modeled. The ASM is an extension of

the point distribution model, as it also takes into account the distribution of grey values surrounding landmark points, which are sampled on scanlines perpendicular to the contours. ASMs are successful in finding strong edges, however, because little information on the grey values is used, ASMs may lock onto false edges and are not sufficiently robust. In case of the AAM, a solid intensity patch within and surrounding a shape is modeled. Furthermore, artificial images can be generated with AAMs, which resemble real images. The least squares error between the images generated by the model and the real images can be used as a measure of goodness of fit. Because AAMs are trained on a dataset containing example images and contours, they intrinsically incorporate prior knowledge about shape and texture, making AAMs more robust for finding weak edges. They have shown to be very useful in medical image processing [9, 10].

However, Active Appearance Models have two distinct limitations. Traditionally, AAMs use Principal Component Analysis (PCA) to describe the shape variations in the training dataset. PCA finds a set of basis vectors - eigenvectors - along which the variance is maximal. These eigenvectors are used to describe the variation as seen in the examples. As a consequence of variance maximization, eigenvectors corresponding to high eigenvalues describe more information and the amount of information described by each eigenvector decreases for decreasing eigenvalues. Eigenvectors with lowest eigenvalues describe noise. This way, a dimension reduction can be achieved by discarding the eigenvectors that describe noise and the variation in the data can be mapped to a more compact space. However, as the goal of PCA is to achieve maximum compactness, the resulting eigenvectors describe global shape changes, especially when a relatively small number of examples is available. Therefore, AAMs are able to yield globally good segmentations; however local segmentation inaccuracies may occur, because the model does not cover the localized shape details. Furthermore, AAMs are less suitable for segmentation of the full cardiac cycle. The main reason for this is the fact that a large training dataset is required, with expert drawn manual annotations. Due to the large amount of contours required to construct such a sufficiently representative model, application to the full cardiac cycle is impractical.

1.6 Scope of thesis

As mentioned above, AAMs have shown great potential for medical image segmentation tasks, however, they have a few limitations. In this thesis, we explore different ways to improve the AAM framework, and to develop segmentation methods for application on cardiac image sequences. The goal of the research described in this thesis is threefold:

- Improvement of the local segmentation accuracy of AAMs by exploring alternative, locally more accurate decompositions of the training data

- Increasing the segmentation robustness by integrating redundant and complementary information from different views and time frames
- Developing a less training-intensive segmentation algorithm for time-continuous segmentation of the full cardiac cycle

In this thesis, we focused on cardiac MR imaging; however, many of the concepts presented here are applicable to other cardiac imaging modalities. Also, this thesis mainly deals with the left cardiac ventricle, although there are no fundamental obstacles for application of the developed methods to other cardiac structures.

1.7 Thesis outline

This thesis consists of seven chapters, five of which are based on articles that have been published in international journals and conference proceedings. Each chapter is self-contained and therefore, some overlap between chapters may exist. This thesis is further organized as follows.
Chapter 2 explores the use of Independent Component Analysis for describing shape variations in Statistical Shape Models. The focus of this chapter is on the evaluation of several methods for computing ICA and presents a comparison of these methods. Principal Component Analysis results in an ordered set of eigenvectors, in which vectors describing more information are placed first and vectors describing noise are placed last. ICA, however, results in Independent Components, which cannot be sorted in the same way as eigenvectors. In this chapter several sorting criteria are evaluated to address this problem.
Chapter 3 describes the implementation of ICA in the Active Appearance Model framework. A sorting method based on the local nature of shape variations obtained with ICA is introduced and an extensive comparison of the segmentation performance of PCA and ICA is presented.
Chapter 4 explores the use of model parameters for diagnosis of cardiac motion abnormalities. An ICA based shape model was trained on healthy subjects and the corresponding model parameters were stored. When images of patients and healthy subjects are mapped onto the model vectors, the patients can be separated by viewing the model parameters. Sorting the Independent Components according to the location of shape variations that they describe enabled also the localization of the infarcted regions.
Chapter 5 presents a method for extending the Active Appearance Models by including information from different views. In this chapter, a method is proposed to enable rapid on-line assessment of relevant clinical parameters, such as end-diastolic and end-systolic volumes and ejection fractions. Images from 2- and 4-chamber long axis views in end-diastolic and end-systolic phases were coupled and an AAM was trained on the combination of these two views and two time frames. Experimental results from 59 patients are presented, demonstrating the potential of the Multi-view

Active Appearance Model for rapid evaluation of cardiac function from standardized MR views.
Chapter 6 describes time-continuous segmentation of a full cycle of 3-D cardiac short axis MR images using Multi-dimensional Dynamic Programming. In this chapter also an application of the presented method is shown for time-continuous tracking of the aorta to perform flow measurements. Results of quantitative experiments on 20 patients and qualitative experiments on one healthy subject are presented to demonstrate the applicability of this method for both time-continuous left ventricular volume calculation and aorta tracking.
Finally, in Chapter 7 conclusions and directions for further research are presented.

References

[1] British Heart Foundation Health Promotion Research Group, European Cardiovascular Disease Statistics 2005 Edition, Univ. of Oxford, Oxford, U.K. Online available:
http://www.heartstats.org/uploads/documents/PDF.pdf

[2] Heart Disease and Stroke Statistics - 2006 Update, Circulation, American Heart Association, Dallas, Texas. Online available:
http://circ.ahajournals.org

[3] B.R. Wilcox, A.C. Cook, R.H. Anderson, Surgical Anatomy of the Heart, Cambridge University Press, Cambridge, U.K., 2004. ISBN: 1841100285

[4] M. A. Vlaardingerbroek, J.A. den Boer, Magnetic Resonance Imaging, 2nd edition, ISBN 978-3-540-43681-2, Springer, Germany, 2000

[5] J. P. Finn, K. Nael, V. Deshpande, O. Ratib, and G. Laub, Cardiac MR Imaging: State of the Technology, Radiology, November 1, 2006; 241(2): 338–354

[6] T.F. Cootes, G.J. Edwards, C.J. Taylor, Active Appearance Models, Proceedings of the European Conference on Computer Vision, (2): 484–498, 1998

[7] G. Edwards, C. Taylor, T. Cootes, Interpreting face images using active appearance Models, Proceedings of the Third IEEE International Conference on Automatic Face and Gesture Recognition, 300–305, 1998

[8] T.F. Cootes, D. Cooper, C.J. Taylor and J. Graham, Active Shape Models - Their Training and Application. Computer Vision and Image Understanding. 61(1): 38–59, 1995

[9] S. C. Mitchell, B. P. F. Lelieveldt, R. J. van der Geest, J. G. Bosch, J. H. C. Reiber, and M. Sonka, Multistage Hybrid Active Appearance Model Matching: Segmentation of Left and Right Cardiac Ventricles in Cardiac MR Images, IEEE Transactions on Medical Imaging, 20(5): 415–423, 2001

[10] C.R. Oost, G. Koning, M. Sonka, P.V. Oemrawsingh, J.H.C. Reiber, B.P.F. Lelieveldt, Automated Segmentation of X-Ray Left Ventricular Angiograms using Multi-View Active Appearance Models, IEEE Transactions on Medical Imaging, 25(9): 1158–1171, 2006

2

Independent Component Analysis in Statistical Shape Models

In generosity and helping others be like a river

This chapter was adapted from:
Independent Component Analysis in Statistical Shape Models
M. Üzümcü, A.F. Frangi, J.H.C. Reiber, B.P.F. Lelieveldt
In: Proceedings of SPIE, Medical Imaging 2003: Image Processing, Eds: Milan Sonka, J. Michael Fitzpatrick, vol. 5032:375 – 383, 2003

Abstract

Statistical shape models generally use Principal Component Analysis (PCA) to describe the main directions of shape variation in a training set of example shapes. However, PCA assumes a number of restrictions on the data that do not always hold. In this paper we explore the use of an alternative shape decomposition, Independent Component Analysis (ICA), which does not assume a Gaussian distribution of the input data. Several different methods for performing ICA are available. Three most frequently used methods were tested in order to evaluate their effect on the resulting vectors. In statistical shape models, generally not all the eigenvectors that result from the PCA are used. Vectors describing noise are discarded to obtain a compact description of the dataset. The selection of these vectors is based on the natural ordering of the vectors according to the variance in that direction, which is inherent to PCA. With ICA, however, there is no natural ordering of the vectors. Four methods for sorting the ICA vectors are investigated. The different ICA-methods yielded highly similar yet not identical results. Vectors obtained with ICA showed localized shape variations, whereas eigenvectors obtained with PCA show global shape variations. From the results of the ordering methods can be seen that PCA is better suited for dimensionality reduction. Of the ordering methods that were tested, the best results were obtained with the ordering according to the locality of the shape variations.

2.1 Introduction

Statistical shape models such as Active Shape Models (ASM) [1] or Active Appearance Models (AAM) [2] have shown great potential in image recognition and segmentation tasks [3, 4, 5]. Such models generally use Principal Component Analysis to describe the main directions of shape variation in a training set of example shapes. However, PCA assumes that the data is normally distributed, which frequently is not the case. This may lead to a wrong description of the dataset and result in shapes that are not plausible and in some cases cannot generate shapes that are desired. We have investigated the use of an alternative shape decomposition technique, Independent Component Analysis, which does not assume a Gaussian distribution of the input data, and therefore potentially resolves these problems.

Independent Component Analysis produces statistically independent non-Gaussian components by de-correlating higher order moments in addition to the first- and second-order moments of the statistical distribution. Several different methods for calculating ICA exist, such as e.g. the FastICA [6], the InfoMax [7] and the JADE [8] algorithm. These methods differ in the optimized contrast function to achieve decorrelation. The above mentioned methods were tested in order to make a comparison, which is independent of the method that is used.

In classical PCA, one is able to define a natural ordering of the eigenvectors according to the associated eigenvalues (variances). Therefore, it is possible to obtain a

compact description of the shape set by discarding the eigenshapes describing the least variance (noisy components). In Independent Component Analysis however, the directions are known to be descriptive of independent factors but the method itself does not rank the components. This makes it difficult to achieve dimensionality reduction unless, as customarily, one first performs PCA [11].
In this work, we have developed and evaluated several methods for ordering the independent components according to intuitive criteria. The main contribution of this work is the application of Independent Component Analysis on several sets of shapes, the comparison of different ICA-methods and the analysis of various methods for ordering the independent components.
This chapter is organized as follows. In Section 2 a summary of statistical shape models, such as the Point Distribution Models is given. In Section 3, Independent Component Analysis methods will be explained, as well as the different sorting methods that were considered. In Section 4 the results obtained with the different optimization methods for ICA and results of the comparison between different sorting methods is presented, followed by a discussion and conclusions in Section 5.

2.2 Point Distribution Models

Statistical Models for image processing, such as the Active Shape Model and the Active Appearance Model were introduced by Cootes et al. [1, 2], and can be applied to image segmentation in various domains [3, 4, 5]. These models describe statistical variations as seen in a set of example images, in which corresponding landmark points are annotated. The shapes, which are spanned by the landmarks, are aligned using Procrustes analysis to compensate for translation, rotation and scaling differences between the shape samples by minimizing the squared distance between corresponding points in the shape samples. The mean shape of this set of aligned shapes is calculated, and modes of shape variation are computed using PCA.
Each shape sample can then be expressed by means of a set of shape coefficients b_s as follows:

$$x \approx \bar{x} + Q_s \cdot b_s \tag{2.1}$$

where x is a generated shape sample, $\bar{x}$ the mean shape, Q_s is the matrix with eigenvectors describing the modes of shape variation in the training set and b_s is the vector that contains the coefficients weighting those eigenvectors.
As mentioned in the previous section, Principal Component Analysis is used to derive the main directions of variation in the dataset. PCA assumes that the input data is drawn from a multidimensional Gaussian distribution, which in practice tends to be an oversimplification. Therefore, we have investigated the use of ICA to this end: ICA does not impose normality assumptions in the training data and also takes into account higher order moments of the distribution, e.g. skewness and kurtosis. In

this way, we expect to give a more accurate description of the training dataset and achieve better matching results.

2.3 Independent Component Analysis

2.3.1 ICA

Independent Component Analysis, which is also known as Blind Source Separation (BSS) [9], is a widely used method for separation of mixed signals. This concept can be illustrated as follows. Let X be a shape vector which is assumed to come from a mixture of signals of the form

$$X = A \cdot S \tag{2.2}$$

where A is a matrix containing mixing parameters and S is a matrix containing the source signals/shapes. The goal of Blind Source Separation is to calculate the original source signals from the mixture. Thus, to find the de-mixing matrix U that gives the following:

$$\hat{S} = U \cdot X \tag{2.3}$$

This method is called blind, because little information is available, i.e. both the mixing matrix A and the matrix containing the sources S are unknown. ICA can be defined as a method that finds a linear transformation, which maximizes the non-Gaussianity of the $\hat{s}_i$. The de-mixing matrix U is found by optimizing a cost function. Several different cost functions can be used for performing ICA, e.g. kurtosis, neg-entropy, etc. Therefore, different methods exist to calculate U. Three of the most frequently used ICA-methods are explained in the following sections.

2.3.2 ICA-methods

FastICA

The FastICA method is an iterative fixed-point algorithm that was developed by Hyvärinen *et al.* [6]. It is an alternative to gradient-based methods for maximizing non-Gaussianity and shows fast (cubic) convergence. This method can be used for optimizing different types of cost functions, such as kurtosis or neg-entropy. Contrary to gradient-based methods, the Fast-ICA method does not have a learning rate or other adjustable parameters. This is a great advantage, because in general, a bad choice of learning rate may destroy convergence.

InfoMax

This method is based on maximizing the output entropy (or information flow), of a neural network with nonlinear outputs and therefore is called InfoMax [7]. The non-linearities in the transfer function are able to pick up higher-order moments of the input distribution and perform redundancy reduction. This enables the neural network to separate statistically independent components in the input data. It can be shown that this method is equivalent to the Maximum Likelihood method [9].

JADE

The Joint Approximated Diagonalization of Eigenmatrices (JADE) [8] is an algorithm based on the joint diagonalization of the cumulant matrices. All cumulants of order 2 and 4 are involved and a joint diagonalization is performed with a Jacobi technique. The JADE algorithm also does not have any adjustable parameters, and therefore is a robust method. This method is computationally quite intensive, however, because all of the cumulant matrices are diagonalized at once.

2.3.3 Ordering of Independent Components

PCA results in a natural ordering of the vectors according to their variance, because the goal of PCA is to find orthogonal directions along which the projections of the shapes have maximal variance. Eigenvectors with highest variance are placed first and those with low variance are placed last. With ICA such an ordering is not obtained automatically. However, this ordering is essential in PCA for determining which and how many vectors will be used to give an accurate description of the training dataset: some vectors describe noise effects and are undesired in the shape model. To select the Independent Components (ICs) that describe most relevant independent directions within the training dataset, a sorting method for ICA is required. This question is still open in the literature. Several intuitive criteria considered for sorting the independent components, which could be applicable to ASMs, are explained in the following sections.

Variance of the histogram

This method for ordering the Independent Components is a similar scheme as the one followed in PCA, i.e. the variance can be considered as a measure of energy of the ICs. In this method all of the shapes are projected onto each of the ICs. A histogram of these projections is made and a Gaussian curve is fitted to this histogram. The variance of this Gaussian function is estimated for each of the ICs. A large variation describes a large range of shapes. The IC with small variance describes noise and outliers in the input dataset. Therefore, the ICs are ordered from largest variance to smallest.

Non-Gaussianity

Independent components are calculated by maximizing non-Gaussianity of the sample projections on the component. The ordering according to non-Gaussianity is based on statistical testing for Gaussianity of the sample projections. The Shapiro-Wilk test for normality [10] was implemented to this end. This test is based on the following hypotheses:

- H0: Data values are a random sample from a normal distribution
- H1: Data values are not a random sample from a normal distribution

The Shapiro-Wilk test provides two values, i.e. W (*the Shapiro-Wilk statistic*) and the associated p-value (the probability $PR < W$). If the p-value is less than the chosen level of significance (e.g. 0.05 for a significance level of 95%), the null hypothesis can be rejected at that level and this can be taken as evidence supporting non-Gaussianity. The components are ordered from maximally non-Gaussian to Gaussian. This measure aims at utilizing one of the implicit characteristics: ICA produces directions along which the shape space is maximally non-Gaussian. The ICs are ordered according to increasing p-values.

Alignment of Shapes with IC

Independent Components are vectors that span a shape space in order to describe the input dataset. Each of the ICs points in a direction, along which the projections of the shapes are maximally non-Gaussian. In shape space, the shapes can be considered as vectors that point in a specific direction (Fig. 2.1). This ordering method is based on ranking each IC according to how well it is aligned with respect to the rest of the training set. Therefore, the mean angle α between each IC and the shape set is calculated. The smaller the mean angle is, the more the shape set is aligned with the Independent Component. The ICs are sorted with increasing mean angle.

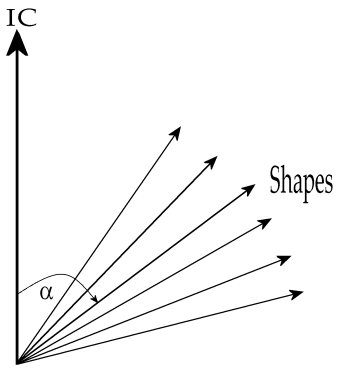

Figure 2.1: Mean angle between IC and shapes

Locality of Shape Variation

Vectors obtained with PCA describe global shape variations, and more localized variations are eliminated. Segmenting with a description of the dataset obtained with PCA shows results that are globally good. However, locally the correct contours cannot be found in some cases, because local deformations are not accommodated by the model. Also, information about the locality and amplitude of the shape variations can be very useful for diagnostic purposes. In this way for example, areas of myocardial malfunctioning may be discovered by analyzing the corresponding ICs. Therefore, an ordering of the ICs according to locality and amplitude of the shape variation is designed as follows.

When the corresponding weight factor of an Independent Component is varied, the IC shows a variation with respect to the mean with certain amplitude. For noisy modes, these variations are relatively small and not localized. For modes that describe examples as seen in the training data, these variations are localized and have large amplitudes.

To quantify the locality of the shape variations and their amplitudes, first the shapes are projected onto each IC. Of these projections a histogram is computed. The width of this histogram, W, is calculated as a measure of variation of the Independent Component. Here, W plays a role similar to the variance in PCA but it is less dependent on the presence of outliers or non-Gaussian shape of the histogram. Then, the shape parameters are varied between limits $-W/2$ and $+W/2$. The width of the histogram, W, was determined as follows. First the median value of the histogram is calculated. Parting from this value, the surface of the histogram is determined by adding the corresponding bin values. To discard outliers, the bin values are summed until 90% of the total surface of the histogram is reached. The coordinates spanning 90% of the total surface are used to determine the histogram width.

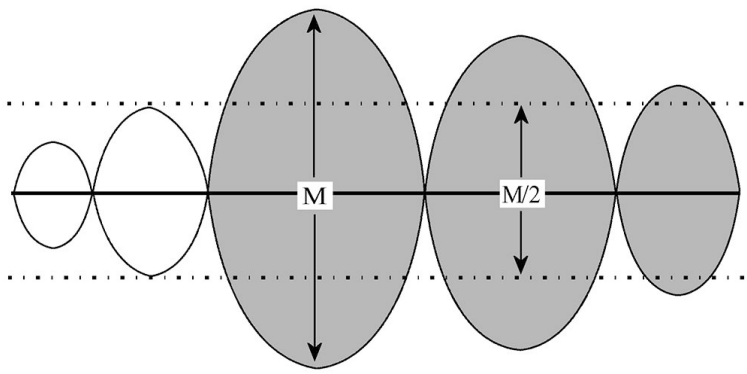

Figure 2.2: Example of shape variation with maximum peak (M) and surface of peaks that are taken into account (grey)

After weighing the IC with the corresponding histogram widths, the maximum amplitude of the peaks is determined. Subsequently, to eliminate the effect of noisy peaks, the peaks whose amplitude is larger than 50% of the maximum peak are selected (Fig. 2.2). The total surface O of these peaks is calculated. The ICs are now ordered according to the following criterion:

$$C = W \cdot M \cdot \frac{O}{F} \tag{2.4}$$

where C is the criterion used for ordering, W is the width of the histogram, M is the maximum amplitude of the largest peak, O is the total surface of the peaks that are larger than 50% of the largest peak and F the ratio between the shape points spanning the peaks and the total number of points in the shape. In this criterion, information about the number of shapes described is included by means of W, the significance of the peak is denoted by M and the ratio (O/F) gives information about the locality of the ICs. Noisy ICs show variations that have small amplitudes and that occur along the entire shape, therefore for these ICs the fraction (O/F) will be small and thus the criterion value will be lower. Sorting is performed with decreasing value of C.

2.4 Results

2.4.1 Data Sets

To compare the different ICA and sorting methods, the following datasets were available:

- Set I: 51 expert drawn contours from 2-chamber long-axis MR images of the end-diastolic phase of the left ventricle, consisting of 64 landmark points each
- Set II: 89 expert drawn contours of the cardiac left ventricle as seen in X-ray angiography images, each consisting of 60 landmark points
- Set III: 150 expert drawn shapes of the cardiac left and right ventricle as seen in short-axis MR images of the end-diastolic phase, consisting of 105 landmark points each

2.4.2 Comparison between ICA-methods

To evaluate the effect of the different cost optimization functions on the Independent Component Analysis results, the FastICA, InfoMax and the JADE methods for ICA were tested on the above mentioned datasets. Visual inspection showed that these methods yielded highly similar, yet not identical Independent Components. For example the locations of the main variations in the ICs seemed equal; however, the shape and size were slightly different. Also, the small peaks differed in location between several ICA-methods.

The vectors that result from ICA showed localized variations, whereas Principal Component Analysis yields vectors that show global variations. Figure 2.3 shows the difference between the modes of variation that are obtained with PCA and with ICA.
The FastICA method has very fast convergence and can handle high dimensional signals. However, this method has a random initialization phase and therefore, the computed ICs were not identical when the algorithm was run several times. This undermines the reproducibility of the results and this method was thus not preferred.
The InfoMax method is a gradient-based method and has a learning rate and other adjustable parameters. In some cases, especially in the case of the dataset consisting of 150 short-axis cardiac shapes, this method did not converge. For the ordering method comparison, we have selected the JADE algorithm, because this method does not have a random initialization and also does not have any tunable parameters and therefore is more robust. However, this method is computationally intensive. Since our calculations are performed off-line and the training of the ASM has to be done only once, this does not pose any serious problems.

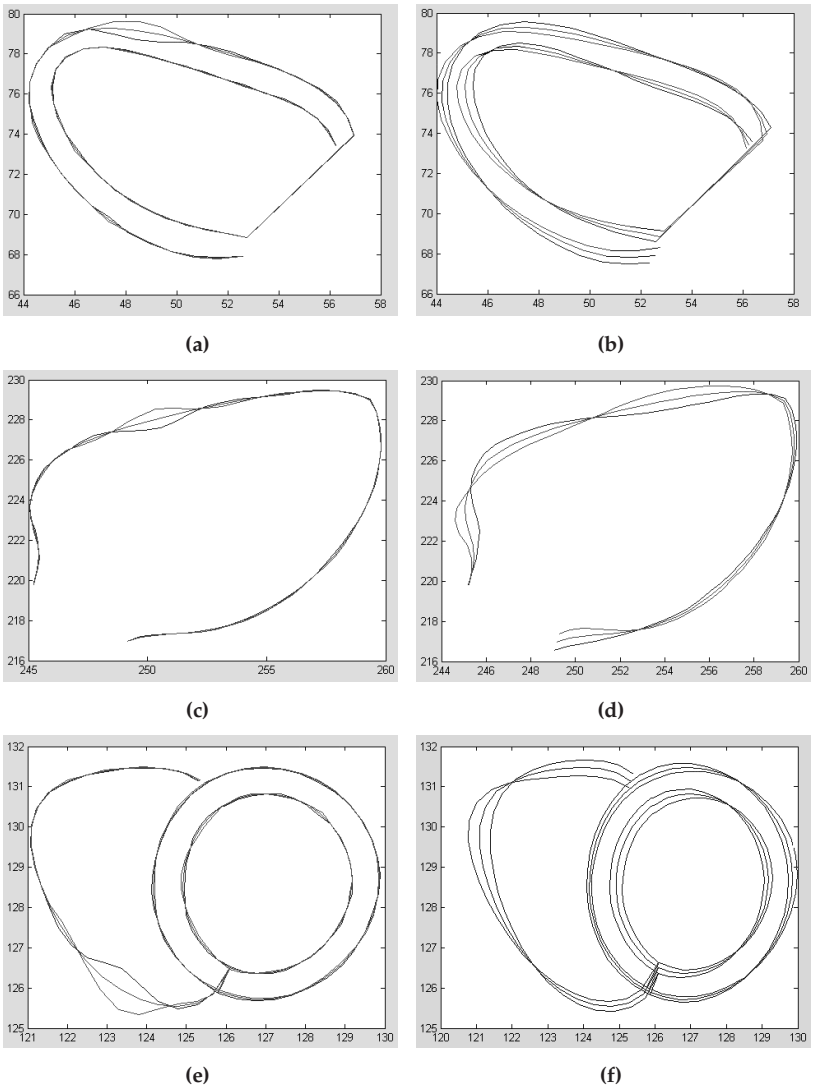

Figure 2.3: Left: modes of variation obtained with ICA and right: modes of variation obtained with PCA for respectively long-axis MRI (above), long-axis angiography (middle) and short-axis MRI (below) shapes of the heart. These images show the variation of the IC (left) and the variation of the eigenvectors obtained with PCA (right) when the corresponding weight factors are varied between $-W/2$ and $+W/2$, and -3σ and $+3\sigma$ respectively.

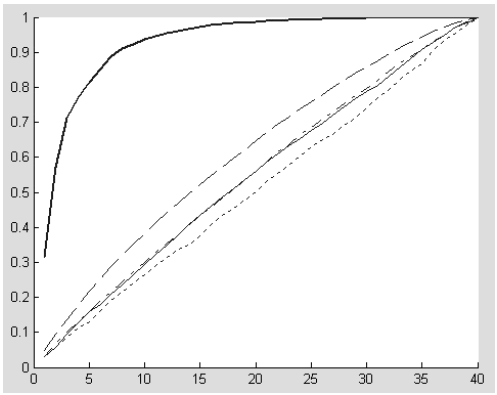

(a)

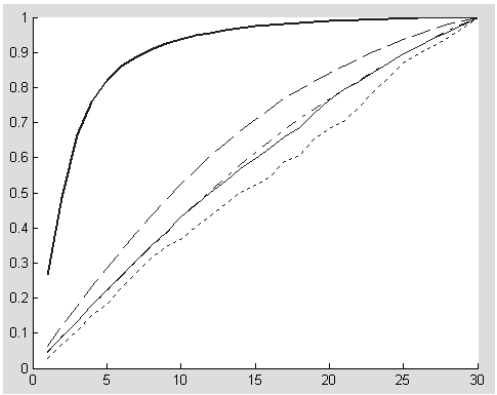

(b)

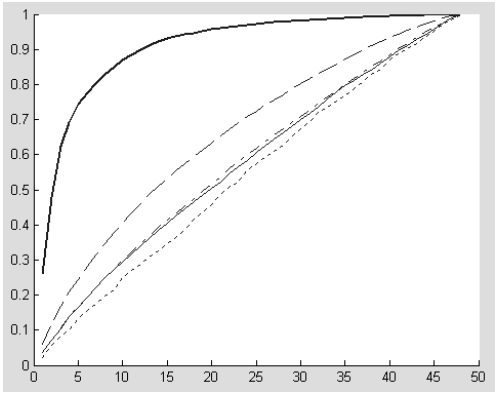

(c)

Figure 2.4: Cumulative variance curves for ICs of long-axis MRI shapes (a), long-axis angiography shapes (b) and short-axis MRI shapes (c) according to different ordering methods (dashed: variance, dotted: non-Gaussianity, dash-dot: alignment, solid: locality), compared to PCA (bold)

2.4.3 Results of Ordering Methods

No golden standard was available for evaluating the results of the different ordering schemes. Therefore, the results were evaluated visually according to criteria that were intuitively expected, e.g. the property that noisy ICs show small variations, which are not localized. Also the cumulative variance was considered by means of the half-width of the histograms of the shape projections onto the ICs (see Fig. 2.4).

2.5 Discussion & Conclusions

The Principle Component Analysis gives a representation of the training dataset, which consists of vectors that describe global deformations, whereas the vectors that are obtained with Independent Component Analysis describe local deformations. Furthermore, PCA assumes that the training data is from a Gaussian distribution, which is not needed for ICA. However, the vectors given by PCA are ordered, which is not the case with ICA.

As can be seen from Fig. 2.4, dimensionality reduction with ICA is not as good as with PCA. It is inherent to the PCA method to find directions along which the variance is the greatest and, in this sense, PCA is known to be optimal. Consequently, the first few modes explain most of the shape variations, whereas the later modes are less significant. The ICA method however, maximizes the independence between the vectors and therefore each Independent Component describes an almost equal amount of variance.

With regard to compression, the ordering method according to the variance of the projections comes the closest to PCA, because the ordering criterion is similar to the natural ordering in PCA. However, the variance proved to be a poor measure for ordering the Independent Components, because in order to obtain the variance, Gaussian curves had to be fitted to the histograms of the projections of the shape set onto each IC. Because ICA finds directions in shape-space along which the projections of the shape set are maximally non-Gaussian, the histograms of the projections of the shapes onto the IC were also non-Gaussian. This resulted in a high ranking of modes that described noise or outliers.

To exploit the inherent property of ICA, that it maximizes non-Gaussianity, a statistical testing method (the Shapiro-Wilk W-statistic [10]) was implemented to obtain a measure for sorting the ICs. However, statistical testing methods for non-Gaussianity, such as the Shapiro-Wilk method, could distinguish between Gaussian and non-Gaussian distributions only and were not able to give a gradual measure of non-Gaussianity, which is needed for sorting the Independent Components. If the p-value is lower than the threshold, the null hypothesis can be rejected and there is evidence for non-Gaussianity. However, our experiments have shown that a lower p-value does not necessarily imply that a sample is drawn from a more non-Gaussian distribution.

Next, sorting according to the mean angle between the shape set and the ICs was

tested. The resulting mean angles were all close to 90^o. Because the vectors are in a high-dimensional space, they can point in many different directions and therefore do not have to be aligned with the Independent Components. Ordering according to this method resulted in a high ranking for modes describing noise artifacts and therefore, ordering according to this method did not yield good results.
Finally, the ordering according to the locality of the modes was investigated. From Fig. 2.4 it can be seen that the cumulative variance curves for this ordering method are flatter than for e.g. ordering according to the variance of the histograms. However, this method resulted in giving modes that showed localized and large variations a high ranking, whereas modes that described noisy effects were placed later. From the methods that were tested, the results obtained from this ordering technique were the best, because they agreed with what was intuitively expected.
As mentioned earlier, no golden standard for evaluating the results of the ordering method is available and therefore the results were mainly interpreted according to what was intuitively expected. In the nearby future these methods will be implemented in the AAM segmentation software for testing and selecting the ordering method that performs best according to segmentation errors. We believe that this task-based metric will more clearly elucidate the pros and cons of the proposed ranking schemes.

Acknowledgements

M. Üzümcü is supported by grant IBV00303 from IOP, Dutch Ministry of Economic Affairs, and a research-stay grant in Spain by the same Ministry. A.F. Frangi is supported by a Ramón y Cajal Research Fellowship and grants TIC2002-04495-C02 and FIT-070000-2002-935 from the Spanish Ministry of Science and Technology. B.P.F. Lelieveldt is supported by an Innovational Research Incentive 2001 grant from the Netherlands Organization for Scientific Research (NWO).

References

[1] T.F. Cootes, C. Taylor, A. Hill, J. Halsam, "The Use of Active Shape Models for Locating Structures in Medical Images", Proceedings of the 13th International Conference on Information Processing in Medical Imaging, 33–47, 1993

[2] T.F. Cootes, G.J. Edwards, C.J. Taylor, "Active Appearance Models", Proceedings of the European Conference on Computer Vision, (2): 484–498, 1998

[3] G. Edwards, C. Taylor, T. Cootes, "Interpreting face images using active appearance Models", Proceedings of the Third IEEE International Conference on Automatic Face and Gesture Recognition, 300–305, 1998

[4] S. C. Mitchell, B. P. F. Lelieveldt, R. J. van der Geest, J. G. Bosch, J. H. C. Reiber, and M. Sonka, "Multistage Hybrid Active Appearance Model Matching: Segmentation of Left and Right Cardiac Ventricles in Cardiac MR Images", IEEE Transactions on Medical Imaging, 20(5): 415–423, 2001

[5] S.C. Mitchell, J.G. Bosch, B.P.F. Lelieveldt, R.J. van der Geest, J.H.C. Reiber, M. Sonka, "3D Active Appearance Models: Segmentation of Cardiac MR and Ultrasound images", IEEE Transactions on Medical Imaging, 20(9), 2002

[6] A. Hyvärinen and E. Oja, "A Fast Fixed-Point Algorithm for Independent Component Analysis", Neural Computation, 9(7): 1483–1492, 1997

[7] A.J. Bell and T.J. Sejnowski, "An Information Maximization Approach to Blind Separation and Blind Deconvolution", Neural Computation, 7: 1129–1159, 1995

[8] J.F. Cardoso, "Higher Order Contrasts for Independent Component Analysis", Neural Computation, 11(1): 157–192, 1999

[9] A. Hyvärinen, J. Karhunen and E. Oja, Independent Component Analysis, John Wiley & Sons, 2001

[10] S.S. Shapiro and M.B. Wilk, "An analysis of variance test for normality (complete samples)", Biometrika, 52, 3 and 4, 591–611, 1965

[11] M. Bressan, J. Vitrià. "Independent Modes of Variation in Point Distribution Models". Proceedings of the 4th International Workshop on Visual Form (IWVF4), LNCS 2059, Springer Verlag, 123–134, 2001

3

Comparing ICA and PCA in Active Appearance Models

In compassion and grace be like the sun

This chapter was adapted from:
ICA vs. PCA Active Appearance Models: Application to cardiac MR Segmentation
M. Üzümcü, A.F. Frangi, M. Sonka, J.H.C. Reiber, B.P.F. Lelieveldt
Lecture Notes in Computer Science, MICCAI '03, Eds: R.E. Ellis, T.M. Peters, 2878: 451 – 458, 2003

Abstract

Statistical shape models generally use Principal Component Analysis (PCA) to describe the main directions of shape variation in a training set of example shapes. However, PCA has the restriction that the input data must be drawn from a Gaussian distribution and is only able to describe global shape variations. In this paper we evaluate the use of an alternative shape decomposition, Independent Component Analysis (ICA), for two reasons. ICA does not require a Gaussian distribution of the input data and is able to describe localized shape variations. However, with ICA the resulting vectors are not ordered, therefore, a method for ordering the Independent Components is presented in this paper.
To evaluate ICA-based Active Appearance Models (AAMs), 44 leave-3-out models were trained on a set of 132 short-axis cardiac MR Images with PCA-based as well as ICA-based AAMs. Both models showed comparable segmentation accuracy. A subspace analysis showed that the PCA and ICA subspaces describe nearly the same amount of variance in the dataset. Also, the local nature of independent components may be counteracted by the final PCA in the appearance model. Experiments with Active Shape Models are ongoing to further explore the locality properties of ICA.

3.1 Introduction

Statistical shape models such as Active Shape Models (ASM) [1] or Active Appearance Models (AAM) [2] are widely used in different image segmentation and recognition domains [3, 4, 5]. These models have shown to be powerful in medical image analysis, mainly because of their capability to include expert knowledge. Statistical shape models are trained from a set of images, in which contours have been drawn by experts. These models generally use Principal Component Analysis to describe the main directions of shape variation in the training set of example shapes. However, PCA is a method that fits a Gaussian hyper-ellipsoid to the data and therefore assumes that the data is normally distributed, which frequently is not the case. This assumption follows from the fact that PCA only takes into account the first (mean) and second (variance) order moments of the distribution of the input data. This may lead to an incorrect statistical description of the dataset and to the generation of implausible shapes. Furthermore, PCA results in eigenvectors that describe global variations, i.e. the entire shape deforms when a parameter corresponding to a vector is changed. This fact usually hampers achieving a locally accurate segmentation.
A number of alternatives have been proposed to extend the formulations of ASMs and AAMs to other types of statistical shape decompositions. Sozou *et al.* [16] proposed a method using polynomial regression to fit high order polynomials to the non-linear axis of the training set. However, this method does not adequately compensate for higher order non-linearity, such as the smaller modes of variation that describe high frequency oscillations. Furthermore, the order of the polynomial to be used must be selected and the fitting process is time consuming. Davatzikos *et*

al. [17] presented hierarchical active shape models using the wavelet transform. In this approach, the shapes were divided into small pieces and a PCA was performed on each piece separately. With this method global and local shape variations can be described and the performance of the proposed method is better than standard ASM when a small number of training samples is available. However, when the training dataset is sufficiently large, the performance of the hierarchical ASM is comparable to standard ASM.

In this paper, we investigate and evaluate the use of an alternative decomposition technique, Independent Component Analysis (ICA), which does not make the above mentioned assumptions on the distribution of the input data and also takes into account higher order moments of the distribution, such as the skewness (3^{rd} order) and kurtosis (4^{th} order). The goal of ICA is to maximize the independence between the vectors that describe the variation as seen in the dataset. ICA has been successfully applied in various image-related domains. In [18], ICA is used for detection of facial components in video sequences. In [19], an ICA-based method for watermark detection is presented. Calhoun et al. [20] use ICA for analyzing functional MRI of the brain. Bartlett *et al.* [21] have proposed a method for face recognition based on ICA and Bressan *et al.* [22] have investigated the use of ICA in Point Distribution Models. In previous work [12], we have demonstrated that ICA yields vectors that describe localized shape variations, whereas PCA vectors describe global shape variations. Segmentation results obtained with PCA-based statistical shape models are globally good, however, there are local errors because the model cannot deform locally. Many researchers have tried to resolve this by using a subsequent constraint relaxation or additional post-processing of the model generated segmentation, e.g. [15, 24, 25]. However, segmentation results obtained with an ICA-based AAM may be more accurate because of increased local control with ICA.

The main contribution of this paper is the evaluation of Independent Component Analysis for medical image segmentation using Active Appearance Models. To enable the use of ICA in statistical shape modeling, vectors describing the shape variation in the training dataset need to be separated from vectors describing noise. In classical PCA, the eigenvectors are ordered automatically according to the associated eigenvalues (variances). In Independent Component Analysis, however, the resulting vectors are not naturally ordered. Therefore, a novel method for sorting the independent components is introduced to distinguish between vectors describing actual shape variations and those describing noise. In addition, we present a quantitative comparison between conventional PCA-based models and our ICA approach.

This chapter is further organized as follows. In Section 2 Active Appearance Models are briefly explained. Section 3 introduces Independent Component Analysis. In section 4, the evaluation of ICA versus PCA and the results are presented. Section 5 discusses the evaluation results and the chapter ends with conclusions.

3.2 Active Appearance Models

Active Shape Models and Active Appearance Models were introduced by Cootes *et al.* [1, 2], and can be applied to image segmentation in various domains [3, 4]. Since introduction, several successful applications of AAMs in medical image segmentation have been presented. Initially, Cootes has demonstrated the application of 2D AAMs on finding structures in brain MR images [6], and knee cartilage in MR images [7]. In 2D cardiac MR images, Mitchell *et al.* successfully applied AAMs to segment the left and right ventricle [4]. Thodberg applies a 2D AAM to reconstruct bones in hand radiographs [8]. Bosch *et al.* applied 2D + time AAMs to segment endocardial borders in echocardiography [9], introducing a correction method to compensate for non-Gaussian intensity distributions in echo-cardiographic images. Beichel *et al.* describe a semi-3D AAM extension applied to segmentation of the diaphragm dome in 3D CT data [10]. Mitchell *et al.* describe a full 3D AAM extension, and apply it to 3D cardiac MR data and 2D + time echocardiograms [5]. In many of the applications mentioned here, Active Appearance Models have been shown to outperform other segmentation approaches for two reasons:

- They combine correlated intensity and shape knowledge, thus maximally integrating a-priori knowledge, resulting in highly robust performance
- They model the relationship between expert contours and underlying image data, and are therefore capable of reproducing expert contour drawing behavior

AAMs describe statistical variations as seen in a set of example images, in which corresponding landmark points are annotated. The shapes, which are spanned by the landmarks, are first aligned using Procrustes analysis to compensate for translation, rotation and scaling differences between the shape samples. Next, the mean shape of this set of aligned shapes is calculated and modes of shape variation are computed by applying PCA on the sample covariance matrix. Each shape sample can then be expressed by means of a set of shape coefficients $\vec{b}_s$ as follows:

$$\vec{x} \approx \bar{\vec{x}} + Q_s \cdot \vec{b}_s \tag{3.1}$$

where $\vec{x}$ is a shape sample, $\bar{\vec{x}}$ the mean shape, Q_s is the matrix describing the modes of shape variation in the training set and $\vec{b}_s$ is the vector containing the coefficients weighing those eigenvectors. After warping the gray values in the images onto the mean shape, they are sampled in an intensity vector $\vec{g}$. Similar to the shape model, modes of gray value variation are calculated by performing a PCA. Each gray value patch can then be expressed by means of a set of gray value coefficients $\vec{b}_g$ as follows:

$$\vec{g} \approx \bar{\vec{g}} + Q_g \cdot \vec{b}_g \tag{3.2}$$

where $\vec{g}$ is a gray value patch, $\bar{\vec{g}}$ the mean gray value patch, Q_g is the matrix describing the modes of variation of the gray values and $\vec{b}_g$ the vector of weight coefficients.

The shape and texture of a shape sample can be described by the parameters $\vec{b}_s$ and $\vec{b}_g$ respectively. Because shape and gray values are correlated, the shape and gray value models can be combined as follows:

$$\vec{b} = \begin{pmatrix} W_s \vec{b}_s \\ \vec{b}_g \end{pmatrix} \tag{3.3}$$

Where W_s is a diagonal matrix of weight factors for the shape parameters. A PCA can now be performed on the combined vectors $\vec{b}$ and the appearance can be expressed by means of a set of appearance parameters $\vec{b}_a$ as follows:

$$\vec{a} \approx \bar{\vec{a}} + Q_a \cdot \vec{b}_a \tag{3.4}$$

where $\vec{a}$ is an appearance, $\bar{\vec{a}}$ the mean appearance, Q_a a matrix describing the modes of appearance variation and $\vec{b}_a$ the vector of appearance weight parameters.
Matching the model to an unseen image is performed by minimizing the root mean square error between the model generated image and the target image, within the boundaries of statistically plausible model limits. To drive the model matching iterations, the parameter update steps are computed from the residual images $\delta g_0 = g_s - g_m$, where g_s denotes the target image, and g_m the model synthesized image.
As mentioned above, PCA is used to derive the main directions of shape variation in the dataset. PCA assumes that the input data is drawn from a multidimensional Gaussian distribution, which in practice tends to be an oversimplification. Therefore, we have investigated the use of ICA to find the main directions of shape variation: ICA does not impose normality assumptions in the training data and takes into account higher order moments of the distribution, such as skewness and kurtosis. This way, we expect to give a more accurate description of the training dataset and achieve better matching results.

3.3 Independent Component Analysis

3.3.1 Background

Independent Component Analysis, also known as Blind Source Separation (BSS) [13, 14], is a widely used method for separation of mixed signals. This concept can be illustrated as follows. Let X be a shape vector, which is assumed to come from a mixture of signals of the form

$$X = A \cdot S \tag{3.5}$$

where A is a matrix containing mixing parameters and S a matrix containing the source signals/shapes. The goal of Blind Source Separation is to calculate the origi-

nal source signals from the mixture. Thus, to estimate the de-mixing matrix U that gives the following:

$$\hat{S} = U \cdot X \tag{3.6}$$

This method is called blind, because little information is available, i.e. both the mixing matrix A and the matrix containing the sources S are unknown. The de-mixing matrix U is found by optimizing a cost function. Several different cost functions can be used for performing ICA, e.g. kurtosis, neg-entropy, etc. Therefore, different methods exist to calculate U. In previous work, the effect of these methods on the resulting vectors was evaluated [12]. Based on this evaluation, we have chosen to use the JADE method for performing ICA, because this method was found to be robust and free of tunable parameters.
In the application of ICA to shapes, the rows $\vec{x}_i$ of the mixed signals X represent the shape samples. The rows of S are the independent components and the rows $\vec{a}_i$ of A contain the corresponding weight factors. A shape sample can be reconstructed as follows:

$$\vec{x}_i = \bar{\vec{x}} + \vec{a}_i \cdot S \tag{3.7}$$

3.3.2 Ordering Independent Components

PCA results in a natural ordering of the vectors according to their variance, because the goal of PCA is to find orthogonal directions along which the projections of the shapes have maximal variance. Eigenvectors with highest variance are placed first and those with low variance are placed last. With ICA, such an ordering is not obtained automatically. However, this ordering is essential for determining which and how many vectors shall be used to give an accurate description of the training dataset: some vectors describe noise effects and are undesired in the shape model. To select the Independent Components that describe *most relevant* independent directions within the training dataset, a sorting method for ICA is required. In [12], a number of sorting methods were evaluated. The method that was found to perform best is explained in the following paragraphs.
When the corresponding weight factor of an IC is varied, the IC shows a variation with respect to the mean with certain amplitude. For ICs describing noise, these variations are relatively small and occur along the entire contour. ICs that describe shape variations as seen in the training data, typically involve prominent variations, which are localized and have relatively large amplitudes (see Fig. 3.1).
The above-mentioned property can be used to distinguish the ICs that describe noise from those that describe actual shape variations. To determine the locality of the variations, the point-to-point distances of the amplitudes of the shape variations are determined as follows. Let $\hat{\vec{x}}_i$ be a generated shape variation with the i-th component:

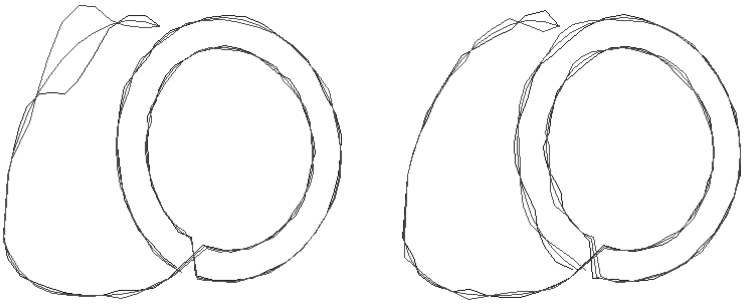

(a) (b)

Figure 3.1: Independent Component describing a mode of actual shape variation (left) and Independent Component describing noise (right). The variation of the ICs between the two extremes when the corresponding weight factor is varied, is shown.

$$\hat{\vec{x}}_i = \bar{\vec{x}} + \vec{\Phi} \cdot \vec{a} \tag{3.8}$$

where $1 \leq i \leq p$, $a_i = 1$ and $a_j = 0$ for $j \neq i$. The distance vector $\vec{d_i} \in \mathbb{R}^m$ describes the distance of each landmark of $\hat{\vec{x}}_i$ to the mean shape and is defined as follows:

$$\vec{d}_i^{(j)} = \sqrt{\sum_{k=2j-1}^{2j} \left(\hat{\vec{x}}_i^{(k)} - \bar{\vec{x}}^{(k)} \right)^2} \tag{3.9}$$

where $j = 1, 2, , m$. The width of the shape variations is determined by constructing a bank of Gaussian filters with varying width and determining the normalized cross-correlation between each kernel and the distance plot as follows. Consider two series $x(i)$ and $y(i)$ where $i = 0, 1, 2, \ldots, N-1$. The normalized cross-correlation r at delay t is defined as:

$$r(t) = \frac{\sum_i \left[(x(i) - \mu_x) * (y(i-t) - \mu_y) \right]}{\sqrt{\sum_i (x(i) - \mu_x)^2} \sqrt{\sum_i (y(i-t) - \mu_y)^2}} \tag{3.10}$$

where $r(t)$ is the correlation rate at delay t, μ_x the mean of series $x(i)$ and μ_y the mean of series $y(i)$. The value of $r(t)$ varies between -1 and 1, negative when the two signals are in anti-phase. The closer the value of $r(t)$ is to -1 or 1, the more the two signals are correlated.

ICs that describe noise show small shape variations that occur along the entire shape, whereas ICs describing real shape variation show localized shape variations with large amplitude. Figure 3.2 shows the differences in cross-correlation response for a noise component and for a component that describes shape variation. ICs describing actual shape variations show a maximum in the cross-correlation response at a

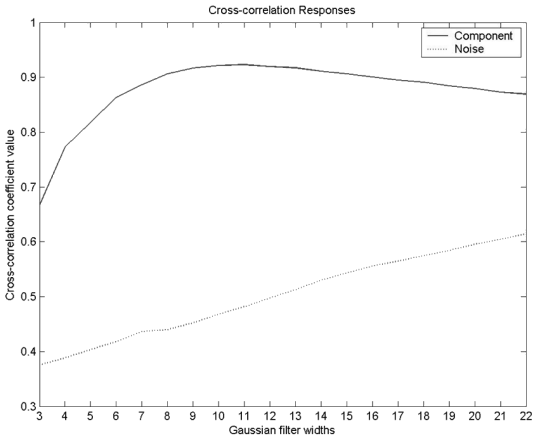

Figure 3.2: Responses from cross-correlation of Independent Component with Gaussian filter banks with width varying between 3 and 22 pixels. Independent Component describing actual shape variation has a maximum, IC describing noise has no maximum.

certain width of the Gaussian filter bank. This way the landmark where the maximum response occurs can be determined and the shape variations can be localized. The noise ICs, however, show no peak in the cross-correlation response and correlate best with the widest Gaussian filter. This way, they can be detected and filtered out automatically.

3.3.3 Integration of ICA into AAM-framework

As explained in section 3.2, the AAM consists of 3 parts, e.g. the shape part, the gray value part and the appearance part (see Fig. 3.3). The Independent Component Analysis is only performed on the shape part of the AAM. The modes of gray value variation are computed with PCA. ICA is not performed on the intensity patches, because we are mainly interested in obtaining a more accurate shape description, and not a detailed intensity model. The gray value variations only serve as a means to constitute the matching criterion, whereas the shape variations define the allowed deformations. Therefore, the shape part of the model asserts the most critical influence on border localization accuracy.

An appearance model was constructed by combining the principal components of the gray value model with the independent components of the shape model and performing a PCA on this combination. The appearance model was restricted between -3σ and $+3\sigma$ with the σ resulting from the final appearance PCA.

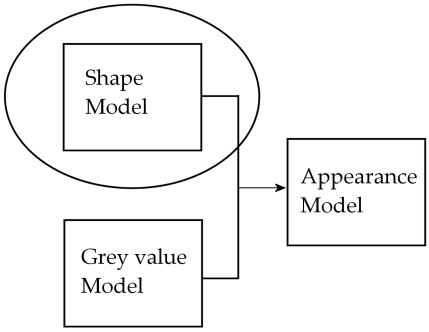

Figure 3.3: Parts constituting the AAM, ICA is applied only to the shape part of the model.

3.4 Evaluation of ICA vs. PCA

3.4.1 Data

To evaluate the segmentation results obtained with the ICA-based AAM, a set of 132 routinely acquired multislice multiphase short-axis midventricular MR images of the cardiac left and right ventricle in the end-diastolic phase was used. Images were collected from 44 subjects, and the three mid-ventricular slices per subject were used for model training and evaluation. The images had a resolution of 256^2 pixels, a field of view of 400 – 450 mm and pixel sizes of 1.56 – 1.75 mm. In each image left- and right-ventricular endo- and epicardial contours were drawn by experts, and were resampled to 105 corresponding landmarks.

3.4.2 Evaluation Criteria

The ICA-based and PCA-based Active Appearance Models were compared using the following criteria:

- The *reconstruction error* describes the generative power of the statistical method, i.e. the ability of the method to regenerate the shape samples of the dataset after dimensionality reduction.
- The *average point-to-point error* is a measure for the segmentation accuracy. This average is calculated over all landmarks, of which a contour consists.
- The *maximum point-to-point error* gives information on the local nature of the segmentation errors.
- The *sensitivity to initialization* is tested by initializing the model with several offsets from the optimal position.

3.4.3 Results

Reconstruction Error

Using the eigenvectors computed with PCA or the Independent Components resulting from the ICA, the original shapes from the training dataset can be reconstructed with eq. (3.1) in the PCA case and eq. (3.7) in the ICA case. The shapes cannot be reconstructed exactly, because of the approximations made and small errors are present between the original expert drawn shapes and the reconstructed shapes.
The reconstruction error of PCA and ICA is compared to evaluate the model performance and determine which method approximates best the original shapes in the training dataset. To this end, models were generated with PCA and ICA consisting of 5 to 50 vectors describing shape variation. The entire shape set was reconstructed with these models and the reconstruction error was calculated by determining the overall average point-to-point distance between the expert drawn and reconstructed shapes. Figure 3.4 shows the reconstruction error of both models.

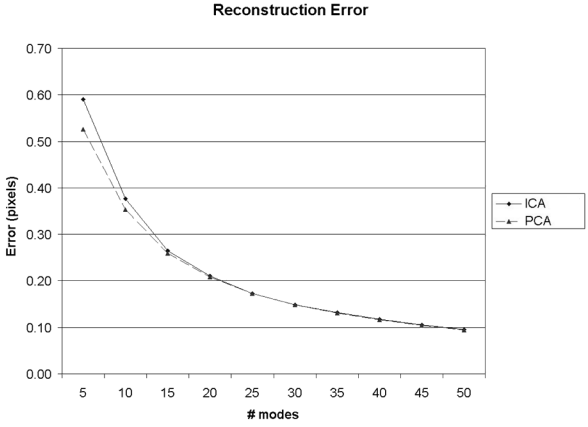

Figure 3.4: Comparison of reconstruction error between ICA and PCA for increasing number of modes used.

Segmentation performance

The ICA-based appearance models were calculated using 35 independent components for shape variation for each model. Subsequently, the ICA modes were sorted using the cross-correlation sorting described earlier and noise ICs were eliminated. In addition, intensity models were constructed following the approach based on PCA. For these models, 98% of the total variation was retained. The computation of the intensity and appearance parts was identical for both approaches.
To quantitatively evaluate the ICA-based AAM segmentation, 44 leave-3-out models were trained. This way, 3 samples (1 subject) were left out and a model was trained

on the remaining 129 samples; this was repeated 44 times by leaving out different samples. The performance of the models was tested on the left-out samples.
For each test, the model search was started with the mean model at positions displaced from the known optimal position by ± 10 pixels, following the approach in [9]. The segmentation results were compared on the basis of the average and maximum point-to-point errors between the hand-labeled and the automatically detected contour points (see Table 3.1).

Table 3.1: Comparison of average and maximum point-to-point errors obtained with PCA- and ICA-based Active Appearance Models

	Average Point-to-Point Error (Pixels)				Maximum Point-to-Point Error (Pixels)			
	No Offset		Offset		No Offset		Offset	
AAM type	Median	90%-ile	Median	90%-ile	Median	90%-ile	Median	90%-ile
PCA-based	1.62	2.61	3.10	6.23	4.55	8.13	7.89	13.84
ICA-based	1.71	2.76	2.89	5.29	4.70	8.12	7.27	12.62

3.5 Discussion

The segmentation accuracy of ICA-based AAMs was compared to the accuracy obtained with PCA-based AAMs for contour detection in cardiac short axis images. Because of the local nature of the shape variations described by the independent components, ICA-based AAMs were expected to yield better segmentation results than PCA-based AAMs.
The reconstruction error for the ICA and PCA models was slightly better for the PCA models in case a small number of modes was selected (< 10). For higher model dimensionality, the ability of both models to reconstruct the training samples was nearly identical.
The segmentation performance of the ICA-based AAM was also comparable to the performance of the classical PCA-based AAM. In case of initialization at the known optimal positions, PCA shows slightly better results and in the case of model initialization with an offset from the optimal position, ICA based AAMs show slightly better results. However, the differences were not statistically significant.
As the average reconstruction and segmentation errors were comparable over all landmarks and shapes, a local error analysis was performed to investigate whether the distribution of the segmentation errors was different for the ICA-based AAMs compared to the PCA-based AAMs. ICA-based segmentations were expected to yield more uniformly distributed landmark errors, whereas PCA-based segmentations were expected to result in locally varying landmark errors. The point cloud of error distributions per landmark over all segmentations was considered and ellipses

were fit, describing local error distributions. Figure 3.5 shows the distribution of the errors per landmark in case of PCA (left) and ICA (right).

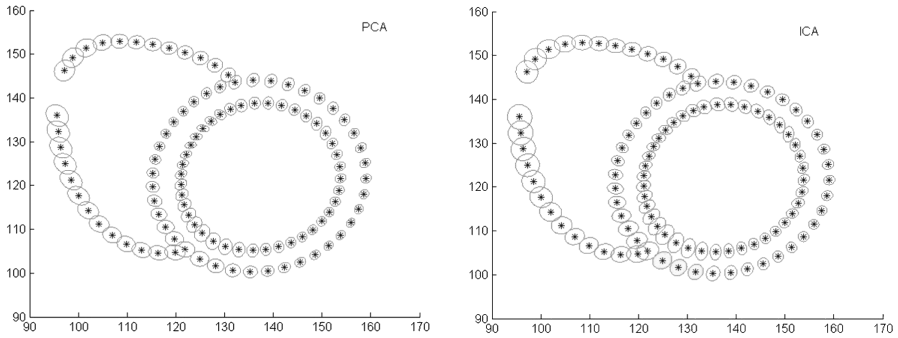

(a) **(b)**

Figure 3.5: Distribution of errors per landmark in case of PCA (a) and ICA (b).

As can be seen from Fig. 3.5, the distribution of the errors is highly similar for both methods. In case of ICA the distributions in the apex of the right ventricle are slightly more circular, whereas in case of PCA the distributions were slightly elliptical. However, differences in error distributions were small.

To understand the highly similar reconstruction errors, segmentation performance and error distributions of ICA and PCA based AAMs, a subspace analysis was performed. Since both ICA and PCA are used for dimension reduction, the high-dimensional data is mapped onto a lower dimensional subspace. A potential explanation for the comparable performance is the fact that if the intersection of the PCA and ICA subspaces shows a large overlap, both decomposition methods explain approximately the same variation in the dataset. This showed to be the case (see Fig. 3.6): while retaining 35 PCA and ICA modes, the intersection subspace contains 12 vectors, which describe nearly the same amount of variance as the first 12 high-energy PCA modes. This strongly suggests that these intersection vectors actually describe a similar shape range, where PCA gives a global description and ICA a local description.

From this subspace analysis we can conclude that although ICA yields localized shape variations, it does not give a better description of the variations as seen in the training dataset. ICA results in a different representation of the same information, which in case of segmentation performance is an equivalent representation to PCA. However, we have shown in other work [23] that for disease classification purposes, the localized ICA shape variations enable an intuitive ordering along the contour, which has the advantage that population differences can be localized and intuitively interpreted. For data compression applications however, the variance packing of PCA in the first few modes is an advantage over ICA.

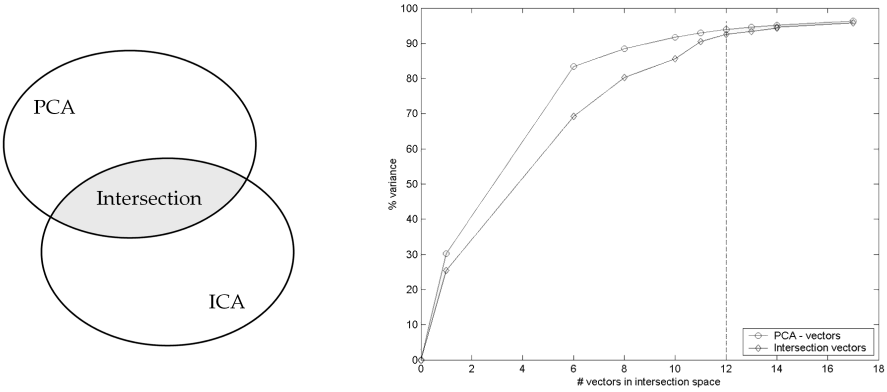

Figure 3.6: Amount of variance explained by high-energy PCA modes and by vectors in the intersection subspace (a). When 35 modes of ICA and PCA are retained, the intersection subspace contains 12 vectors. These vectors describe nearly the same amount of variance as the 12 high-energy PCA eigenvectors (b).

3.6 Conclusions

In this chapter, we evaluate the use of an alternative shape decomposition to PCA, Independent Component Analysis (ICA), for application in statistical shape modeling. To this end, we introduce a novel method for ordering the Independent Components. We have compared the reconstruction error and the segmentation performance of ICA based Active Appearance Models (AAMs) with PCA-based AAMs in an evaluation study on 132 short-axis cardiac MR Images. Both models showed comparable reconstruction errors, segmentation errors and local error distributions. A subspace analysis showed that the PCA and ICA subspaces describe nearly the same amount of variance in the dataset, indicating that there is a high degree of equivalence between ICA and PCA in segmentation applications.

Acknowledgements

M. Üzümcü is supported by grant IBV00303 from IOP, Dutch Ministry of Economic Affairs. A.F. Frangi is supported by a Ramón y Cajal Research Fellowship and grant TIC2002-04495-C02 from the Spanish Ministry of Science and Technology. B.P.F. Lelieveldt is supported by an Innovational Research Incentive 2001 grant from the Netherlands Organization for Scientific Research.

References

[1] T.F. Cootes, C. Taylor, A. Hill, J. Halsam, "The Use of Active Shape Models for Locating Structures in Medical Images", Proc. IPMI 1993, 33–47, 1993

[2] T.F. Cootes, G.J. Edwards, C.J. Taylor, "Active Appearance Models", Proc. of the ECCV, vol. 2, 484–498, 1998

[3] G. Edwards, C. Taylor, T. Cootes, "Interpreting face images using active appearance Models", Proceedings of the Third IEEE International Conference on Automatic Face and Gesture Recognition, 300–305, 1998

[4] S. C. Mitchell, B. P. F. Lelieveldt, R. J. van der Geest, J. G. Bosch, J. H. C. Reiber, and M. Sonka, "Multistage Hybrid Active Appearance Model Matching: Segmentation of Left and Right Cardiac Ventricles in Cardiac MR Images", IEEE TMI, vol. 20(5), pp 415–423, 2001

[5] S.C. Mitchell, J.G. Bosch, B.P.F. Lelieveldt, R.J. van der Geest, J.H.C. Reiber, M. Sonka, "3D Active Appearance Models: Segmentation of Cardiac MR and Ultrasound images", IEEE TMI, Vol. 21(9), 1167–1178, 2002

[6] T. F. Cootes, C. Beeston, G. J. Edwards, and C. J. Taylor, "A Unified Framework for Atlas Matching Using Active Appearance Models", LNCS Vol. 1613, 322–333, 1999

[7] T.F. Cootes and C.J. Taylor, "Statistical Models of Appearance for Computer Vision", available at:
$http://www.wiau.man.ac.uk/\ bim/Models/app\_model.ps.gz$, 2001

[8] H.H. Thodberg, "Hands on Experience with Active Appearance Models", Proc SPIE Medical Imaging, Vol. 4684, 495–506, 2002

[9] J.G. Bosch, S.C. Mitchell, B.P.F. Lelieveldt, F. Nijland, O. Kamp, M. Sonka and J.H.C. Reiber, "Automatic Segmentation of Echocardiographic Sequences by Active Appearance Motion Models", IEEE TMI Vol. 21(11), 1374–1383, 2002

[10] R. Beichel, G. Gotschuli, E. Sorantin, F. Leberl, M. Sonka, "Diaphragm Dome Surface Segmentation in CT Data Sets: A 3D Active Appearance Model Approach", Proc. SPIE Medical Imaging, Vol. 4684, 475–484, 2002

[11] Hyvärinen and E. Oja, "A Fast Fixed-Point Algorithm for Independent Component Analysis", Neural Computation, 9(7), 1483–1492, 1997

[12] M. Üzümcü, A.F. Frangi, J.H.C. Reiber, B.P.F. Lelieveldt, "Independent Component Analysis in Statistical Shape Models", Proc. SPIE 2003, 5032:375-383, 2003

[13] J.F. Cardoso, "Higher Order Contrasts for Independent Component Analysis", Neural Computation, 11(1), 157–192, 1999

[14] Hyvärinen, J. Karhunen and E. Oja, Independent Component Analysis, John Wiley & Sons, 2001

[15] T.F. Cootes, P. Kittipanya-ngam, "Comparing Variations on the Active Appearance Model Algorithm", Proc. BMVC, Vol.2, 837–846, 2002

[16] P.D. Sozou, T.F. Cootes, C.J. Taylor and E.C. Di Mauro, "A Non-Linear Generalisation of Point Distribution Models using Polynomial Regression", Image and Vision Computing Journal, 13(5):451–457, 1995

[17] C. Davatzikos, Xiadong Tao and Dinggang Shen, "Hierarchical Active Shape Models, Using the Wavelet Transform", IEEE Transactions on Medical Imaging, 22(3):414–423, 2003

[18] K. Takaya and K-Y Choi, "Detection of Facial Components in a Video Sequence by Independent Component Analysis", Proceedings of the 3rd International Conference on Independent Component Analysis and Blind Source Separation, San Diego, U.S.A., Eds. T-W Lee, T-P Jung, S. Makeig, T.J. Sejnowski, 266–271, 2001

[19] D. Yu and F. Sattar, "A New Blind Watermarking Technique Based on Independent Component Analysis", Lecture Notes in Computer Science, Vol. 2613/2003, IWDW 2002, Seoul, Korea, Eds. F.A.P. Petitcolas and H.J. Kim, 51–63, 2003

[20] V.D. Calhoun, T. Adali, G.D. Pearlson and J.J. Pekar, "Spatial and Temporal Independent Component Analysis of Functional MRI Data Containing a Pair of Task-Related Waveforms", Human Brain Mapping, Vol. 13, 43–53, 2001

[21] M.S. Bartlett, J.R. Movellan and T.J. Sejnowski, "Face Recognition by Independent Component Analysis", IEEE Transactions on Neural Networks, 13(6): 1450–1464, 2002

[22] M. Bressan, J.Vitrià. "Independent Modes of Variation in Point Distribution Models", In C. Arcelli, L.P. Cordella, G. Sanniti di Baja (Eds.): Visual Form 2001 4th International Workshop on Visual Form, IWVF4 Capri, Italy, Proceedings, Lecture Notes in Computer Science 2059, Springer Verlag, 123–134, 2001

[23] A. Suinesiaputra, M. Üzümcü, A.F. Frangi, T.A.M. Kaandorp, J.H.C. Reiber, B.P.F. Lelieveldt, "Extraction of Myocardial Contractility Patterns from Short-Axis MR Images using Independent Component Analysis", Medical Image Computing and Computer-Assisted Intervention MICCAI04. C. Barillot, D.R. Haynor, and P. Hellier (Eds.). Lecture Notes in Computer Science, Springer Verlag, Berlin, Germany, vol. 3216, 737–744, 2004

[24] M.R. Kaus, J. von Berg, J. Weese, W.J. Niessen, V. Pekar, "Automated segmentation of the left ventricle in cardiac MRI", Medical Image Analysis, 8(3): 245–254, 2004

[25] T.F. Cootes and C.J. Taylor, "Combining Elastic and Statistical Models of Appearance Variation", Proc. European Conference on Computer Vision, (1): 149–163, 2000

4

Detecting Regional Abnormal Cardiac Contraction in Short-Axis MR Images using Independent Component Analysis

In concealing others' faults be like the night

This chapter was adapted from:
Extraction of Myocardial Contractility Patterns from Short-Axis MR Images using ICA
A. Suinesiaputra, M. Üzümcü, A.F. Frangi, T.A.M. Kaandorp, J.H.C. Reiber, B.P.F. Lelieveldt
Lecture Notes in Computer Science, MICCAI '04. Eds: C. Barillot, D.R. Haynor, and P. Hellier. 3216: 737 – 744, 2004

Abstract

Regional myocardial motion analysis is used in clinical routine to inspect cardiac contraction in myocardial diseases such as infarction or hypertrophy. Physicians or radiologists can recognize abnormal cardiac motion because they have knowledge about normal heart contraction. This paper explores the potential of Independent Component Analysis (ICA) to extract local myocardial contractility patterns and to use them for the automatic detection of regional abnormalities. A qualitative evaluation was performed using 42 healthy volunteers to train the ICA model and 6 infarct patients to test the detection and localization. This experiment shows that the evaluation results correlate very well to the clinical gold standard: delayed-enhancement MR images.

4.1 Introduction

Identification of reversible myocardial ischemic injury is a crucial assessment before coronary revascularization. Myocardial infarction is characterized by the presence of hypo-kinetic regions. MRI images have been used widely to diagnose myocardial infarction, especially recently with the delayed-enhancement MRI [1].
The effect of coronary artery occlusion is an abnormal myocardial contraction, particularly in the infarcted regions. Figure 4.1 shows two examples of MRI images from a healthy volunteer and an infarct patient, both at end-systole. Note that the inferior region (indicated by a white arrow) of the infarct heart does not contract, and has a reduced wall thickness.

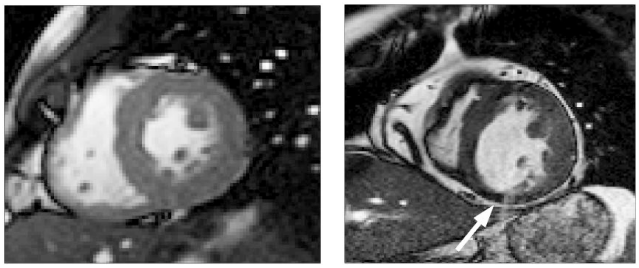

(a) healthy volunteer **(b)** infarct patient

Figure 4.1: MRI images of a healthy volunteer and an infarct patient at end-systole. The white arrow points to the infarcted tissue.

The goal of this work is to automate the detection of abnormal cardiac motion from short-axis MRI images. This is achieved by deriving a statistical model of normal heart contraction and its local contractility patterns. In this paper, ICA is used to model the normal heart contraction and to detect and localize regions of the abnormal contraction in a patient. The contributions of this paper are threefold:

- We propose a geometry-based sorting method of independent components, providing an intuitive anatomical interpretation of the ICA modes.
- We demonstrate the potential of ICA in cardiac shape modeling to detect local contraction abnormalities.
- We present a qualitative evaluation of the detection and localization of myocardial infarctions. Results are compared with the corresponding "gold-standard" delayed-enhancement MRI images.

Section 4.2 describes shape modeling with ICA, the new sorting method for independent components and the method to detect local abnormalities. In Section 4.3, qualitative evaluation results are presented, followed by a discussion in Section 4.4.

4.2 Methodology

4.2.1 ICA modeling of the normal cardiac contraction

ICA is originally used for finding source signals from a mixture of unknown signals without prior knowledge other than the number of sources. In machine learning, ICA has been applied for feature extraction [2] and face recognition [3]. ICA can be applied to statistical shape modeling to extract independent components of the shape variation [4].
ICA is a linear generative model, where every training shape can be approximated by a linear combination of its components.
Let $\vec{x} = (x_1, y_1, \ldots, x_m, y_m)^T$ be a shape vector, consisting of m pairs of (x, y) coordinates of landmark points. The linear generative model is formulated as follows:

$$\vec{x} \approx \bar{\vec{x}} + \vec{\Phi}\vec{b} \ . \tag{4.1}$$

The matrix $\vec{\Phi} \in \mathbb{R}^{2m \times p}$ defines the independent components (ICs) and $\vec{b} \in \mathbb{R}^p$ is the weight coefficient vector. The mean shape, $\bar{\vec{x}}$, is defined by

$$\bar{\vec{x}} = \frac{1}{n} \sum_{i=1}^{n} \vec{x}_i \ . \tag{4.2}$$

where n is the number of shapes and p is the number of retained components.
The goal of ICA is to find a matrix, $\vec{\Psi}$, such that

$$\vec{b} = \vec{\Psi} \left(\vec{x} - \bar{\vec{x}} \right) \tag{4.3}$$

with a constraint that columns of $\vec{\Psi}$ correspond to statistically independent directions. Thus the independent components are given by $\vec{\Phi} = \vec{\Psi}^{-1}$. The matrix $\vec{\Psi}$ is estimated by an optimisation algorithm (see [5] for survey of ICA).

Some pre-processing steps are necessarily performed before the ICA computation. The training shapes must be aligned, such that all shapes are invariant under Euclidean similarity transformations (rotation, translation and scaling). Procrustes analysis [6] is used for the shape alignment. Point correspondence between shapes is usually obtained by taking landmark points with the same anatomical interpretation. The resulting training shapes are zero mean, unit variance and all points are registered between shapes.
In this application, the observed data are left ventricular (LV) myocardial contours from short-axis cardiac MRI images at end-diastole (ED) and end-systole (ES) phases. To model the contractility pattern, contours for each subject are combined serially into one shape vector in the following order: endocardium contour at ED, epicardium contour at ED, endocardium contour at ES and epicardium contour at ES.

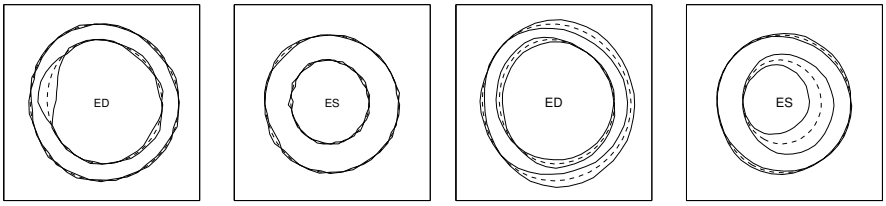

(a) ICA mode **(b)** PCA mode

Figure 4.2: Examples of modes from ICA and PCA models. The mean shape is drawn with a dashed line. The mode is drawn with a solid line. The shape variations are drawn with $\pm 3\sigma$ of the weight matrix distribution from the mean shape.

Figure 4.2(a) shows one example of an ICA derived shape variation mode. For comparison, the first mode of shape variation with PCA from the same data is shown in Fig. 4.2(b). ICA modes have a general shape of a local "bump", whereas the remainder of the shape is unaffected. This is an important property of ICA, which can be used to detect local shape anomalies. In contrast, PCA modes give global shape variations, distributed over the entire contour. A comparison study of ICA and PCA in cardiac shape modeling is given in [4].

4.2.2 Geometry-based sorting of independent components

In our study, ICA is used to detect regional abnormalities, which are extracted from local shape variations. It would give a benefit in this case, if the position of each IC can be determined. Thus ICs are ordered based on their positions along the whole contour, giving an anatomically meaningful interpretation.
Let $\hat{\vec{x}}_i$ be a shape vector from the i-th component

$$\hat{\vec{x}}_i = \bar{\vec{x}} + \vec{\Phi}\vec{a} \tag{4.4}$$

where $1 \leq i \leq p$, $a_i = 1$ and $a_j = 0$ for $j \neq i$. A *displacement* vector is defined as the

distance of each element of $\hat{\vec{x}}_i$ to the mean shape

$$d_i^{(j)} = \sqrt{\sum_{k=2j-1}^{2j} \left(\hat{\vec{x}}_i^{(k)} - \bar{\vec{x}}^{(k)} \right)^2} \quad \text{where } j = 1, 2, \ldots, m \ . \tag{4.5}$$

To determine the position of an independent component, a normalized circular cross-correlation is performed to each contour from the displacement vector with a bank of Gaussian filters. The parameter of the Gaussian filter giving the maximum response is stored for each component. The center of this filter defines the position of the component. Figure 4.3(a) shows an example of the cross-correlation response from a component.
There is an advantage of this sorting mechanism, that noise components can be detected. Noise components have a global wrinkled shape variation along the whole contour, which correlates best with the widest Gaussian filter. Figure 4.3(b) shows an example of the cross-correlation response for a noise component. Noise components are thus easily eliminated.
Figure 4.4 shows an example of the first four ICA modes after the geometry-based sorting mechanism. Note that the local shape variations are orderded clockwise.

4.2.3 Determining the number of independent components

One important parameter to determine is the number of independent components to estimate during the computation of ICA. Predicting this number with PCA may not always be a good idea, because PCA has a risk to eliminate "weak" ICs in the reduced data [7]. In shape modeling, this parameter affects appearance of the shape variations. As the number of computed ICs increases, the components represent more localized shape variations. If this parameter is too small, then the component gives global shape variation, much like PCA modes.
The determination of the optimal number of computed ICs is therefore task-specific. In this application to detect local abnormalities, we need sufficient regional seg-

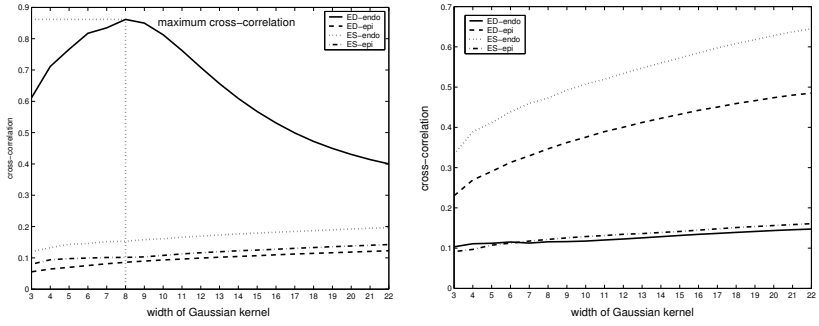

(a) A non-noise IC. **(b)** A noise IC.

Figure 4.3: Cross-correlation responses from two ICs.

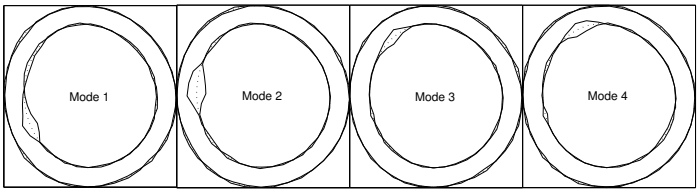

Figure 4.4: The first four sorted ICA modes.

ments. Too few segments will give an inaccurate localization. More segments will improve the detection resolution, but this is constrained by the computation time and the number of available shapes to avoid overlearning [8].
Figure 4.5 shows the number of segments as a function of the number of computed ICs from 42 shapes of normal hearts. From this, we took 40 as the number of computed ICs in our experiment, as it gives enough segments per contour.

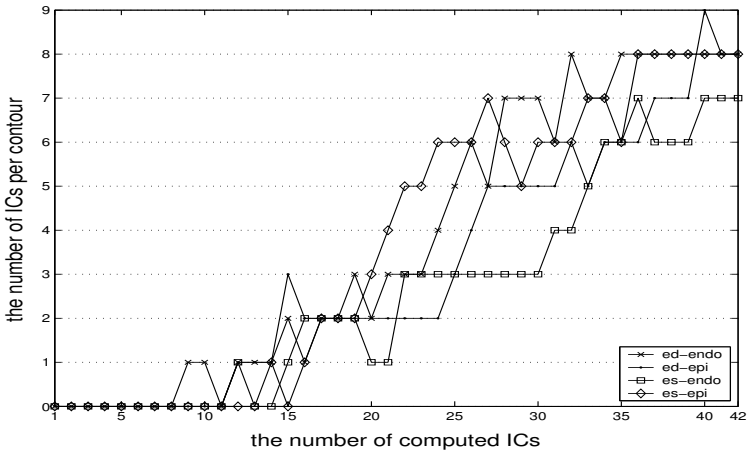

Figure 4.5: A plot of the number of ICs per contour as a function of the number of computed Independent Components.

4.2.4 Detection of abnormal contractility patterns

Let $\vec{y} \in \mathbb{R}^{2m}$ be a shape vector, fitted onto the mean shape of the model using the Procrustes fit [6]. The weight vector of the sample $\vec{y}$ is given by

$$\vec{b}_{\mathrm{y}} = \vec{\Phi}^{-1}\left(\vec{y} - \bar{\vec{x}}\right) \tag{4.6}$$

which represents the parameters approximating the patient shape. Patient anomalies are estimated by elements in the weight vector that lie outside the distribution of parameters of the ICA model.

We have made a statistical test to test the gaussianity for the distribution of coefficient values for each component. We can assume that all components have normal distribution.

We define the anomaly at the i-th component $q_{\mathrm{y}}^{(i)}$ as a value that falls beyond $\pm 3\sigma_i$ (99.7%), to make sure that the anomaly is an outlier. Thus the *anomaly vector* q_{y} is defined by taking the outlier components, normalized by their standard deviation. Each element of q_{y} is defined by

$$q_{\mathrm{y}}^{(i)} = \begin{cases} 0 & \text{if } -3\sigma_i \leq b_{\mathrm{y}}^{(i)} \leq 3\sigma_i \\ \dfrac{b_{\mathrm{y}}^{(i)}}{\sigma_i} & \text{otherwise} \end{cases} \qquad \text{for } i = 1, \ldots, p \tag{4.7}$$

The anomaly vector (4.7) is mapped to a shape vector to facilitate a more intuitive regional interpretation. From the sorted ICs, the corresponding Gaussian filters giving the maximum responses for each IC are known. These Gaussian filters are generated to model the local bumps, resulting in a mixture of Gaussian functions. The regional sum of the Gaussian mixture gives a shape vector that indicates regional abnormal heart contraction of a patient.

4.3 Experimental Results

An ICA model was constructed from 42 healthy volunteers. The mid-ventricular level from short-axis MRI was taken from each subject. Contours were drawn manually and resampled to 40 landmarks defined by equi-angular sampling, starting from the intersection between left and right ventricle. The calculation of ICA was performed using the JADE algorithm [9], implemented in Matlab. The optimal number of computed ICs with minimum of 7 segments per contour is 40 (see Fig. 4.5).

To evaluate the infarct detection and localization of our method, MRI data of 6 patients with all necrotic infarcts were investigated. Mid-ventricular short-axis (SA) MRI images and the corresponding delayed-enhancement (DE) MRI images with the same orientation and the distance only < 1 mm were acquired. Regional abnormal contraction was compared visually with the corresponding DE-MRI. The myocardial infarct regions in the DE-MRI are demonstrated by signal hyperenhancement, corresponding to myocardial necrosis [1].

Six representative evaluation results are presented in Fig. 4.6. The anomaly vectors of patients were projected to the corresponding myocardial regions. The contraction patterns are also shown in the plot of ED contours (solid line) and ES contours (dashed line). It is clearly seen from Fig. 4.6, that the dark areas have a reduced contraction. The corresponding DE-MRI are given in the right side where the infarction regions are depicted by hyperintensity regions.

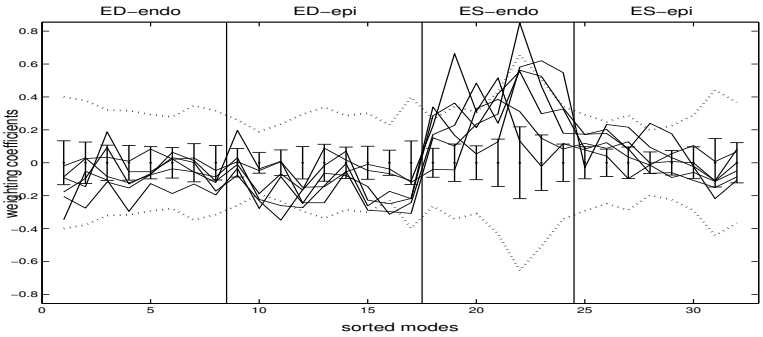

(a) Weight vectors (solid lines) of patients with the distribution of the ICA model (error bars). The dotted lines are the boundary of the normal contraction ($\pm 3\sigma_i$ for $i = 1, \ldots, p$).

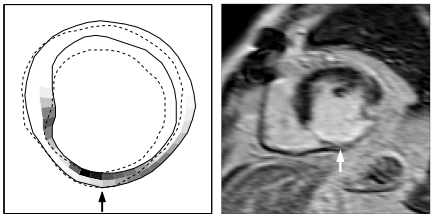

(b) Infarction in the inferior wall.

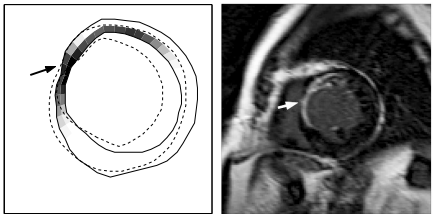

(c) Infarction in the septal wall.

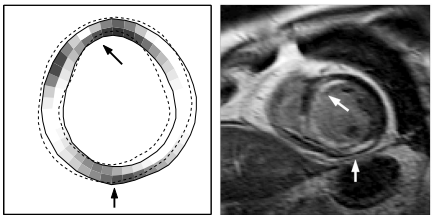

(d) Multiple infarctions.

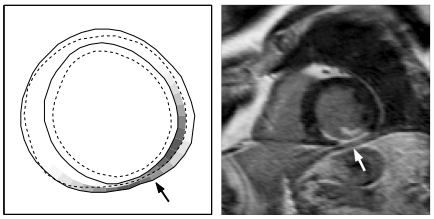

(e) Infarction in the inferior wall.

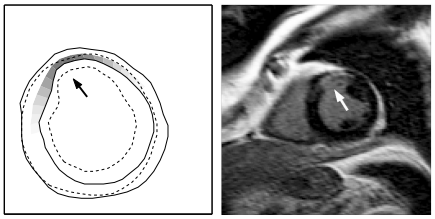

(f) Infarction in the septal wall.

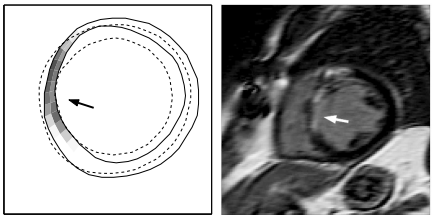

(g) Infarction in the septal wall.

Figure 4.6: Qualitative evaluation results. The top row figure shows projection of 6 patients to the ICA model of a normal heart. Their abnormalities are shown below in the myocardial regions (ED=solid, ES=dashed). Dark areas have high abnormality value, whereas white areas are normal. The corresponding DE-MRI images are shown at the right side.

4.4 Discussion

This study shows the potential of ICA as an analysis tool for extracting local shape deformation. Using ICA to train a model of normal cardiac contraction, both global and regional motions are captured. To this end, we can automatically distinguish between abnormal and healthy cardiac motion.
An intuitive anatomical interpretation of the normal contraction model is achieved by ordering the ICs of the model geometrically along the whole contour. From this, anatomical shape information can be inferred, providing a method to localize the motion abnormalities.
In the qualitative comparison for 6 patients, the hypo-kinetic regions show an excellent correspondence to the hyperintensity regions of the "gold standard" DE-MRI. This demonstrates that the ICA-based infarct detection and localization from short-axis MRI images is a promising technique for computer aided infarct localization.

References

[1] Kim, R., Wu, E., Rafael, A., et. al., "The Use of Contrast-Enhanced Magnetic Resonance Imaging to Identify Reversible Myocardial Dysfunction", New England Journal of Medicine 343 (2000) 1445–1454

[2] Hoyer, P.O., Hyvärinen, A., "Independent Component Analysis Applied to Feature Extraction from Colour and Stereo Images", Network: Computation in Neural System 11 (2000) 191–210

[3] Bartlett, M.S., Movellan, J.R., Sejnowski, T.J., "Face Recognition by Independent Component Analysis", IEEE Trans. on Neural Networks 13 (2002) 1450–1464

[4] Üzümcü, M., Frangi, A.F., Reiber, J.H., Lelieveldt, B.P., "Independent Component Analysis in Statistical Shape Models", In Sonka, M., Fitzpatrick, J.M., eds.: Proc. of SPIE. Volume 5032. (2003) 375–383

[5] Hyvärinen, A., "Survey on Independent Component Analysis", Neural Computing Surveys 2 (1999) 94–128

[6] Dryden, I.L., Mardia, K.V., "Statistical Shape Analysis", John Wiley & Sons (2002)

[7] Nadal, J.P., Korutcheva, E., Aires, F., "Blind Source Separation in the Presence of Weak Sources", Neural Network 13 (2000) 589–596

[8] Hyvärinen, A., Särelä, J., Vígario, R., "Bumps and Spikes: Artifacts Generated by Independent Component Analysis with Insufficient Sample Size", In: Proc. Int. Workshop on ICA and BSS. (1999) 425–249

[9] Cardoso, J., Souloumiac, A., "Blind Beamforming for Non Gaussian Signals", IEEE Proceedings-F 140 (1993) 362–370

5

Multi-view Active Appearance Models for Simultaneous Segmentation of Cardiac 2- and 4-Chamber Long-axis Magnetic Resonance Images

In anger and fury be like dead

This chapter was adapted from:
Multi-View AAMs for Simultaneous Segmentation of Cardiac 2- and 4-chamber Long Axis MR Images
M. Üzümcü, R.J. van der Geest, M. Sonka, H.J. Lamb, J.H.C. Reiber, B.P.F. Lelieveldt
Investigative Radiology, 40(4): 195 – 203, 2005

Abstract

Long-axis cardiac MR views enable a rapid, online evaluation of cardiac function from only two views. This paper aims to evaluate a model-based method for simultaneous detection of 2- and 4-chamber endocardial and epicardial contours in end-diastolic and end-systolic phases of MR Images.

This paper introduces Multi-View Active Appearance Models for the automated segmentation of long axis cardiac MR images of the left ventricle. Two modes of initialization were used to test the accuracy of the model with minimal user interaction and the best obtainable accuracy with this model. The segmentation was initialized by annotating two points in the base and one in the apex. The method's performance was tested by comparing the point-to curve errors, ejection fractions and bi-plane area-length volumes calculated with the automatically detected contours to those calculated from contours that were annotated manually by experts. Leave-one-out experiments were performed with 2- and 4-chamber long axis MR images of 59 subjects in end-diastolic and end-systolic phases.

When initializing in all four frames, 97% of the segmentations were successful and the standard deviation in the volume-errors with respect to the average manually-identified volume was 9.0% for the end-diastolic volumes and 15% for the end-systolic volumes. When the method was initialized in the end-systolic frames only, 92% of the segmentations were successful and the standard deviation in the errors in the volumes with respect to the average manually-identified volume was 13.3% for the end-diastolic volumes and 16.7% for the end-systolic volumes. Blant-Altman plots showed that the errors were distributed randomly around 0 and a paired t-test comparing manual and computer determined volumes showed that the volume differences were not significant. Simultaneous detection of the endocardial and epicardial contours in 2- and 4-chamber views and end-diastolic and end-systolic phases for one subject takes approximately 3 seconds.

The accuracy of the reported method is comparable with the interobserver variability for initialization in all frames and slightly worse than the interobserver variability with initialization in the end-systolic frames only. However, in both cases the errors were not significant. Initialization in end-systolic frames only leads to a statistically insignificant lower model accuracy, however, requires only half the user interaction. Therefore, we can conclude that this method enables rapid analysis of the cardiac left ventricular function with little user interaction.

5.1 Introduction

In recent years, imaging modalities such as MRI and CT are frequently applied to the analysis of cardiac function [16, 17, 18]. These modalities enable the acquisition of 3-dimensional (3D) and 4-dimensional (3D + time) images of the heart, from which detailed diagnostic information can be derived. However, these modalities generate

large amounts of data: 4D cardiac MR studies e.g. may easily consist of 200-500 images and a 4D CT study may even consist of 3000 images or more. In clinical practice first a 2-chamber and a 4-chamber long-axis view are acquired to plan the short-axis image acquisition, which is commonly used to evaluate global and regional cardiac function. However, the quantitative analysis of short-axis acquisitions is time consuming, because a short-axis acquisition consists of approximately 10-15 slices. To obtain an estimate of cardiac function parameters, contours in all slices in at least end-diastolic and end-systolic phases need to be drawn. Alternatively, from the 2- and 4-chamber long-axis acquisitions in end-diastolic and end-systolic phases, i.e. 4 images only, clinically relevant global functional parameters, such as ejection fraction (EF) and stroke volume, can be derived. Though bi-plane MRI is subject to the limitations of geometric assumptions and therefore is less suitable for regional function analysis, it still is attractive, because it only requires two views. This enables a rapid, online (while the patient is still in the scanner) way of assessing global cardiac function. Short-axis images are less suitable to this end: though short-axis views are regarded as a gold-standard for global and regional analysis, the large amount of data to process for computing global functional parameters is a bottleneck for on-line application. Furthermore, in long-axis acquisitions the base and apex are defined more accurately, which is not the case in short-axis acquisitions.

Previous studies have shown that in most cases there are no significant differences in the volumes calculated with volumetric MRI, which is calculated from a stack of short-axis MR images, and bi-plane MRI, which is calculated from the 2- and 4-chamber long-axis MR images [10, 11, 12]. Though this is still an open debate in the clinical community, considering this previous work, we assume that bi-plane MR acquisition is a valid protocol for establishing volume estimates.

The goal of this work is the development of a semi-automatic contour detection method for rapid evaluation of global cardiac function using routinely acquired 2- and 4-chamber long-axis cardiac MR images. It was not our aim to demonstrate a correlation between long-axis bi-plane MR volumes and volumes determined from short-axis MR stacks since this has been evidenced by several others [10, 11, 12]. Therefore, we have limited ourselves to rapid analysis of global function parameters, because long-axis MR acquisitions are less suitable for determination of regional abnormalities than short-axis MR scans.

The method introduced in this work, Multi-view Active Appearance Models incorporates prior knowledge about shape and gray values in images as well as information about the correlation between different views. Previously, several model-driven segmentation methods have been developed for automatic contour detection of the heart in various image modalities, e.g. based on deformable models [1, 2, 3, 4], Active Shape Models [8] and Active Appearance Models [5, 6]. However, these methods have been applied only to cardiac MR short-axis views. Also the computational burden of these methods is currently too high for online application (3-5 minutes computation time).

This work represents the first study towards methods for performing automated analysis of cardiac function using cardiac MR long-axis views, potentially enabling online global function quantification.

5.2 Materials and Methods

5.2.1 Active Appearance Models

Model generation

Active Appearance Models (AAM), introduced by Cootes *et al.* [7], incorporate prior knowledge about shape and gray values in images. Mainly because of this integration of shape and gray value knowledge, AAMs have shown good performance on face recognition problems and have demonstrated high robustness for detecting contours of the left ventricle of the heart in static short-axis cardiac MR [5] and echocardiographic images [8, 9].
AAMs describe statistical variations of shape and gray value and are trained from a set of example images, in which corresponding landmark points are annotated. The shapes, which are spanned by the landmarks, are aligned using Procrustes analysis to compensate for translation, rotation and scaling differences between the shape samples by minimizing the squared distance between corresponding points in the shape samples. Of this set of aligned shapes, the mean shape is calculated, and modes of shape variation are computed using Principal Component Analysis (PCA). In addition, the gray values inside the shapes are sampled, warped onto the mean shape and subsequently intensity normalized. Again, a mean intensity patch and its characteristic principal components are computed for the set of example images. Each shape sample is subsequently expressed as a set of shape coefficients b_s and intensity coefficients b_i: the total appearance of an object can then be represented with an appearance coefficient vector b_a, which is defined in the following manner:

$$b_a = \begin{pmatrix} W_s b_s \\ b_i \end{pmatrix} \tag{5.1}$$

where weighting matrix W is a diagonal matrix that relates the different units of shape and gray level intensity coefficients.
By applying a PCA to the set of b_a vectors for the complete training set, new appearance samples a can be synthesized as follows:

$$a = \bar{a} + Q_a \cdot b_a \tag{5.2}$$

where b_a is the vector that contains the coefficients weighing the appearance eigenvectors Q_a.

Model search

The model described in the previous section represents a compact description of the variation over the training set, and such a model can (re-) generate any likely shape and/or appearance by varying the eigenvector coefficients. By comparing a real, unseen image with such a synthetically generated image and iteratively adapting the model pose and eigenvector coefficients using a gradient descent approach, an approximation of the shape in this image can be found fully automatically.
To perform model search on an unseen example, a sample image is generated by choosing appropriate model coefficients b_a. The similarity measure for model generated and target images is the root mean square (RMS) grey value difference between the generated image and the unseen example. Minimizing this similarity measure is a multi-dimensional optimization problem; the dimensionality is determined by the number of modes retained in the model. With the pre-computed derivative matrix, the required parameter updates for the AAM can be estimated, such that the difference between the model and the unseen image is minimized. After updating the parameters, a new image is generated and this process is iterated until a convergence criterion is reached, i.e. when there is no more improvement in the RMS grey value error between the generated sample and the unseen image.
A high dimensional optimization method as used for our model matching technique is inherently sensitive to local minima. Therefore, it is important to initialize the model matching in a position close to the final solution.

5.2.2 Multi-view AAMs

In Multi-view AAMs, a-priori information about the correlation between different phases, e.g. end-diastolic and end-systolic, and views, e.g. 2-chamber and 4-chamber, is incorporated in the model. All frames from the different views and phases are first aligned separately for each view and phase using Procrustes alignment. After the alignment, the shape vectors x_i from the N different views and phases from one subject are concatenated in one shape vector:

$$x = (x_1^T, x_2^T, x_3^T, ..., x_N^T) \tag{5.3}$$

where x is the shape vector containing the coupled views and phases and N is the total number of views and phases. A PCA is performed on the concatenated shape vectors to find the main directions of shape variation. Analogous to the shape part of the model, the aligned grey values from the N views and phases from one subject are concatenated in one grey value vector:

$$g = (g_1^T, g_2^T, g_3^T, ..., g_N^T) \tag{5.4}$$

and a PCA is performed on the concatenated grey value vectors to find the main directions of grey value variation. This way, the shape and grey value variations are

correlated for the different views and phases. The training of the appearance model is similar to the AAM for single frames. Figure 5.1 shows the coupled variation of the 2-chamber end-diastolic (top) and end-systolic (bottom) frames when corresponding weights are varied between -2σ (left) and $+2\sigma$ (right). The variations for end-diastolic and end-systolic 4-chamber views are also coupled to these variations.

5.3 Evaluation

The model described in the previous section enables a simultaneous contour detection in multiple views and phases of the cardiac cycle. The models used for the evaluation consisted of 4 frames, i.e. 2-chamber and 4-chamber cardiac MR views in end-diastolic and end-systolic phases.

5.3.1 Data

To investigate the clinical potential of the Multi-View AAM for segmentation of cardiac MR long-axis views, studies were collected from 59 subjects. To prove the general applicability of the method, patients with a range of pathologies were selected: 32 subjects were diagnosed with older, stabilized infarcts, 13 with acute myocardial infarcts, 12 with mitral valve regurgitation (confirmed with echocardiography) and 2 were healthy subjects. Two clinically standardized views (i.e. the 2-chamber and 4-chamber views) from cine studies were used, which were acquired using a Balanced FFE protocol on a 1.5T Philips Gyroscan Intera scanner (Philips Medical Systems, Best, The Netherlands) using the following parameter settings: TE = 1.41 ms, TR = 2.82 ms and flip angle = 50 degrees. In Fig. 5.2, example images are shown. Images were acquired with slice thickness of 8 mm, a resolution of 256^2 pixels and field of view ranging from 350 to 480 mm, i.e. pixel sizes varied from 1.37 to 1.88 mm. The end-systolic and end-diastolic images of the 2-chamber and 4-chamber views were used for the training and evaluation of the model. Endocardial and epicardial contours were manually drawn by a radiologist with over three years cardiac MR experience . The contours were drawn in all phases and slices using the MASS software package (Medis medical imaging systems, Leiden, The Netherlands). Contours were resampled to 80 landmarks, i.e. 40 endocardial and 40 epicardial landmarks.

5.3.2 Leave-one-out validation

A leave-one-out approach was used to validate the Multi-view AAM algorithm. Models were trained on the contour and image data of 58 subjects and the matching performance was evaluated on the one left out subject. This process was repeated 59 times, always leaving out a different subject, which was then used for validation. In the model generation, the number of modes was determined automatically by retaining 98% of both shape and grey value variances.

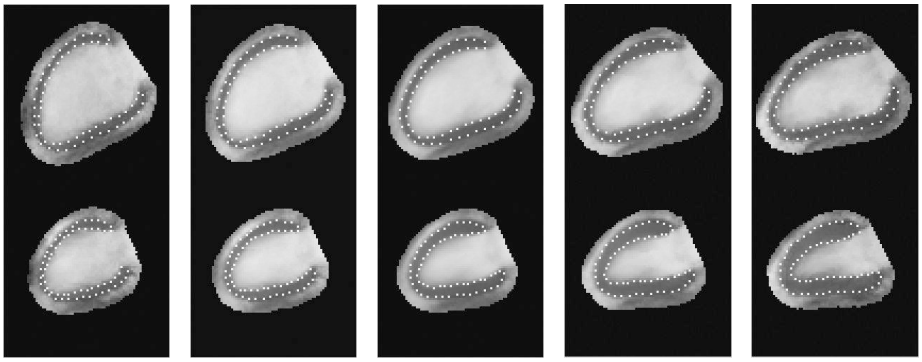

Figure 5.1: First eigenvariation of the multiview AAM. Variation between -2σ (a) and $+2\sigma$ (e) of the eigenvector is shown for 2-chamber end-diastolic (top) and end-systolic (bottom). Eigenvariations of the 4-chamber views are also coupled to the shown eigenmode

5.3.3 Matching

Modeling and matching was performed for 4 views simultaneously: ED and ES for the 2-chamber and 4-chamber views. The model was initialized manually by annotating three points, i.e. 2 points in the base and the apex location of the cardiac left ventricle. Our objective for the evaluation was twofold - to quantify the optimal accuracy with the Multi-View AAM and to quantify the accuracy of the model with minimal user interaction. Therefore, two types of initialization were evaluated; annotating points in all frames and in only the 2- and 4-chamber end-systolic frames. Epicardial and endocardial contours in all frames were detected simultaneously in an iterative process. Iterations stopped when the quadratic image intensity error was not minimized any further. The detected final contours were compared to the manually defined independent standard.

5.3.4 Qualitative evaluation

After completing the model match to automatically detect the endocardial and epicardial contours in all frames, the segmentation results were visually inspected. The results of the visual inspection were divided into three categories:

1. no frames failed
2. 1 frame failed
3. multiple frames failed

Subjects, for which segmentation failed in multiple frames, were reported and discarded from quantitative analysis. Also when contour detection for a certain subject failed in only 1 frame, this subject was excluded from further quantitative evaluation, although the other frames might have been segmented correctly.

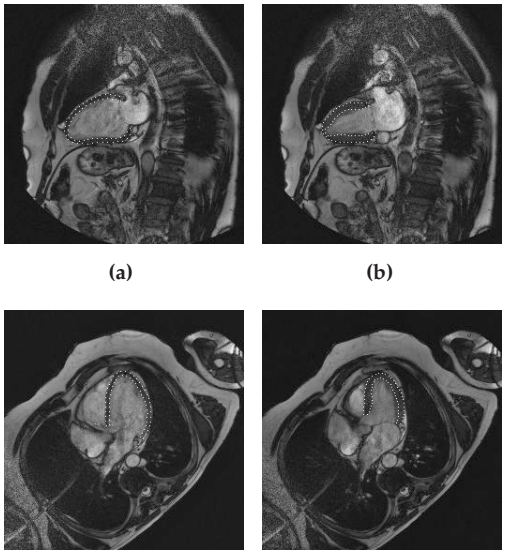

Figure 5.2: Long-axis images of end-diastolic (left) and end-systolic (right) phases of the 2-chamber (top) and 4-chamber (bottom) views. Expert-drawn endocardial and epicardial contours are denoted

5.3.5 Quantitative evaluation

To quantify the matching accuracy of the model, the automatically detected contours were compared with the manually defined expert contours on the basis of the point-to-curve border positioning errors, the bi-plane area length volume and the EF. The point-to-curve errors are defined as the shortest distance between an automatically detected landmark and the manually drawn contour, i.e. the distance along the normal to the manually drawn curve. The bi-plane area length volume of the cardiac left ventricle is defined as follows [10]:

$$V = \frac{8}{3\pi} \cdot \frac{A_{2ch} \cdot A_{4ch}}{L_{min}} \tag{5.5}$$

where V denotes the bi-plane area length volume, A_{2ch} the area of the endocardial contour of the 2-chamber view, A_{4ch} the area of the endocardial contour of the 4-chamber view and L_{min} the smallest distance between the apex and the base for the 2 views. The ejection fraction is defined as follows:

$$EF = \frac{V_{ED} - V_{ES}}{V_{ED}} \tag{5.6}$$

where EF is the ejection fraction, V_{ED} the bi-plane area length volume in end-diastolic phase and V_{ES} the bi-plane area length volume in end-systolic phase.

5.3.6 Statistical Analysis

To quantify the point-to-curve border positioning errors, the median and the 90-percentile were calculated for all views and phases over all accepted matches. Using the areas of the endocardial contours and the lengths of the long-axis of the 2- and 4-chamber views, bi-plane area length volumes were calculated for the end-diastolic and end-systolic phases. A linear regression was performed to find the correlation between the volumes of the manually drawn and the automatically detected contours. Bland-Altman plots were generated to quantify the errors in the volumes and to check for any systematic errors or trends. Finally, paired t-tests were performed to check if the errors were statistically significant. A p-value < 0.05 was considered as statistically significant.

5.4 Results

The leave-one-out validation resulted in 59 automatically detected segmentation results, in which the epicardial and endocardial contours of the left ventricle of the heart are depicted in end-diastolic and end-systolic phases of the heart cycle. Figures 5.3 and 5.4 show examples of automatically detected contours. The segmentation was performed simultaneously on 2- and 4-chamber, end-diastolic and end-systolic frames.

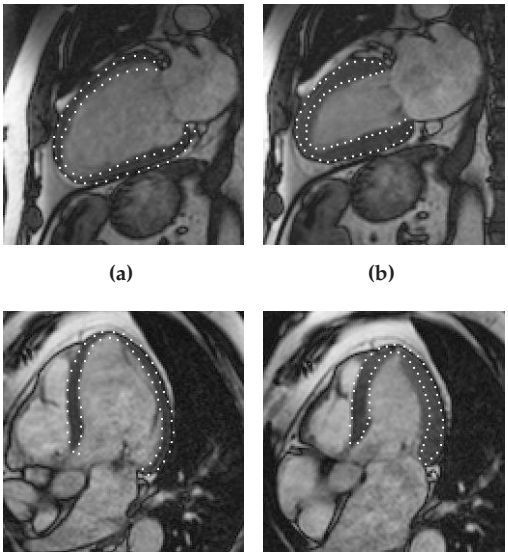

Figure 5.3: Representative example of automatically generated contours in (a) 2-chamber end-diastolic, (b) 2-chamber end-systolic, (c) 4-chamber end-diastolic, and (d) 4-chamber end-systolic long-axis MR images of the left ventricle of the heart. Contours were detected simultaneously in all frames

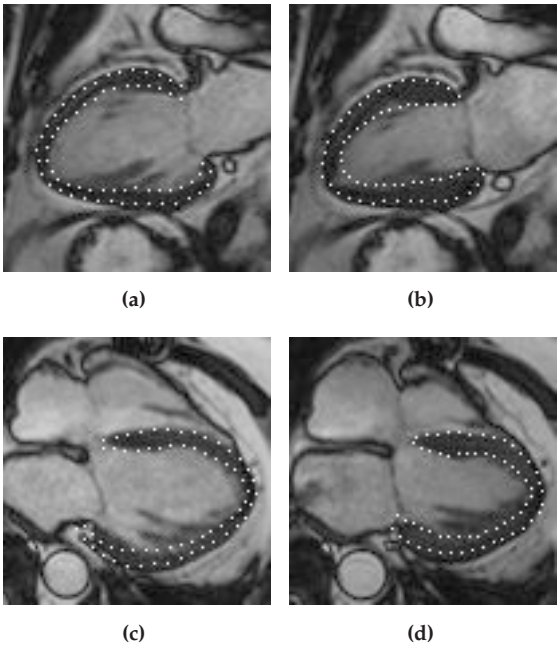

Figure 5.4: Representative example of automatically generated contours in (a) 2-chamber end-diastolic, (b) 2-chamber end-systolic, (c) 4-chamber end-diastolic, and (d) 4-chamber end-systolic long-axis MR images of the left ventricle of the heart. Contours were detected simultaneously in all frames

For the leave-one-out tests with full initialization, i.e. annotating twelve points in total for all frames, for 57 out of 59 cases (97 %) visually correct segmentation results were obtained in a semi-automatic manner.
In 2 cases visually incorrect results were obtained in one frame, i.e. the 4-chamber end-systolic frame. With initialization for the end-systolic frames only, i.e. annotating six points in total, for 54 out of 59 cases (92 %) visually correct segmentation results were obtained. In five cases segmentation failed in multiple frames. In total, 236 frames were segmented. The model matching converged in approximately 8 iterations. Simultaneous detection of endocardial and epicardial contours in four frames takes approximately three seconds; this enables an online cardiac function analysis. After leaving out the visually incorrect matches, the point-to-curve border positioning errors for both types of initialization were computed (Table 5.1)
The bi-plane area length volumes for the manual and automatically detected contours are shown in Table 5.2. This table shows that by initializing in the end-systolic frames only, the standard deviations of the errors for both end-diastolic and end-systolic volumes increase slightly.
The results of the linear regression fits for the bi-plane area length volumes are shown in Table 5.3. In general, the regression fits are good. However, the regression fits for the ejection fractions are less accurate, which is caused by the fact that

the errors in both end-diastolic volumes and end-systolic volumes are accumulated in the calculation of the EF.

Table 5.1: Point-to-Curve border positioning errors for 2- and 4-chamber views in end-diastolic and end-systolic phases

		Error			
		2-Chamber		4-Chamber	
Initialization	**Phase**	**Median (mm)**	**90%-ile**	**Median (mm)**	**90%-ile**
All frames	End-diastolic	1.66	2.86	1.77	2.94
(n=57)	End-systolic	2.12	3.62	2.07	3.25
ES frames	End-diastolic	1.89	2.94	1.98	3.79
(n=54)	End-systolic	2.09	3.27	2.00	3.30

When initializing in all frames, 3 outliers were discarded and when initializing in ES frames only, 6 outliers were discarded in the error computation.

Table 5.2: Bi-plane area-length volumes. Difference between volumes calculated from manually drawn and automatically detected contours and the results of the T-test

		Manual		Automatic		Error		
		Average	**SD**	**Average**	**SD**	**Average**	**SD**	
Initialization	**Phase**	**(mL)**	**(mL)**	**(mL)**	**(mL)**	**(mL)**	**(mL)**	**P Value**
All frames	ED	89.85	30.42	89.78	29.65	0.06	8.07	0.95
(n=57)	ES	49.17	29.28	48.27	26.47	0.90	7.38	0.36
ES frames	ED	91.87	30.73	91.25	34.86	0.62	12.22	0.71
(n=54)	ES	52.01	29.73	51.22	29.41	0.80	8.69	0.50

The difference in the average volumes calculated from manually drawn contours for both types of initialization is caused by the fact that in both cases a different number of subjects were left out.

The ejection fractions for the 2 types of initialization were compared. Table 5.4 shows the average EFs calculated from manually drawn contours, from automatically detected contours and the errors that were made by the Multi-view AAM method. Bland-Altman plots in Figures 5.5 and 5.6 show the errors of the EFs from the automatically detected contours compared to the expert drawn contours. These figures show that there is no systematic over- or underestimation as the errors are distributed randomly around 0.

5.5 Discussion

The results of the validation study presented in this work show the potential for an automated analysis of global cardiac function from bi-plane long-axis cardiac MR images. When initializing in all frames, good results were obtained in more than

Table 5.3: Linear regression fits for bi-plane area-length volumes in end-diastolic, end-systolic volumes and for ejection fractions

Initialization	Volume/Ejection Fraction	Regression Fit	R^2
All frames	End-diastolic (mL)	$y = 0.94x + 5.34$	0.93
(n=57)	End-systolic (mL)	$y = 0.88x + 5.15$	0.94
	Ejection Fraction (%)	$y = 0.81x + 9.42$	0.82
ES frames	End-diastolic (mL)	$y = 1.06x - 6.55$	0.88
(n=54)	End-systolic (mL)	$y = 0.95x + 1.99$	0.92
	Ejection Fraction (%)	$y = 0.70x + 14.39$	0.72

Table 5.4: Comparison of ejection fractions (EFs) for initialization in all frames and in end-systolic (ES) frames only

	Manual EF		Automatic EF		Error		
Initialization	Average (%)	SD	Average (%)	SD	Average (%)	SD	P Value
All frames (n=57)	47.09	16.70	47.58	14.99	-0.49	7.18	0.60
ES frames (n=54)	45.12	15.94	45.93	13.14	-0.82	8.44	0.48

96% of the subjects. The errors between manually annotated and automatically detected contours were not statistically significant. With minimal user interaction, i.e. initializing in the end-systolic frames only, the Multi-view AAM method performed well in more than 92% of the subjects on the simultaneous segmentation of 2- and 4-chamber views in end-diastolic and end-systolic phases of the cardiac cycle. Though there are more outliers, initializing only in the end-systolic frames leads to a slightly less accurate result; however, this requires half the user interaction.

The accuracy of the Multi-view AAM was compared to the variation between multiple observers. In [10] the interobserver variability was determined by having multiple observers draw contours for 2- and 4-chamber long axis MR images and calculating the bi-plane area length volumes from these contours. Reported interobserver variabilities for bi-plane MRI volume calculations are 9.4% for end-diastolic volumes and 12.5% for end-systolic volumes. In the bi-plane area length volumes obtained with initialization in all frames, the standard deviation of the errors with respect to the average volume is 9.0% for end-diastolic volumes and 15.0% for end-systolic volumes. In case of initialization in end-systolic frames only, the standard deviation of the errors with respect to the average volume is 13.3% for end-diastolic volumes and 16.7% for end-systolic volumes. With initialization in all frames, the variability of the proposed method is comparable to the interobserver variabilities reported. With initialization in end-systolic frames only, the error increases. This is due to the fact that the initial position in the end-diastolic phase is further from the optimal position. Hence, the model is more sensitive for locking in local minima.

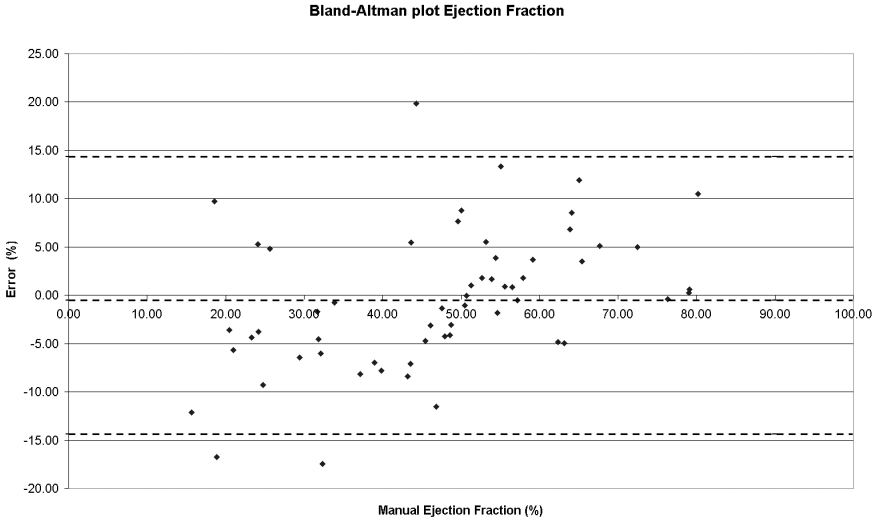

Figure 5.5: Bland-Altman plot for manual versus automatic ejection fractions with initialization in all frames.

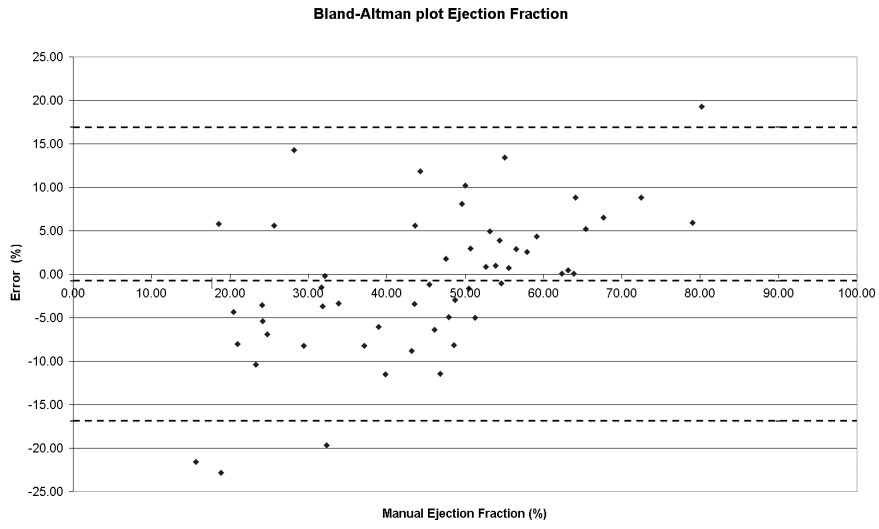

Figure 5.6: Bland-Altman plot for manual versus automatic ejection fractions with initialization in end-systolic frames only.

However, when initializing in end-systolic frames only, minimal user interaction is required for initialization.

Also, from the P-values in Table 5.2 can be seen that the errors in the bi-plane area length volumes are not significant, as all P-values are greater than 0.05. For the ejection fractions, the average error and the standard deviation in the errors were relatively small compared to the average manual ejection fraction. The respective P-values were 0.60 and 0.48 for initialization in all frames and in ES frames only, indicating that the differences between the manually and automatically determined ejection fractions are not statistically significant. In [10] the standard deviation in the differences in left ventricular ejection fractions between various observers is reported as 5.9%. For both types of initialization the standard deviations for the presented method are comparable to this interobserver variability. In [5] the reported point-to-curve border positioning errors for segmentations of 2D cardiac short axis MR images in end-diastolic phase were 1.71 ± 0.82 mm for endocardial contours and 1.75 ± 0.83 mm for epicardial contours. The border positioning errors for cardiac long-axis MR images presented in Table 5.1 show excellent correspondence to the accuracy presented in literature.

As can be seen from the results, the segmentation results are globally very good. However, in some cases the contour detection results in local errors. Figure 5.7 shows an example, where the contours are globally segmented very accurately, however the edges near the apex were not detected correctly. These local errors are due to the fact that a principle component analysis is used in the AAM. The PCA results in global shape descriptions and therefore the AAM cannot describe local shape variations very accurately. However, this may be resolved by applying a subsequent post-processing step to the segmentation result. Using a local or hybrid AAM would not solve these kinds of errors, as these methods also are based on PCA as proposed in [5]. Other sources of error may be a large intensity gradient due to the use of a surface coil during image acquisition. Also, the occurrence of non-representative pathological cases in the dataset (i.e. rare cases not included in the training set), may adversely influence the performance of the proposed method.

Previously, automatic segmentation methods have been presented for the analysis of cardiac function. Also software is commercially available to this end. However, these methods are only applicable to short-axis images of the heart. For instance, in [13] the ARGUS A1.5 from Siemens Medical Systems was used for comparing the automatically determined LV mass with the true LV mass in dogs and pigs. In [14] and [6] automatic methods for segmentation of the cardiac left ventricle were presented. However, these tools and methods were developed for short-axis image segmentation and are computationally intensive and time-consuming, though with the increase of computer speed and fast MR protocols [15], this issue may become less important. However, as yet, analysis of cardiac function using these methods is performed off-line. Short-axis acquisitions are still considered as the gold standard for global and regional analysis of cardiac function; however, the method presented in this paper offers an alternative for rapidly assessing information about global car-

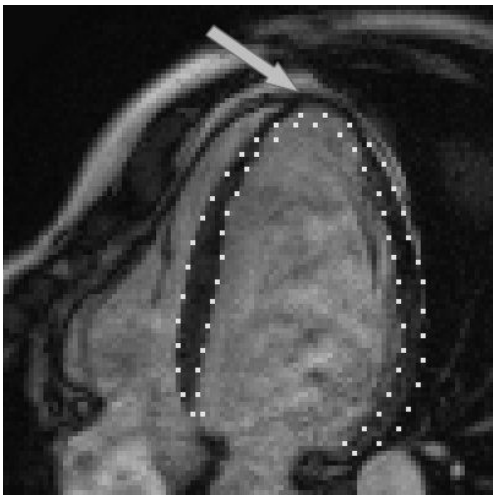

Figure 5.7: Example of local segmentation errors. A 4-chamber end-diastolic frame is shown, where overall contours are very accurate; however, locally the apex is not segmented correctly.

diac function, while the patient is still in the scanner.
To our knowledge no prior method has been presented for the analysis of LV volume and EF with bi-plane MR images of the 2- and 4-chamber cardiac long axis. The method presented in this paper performs very well compared to interobserver reproducibilities as reported in literature [10]. Initializing in the end-systolic frames only does not lead to substantially greater errors, the regression fits for the bi-plane area length volumes are still good and the errors in the volumes are not significant. These findings support the conclusion that using Multi-view AAMs, rapid analysis of cardiac function can be performed. Including all user interaction, global parameters such as EF, stroke volume and cardiac output can be obtained within 20 seconds, enabling online global cardiac function analysis.
The presented method is highly suitable for rapid online quantification of global cardiac function with minimal user interaction. Our method can be generalized towards short-axis MR acquisitions. The combination of both long- and short-axis acquisitions will enable an optimal quantification of both global and regional cardiac function.

References

[1] Staib L, Duncan JS. "Model-based Deformable Surface Finding for Medical Images", IEEE Transactions on Medical Imaging, 1996; 15(5):720–731

[2] McInerney T, Terzopoulos D. "Deformable Models in Medical Image Analysis: A Survey", Medical Image Analysis, 1996; 1(2):91–108

[3] Tagare HD, "Deformable 2-D template matching using orthogonal curves", IEEE Transactions on Medical Imaging, 1997; 16:108–117

[4] Lötjönen J, Magnin IE, Reinhardt L, *et al.* "Model Extraction from Magnetic Resonance Volume Data Using the Deformable Pyramid", Medical Image Analysis, 1999; 3:387–406

[5] Mitchell SC, Lelieveldt BPF, Van der Geest RJ, *et al.* "Multistage Hybrid Active Appearance Model Matching: Segmentation of Left and Right Cardiac Ventricles in Cardiac MR Images", IEEE Transactions on Medical Imaging, 2001; 20(5):415–423

[6] Mitchell SC, Bosch JG, Lelieveldt BPF, *et al.* "3-D Active Appearance Models: Segmentation of Cardiac MR and Ultrasound Images", IEEE Transaction on Medical Imaging, 2002; 21:1167–1178

[7] Cootes TF, Edwards GJ, Taylor CJ. "Active Appearance Models", IEEE Transactions on Pattern Analysis and Machine Intelligence, 2001; 23(6):681–685

[8] Cootes TF, Hill A, Taylor CJ, *et al.* "The Use of Active Shape Models for Locating Structures in Medical Images", Image and Vision Computing, 1994; 12(1):47–59

[9] Bosch JG, Mitchell SC, Lelieveldt BPF, *et al.* "Automatic Segmentation of Echocardiographic Sequences by Active Appearance Motion Models", IEEE Transactions on Medical Imaging, 2002; 21:1374–1383

[10] Chuang ML, Hibberd MG, Salton CJ, *et al.* "Importance of Imaging Method over Imaging Modality in Noninvasive Determination of Left Ventricular Volumes and Ejection Fraction", Journal of the American College of Cardiology, 2000; 35(2):477–484

[11] Dulce MC, Mostbeck GH, Friese KK, *et al.* "Quantification of the Left Ventricular Volumes and Function with Cine MR Imaging: Comparison of Geometric Models with Three Dimensional Data", Radiology, 1993; 188:371–376

[12] Van Pol P, Foster R, Davis N, *et al.* "Optimal Clinical Evaluation of Left Ventricular Function Using MRI", Circulation, 1997; 96 Suppl. I:I-514

[13] Francois CJ, Fieno DS, Shors SM, *et al.* "Left Ventricular Mass: Manual and Automatic Segmentation of True FISP and FLASH Cine MR Images in Dogs and Pigs", Radiology, 2004; 230:389–395

[14] Aladl UE, Hurwitz GA, Dey D, *et al.* "Automated Image Registration of Gated Cardiac Single-Photon Emission Computed Tomography and Magnetic Resonance Imaging", Journal of Magnetic Resonance Imaging, 2004; 19:283–290

[15] Spuentrup E, Mahnken AH, Kuhl HP, *et al.* "Fast interactive real-time magnetic resonance imaging of cardiac masses using spiral gradient echo and radial steady-state free precession sequences", Invest Radiol. 2003; 38:288–292

[16] Fenchel M, Kramer U, Helber U, *et al.* "Semiquantitative Assessment of Myocardial Perfusion Using Magnetic Resonance Imaging: Evaluation of Appropriate Thresholds and Segmentation Models", Invest Radiol. 2004; 39:572–581

[17] Mahnken AH, Henzler D, Klotz E, *et al.* "Determination of Cardiac Output With Multislice Spiral Computed Tomography: A Validation Study", Invest Radiol. 2004; 39: 451–454

[18] Dewey M, Kaufels N, Laule M, *et al.* "Magnetic Resonance Imaging of Myocardial Perfusion and Viability using a Blood Pool Contrast Agent", Invest Radiol. 2004; 39:498–505

6

Time Continuous Tracking and Segmentation of Cardiovascular Magnetic Resonance Images Using Multidimensional Dynamic Programming

In modesty and humility be like earth

This chapter was adapted from:
Time Continuous Tracking and Segmentation of Cardiovascular Magnetic Resonance Images using Multidimensional Dynamic Programming
M. Üzümcü, R.J. van der Geest, C. Swingen, J.H.C. Reiber, B.P.F. Lelieveldt
Investigative Radiology, 41(1): 52 – 62, 2006

Abstract

In this chapter, we propose a semi-automatic method for time-continuous contour detection in all phases of the cardiac cycle in magnetic resonance sequences. The method is based on multidimensional dynamic programming. After shape parameterization, cost hypercubes are filled with image-feature derived cost function values. Using multidimensional dynamic programming, an optimal path is sought through the sequence of hypercubes. Constraints can be imposed by setting limits to the parameter changes between subsequent hypercubes. Quantitative evaluation was performed on 20 subjects. Average border positioning error all slices, all phases and all studies, was 1.77 $\pm$ 0.57 mm for epicardial and 1.86 $\pm$ 0.59 mm for endocardial contours. The average error in end-diastolic and end systolic volumes over all studies was small: 4.24 $\pm$ 4.62 mL and -4.36 $\pm$ 3.01 mL, respectively. The average error in ejection fraction was 4.82 $\pm$ 3.01%. The reported results compare favorable to the best-reported results in recent literature, underlining the potential of this method for application in daily clinical practice

6.1 Introduction

For quantitative analysis of cardiac function, clinical parameters such as end-diastolic (ED) and end-systolic (ES) volume, Ejection Fraction (EF) and ventricular wall motion are relevant. These parameters are usually estimated from short axis acquisitions consisting of 200 to 300 images. To quantitatively analyze global and regional cardiac function, endo- and epicardial contours of the cardiac left ventricle are required. Recently, several (semi-) automatic methods were developed for detecting the contours of the myocardium. Van Assen *et al.* [1] and Lötjönen *et al.* [2] have proposed 3-dimensional (3-D) Active Shape Models for automatic segmentation of the human cardiac left ventricle. Kaus *et al.* [3] have developed deformable models constrained by prior knowledge for automatic segmentation of the left ventricle. Sanchez-Ortiz *et al.* [4] propose a multi-scale fuzzy clustering based segmentation algorithm for contour detection in 3-D cardiac echocardiographic images. However, many of the proposed methods are suitable for segmentation in end-diastolic and end-systolic phases only, e.g. [5, 6, 7]. Lorenzo-Valdés *et al.* [8] have developed a 4-D probabilistic atlas for the 4-D (3-D+time) segmentation of the left ventricle based on an expectation maximization method. This method yields segmentations over the full cardiac cycle. However, many manually segmented images are needed for building the atlas and the structures are segmented independently in each time frame. Bosch et al. [9] and Van der Geest *et al.* [10] have demonstrated that active appearance motion models are able to yield time continuous segmentation results for 2-D echocardiographic and cardiac MR image sequences respectively. This method however, needs to be trained on a training set consisting of several cardiac MR scans with manually annotated contours in all slices and all frames.

For a complete overview of recent developments in cardiac segmentation techniques, see the study by Frangi *et al.* [11]
The mentioned methods here either do not yield time continuous segmentation results over the full cardiac cycle, or require extensive manually annotated datasets for training. The goal of this work is to develop a method for time continuous segmentation of the full cardiac cycle that does not require an extensive training set. To accomplish this, we propose an extension of the well-known 2-D dynamic programming to higher dimensions. By expressing a shape with a limited number of parameters, cost hypercubes are constructed, where each axis represents a parameter range. Each node in a hypercube represents a shape instantiation, and a connective path through a sequence of hypercubes represents a changing shape in a time sequence of images. Constraints such as temporal or spatial continuity are imposed by setting limits to the parameter changes for each axis between subsequent hypercubes. This makes the method robust in the presence of artifacts or missing image information in individual frames. By including information from all frames in the segmentation, we expect the method to yield more robust and consistent contours in ED and ES frames, which are generally used for deriving the parameters that are needed for quantitative analysis of the cardiac left ventricle. Furthermore, other clinically relevant time dependent parameters can be derived from the segmented full cycle, such as regional wall motion, rate of wall thickening and peak ejection/filling rate. The proposed method does not require training on large datasets and prior knowledge on global shape or position dynamics is not needed.

6.2 Materials and Methods

6.2.1 Background

Dynamic Programming (DP) [12] is a method for solving variational problems by successively selecting the locally optimal solutions. The Dijkstra algorithm [13] is one of the best known dynamic programming algorithms and is used for solving shortest path problems, i.e. finding the optimal path from one node to another node in a weighted and directed graph. Each node has an associated weight or cost and the optimal path is the path for which the sum of the costs is minimal. An example is shown in Fig. 6.1.
Dynamic programming has been used widely in medical image segmentation, but mainly to enforce spatial continuity. For instance, DP has been widely applied in X-ray left ventricular angiography and coronary angiography [14]. Xu *et al.* [15] have used DP for automated lung nodule segmentation in Computed Tomography images. Optimal 2-D contours are extracted from all slices using dynamic programming with shape-based constraints. These 2-D contours are stacked to obtain 3-D surfaces of the nodules. Yamada *et al.* [16] have presented a 2-D dynamic programming based matching method for kidney glomerulus recognition. In this approach, a parameterization of the shape of the glomerulus is made and constraints on the

9	5	0	9	12	8
8	7	9	2	4	4
5	2	5	8	2	2
7	8	4	3	7	5
3	5	8	6	3	3
8	3	2	6	3	8
9	6	8	7	6	4

9	5	0	9	12	8
13	7	9	2	12	12
12	9	7	10	4	14
16	15	11	7	11	9
18	16	15	13	10	12
24	18	15	16	13	18
27	21	23	20	19	17

Figure 6.1: Example of dynamic programming. In the cost matrix on the left, each element represents a node with a given cost, which is derived from an image-related cost function. Using back-propagation, an optimal path is sought from the bottom row to the top row. In the matrix on the right side, the minimal cumulative costs are shown and the optimal path (elements in gray) connects minimal cumulative costs per row, resulting in a globally optimal path.

range of parameters are imposed using dynamic programming. Amini *et al.* [17] and Geiger *et al.* [18] have used dynamic programming to find globally optimal solutions to variational problems in energy minimization and to allow direct and natural enforcement of constraints on deformable models.

The approaches described here were all used in static images and typically search for a one-dimensional path through a 2-D graph. Little work has been described toward extending DP to higher dimensions. Sonka *et al.* [19] have proposed an extension of 2-D dynamic programming by constructing a cost cube from two perpendicular edge images, one for each coronary edge. In this graph, each node corresponds to a combination of possible positions of the left and right coronary borders simultaneously. The optimal path through this graph results in a segmentation, where shape changes in both coronary edges are coupled.

Thedens *et al.* [20] have developed a graph searching method for finding the optimal surface through a 3-D cost cube. Their approach is based on a data transformation of a 3-D lattice into an intermediate 2-D graph enabling application of traditional graph searching techniques. To make this approach computationally feasible, they introduce a heuristic search approach potentially yielding sub-optimal solutions. Li *et al.* [21] propose a computationally feasible solution for finding a surface through a 3-D graph lattice by computing a minimum *s-t* cut through a 3-D directed graph.

6.2.2 Multi-dimensional parametric dynamic programming

As mentioned before, higher dimensional extensions of dynamic programming have been described for finding either a surface through a 3-D volume, or finding a path

through a 3-D volume. In this work, we extend the classic dynamic programming method to higher dimensions, similar to Sonka's approach [19]. An overview of the general method is represented in Fig. 6.2, whereas details on the concrete implementation of two tracking problems are described in the next section. Instead of applying dynamic programming directly to image data, we first define a parametric shape model, expressing the shape with N parameters. An N-dimensional space can be constructed, where the axes are spanned by the N parameters. A given shape, is represented by a point in this parameter space. Thus, a given combination of the N parameters represents a shape instantiation. By discretizing each parameter axis in a limited parameter range, an N-dimensional hypercube is constructed which is the N-dimensional equivalent of a cost matrix such as shown in Fig. 6.1. For each frame in a time sequence of images, such a cost hypercube is calculated.

For all possible combinations of the model parameters, i.e. all voxels in the hypercubes, cost values are calculated using a cost function based on image features that expresses the "goodness of fit" of the model instantiation to the image data. This can be for instance the cumulative image gradient along a contour or cross correlation values between two regions of interest: the choice of the most suitable cost function depends on the application and the selected parameterization. Constraints on temporal or spatial continuity are imposed by setting limits to the allowed parameter changes between subsequent hypercubes for each axis. Subsequently, the optimal path is sought using dynamic programming by connecting the nodes with minimal cost from all hypercubes with each other within these connectivity constraints. This path is a curve in N-dimensional space. The nodes with minimal cost from cost cubes corresponding to different time frames are connected, where a connective path through a sequence of hypercubes represents a changing shape in a time sequence (see Fig. 6.2). This way, depending on the type of parameterization, spatial and/or temporal continuity can be enforced to ensure smooth motion between frames.

The concrete implementation of the shape parameterization depends on the intended application. In the next section, two types of applications with corresponding parameterizations are elaborated.

6.3 Validation Studies

To investigate the performance and accuracy of the proposed method, two studies were conducted. The first experiment was performed to investigate the accuracy of the DP method in segmentation of short-axis MR images of the cardiac left ventricle and the effect of imposing time continuity constraints on the robustness of the segmentation results. The second experiment involves a case study to demonstrate the method's efficacy in a higher dimensional case: tracking of the aorta in full cycle MR images using a 6-dimensional parametric representation.

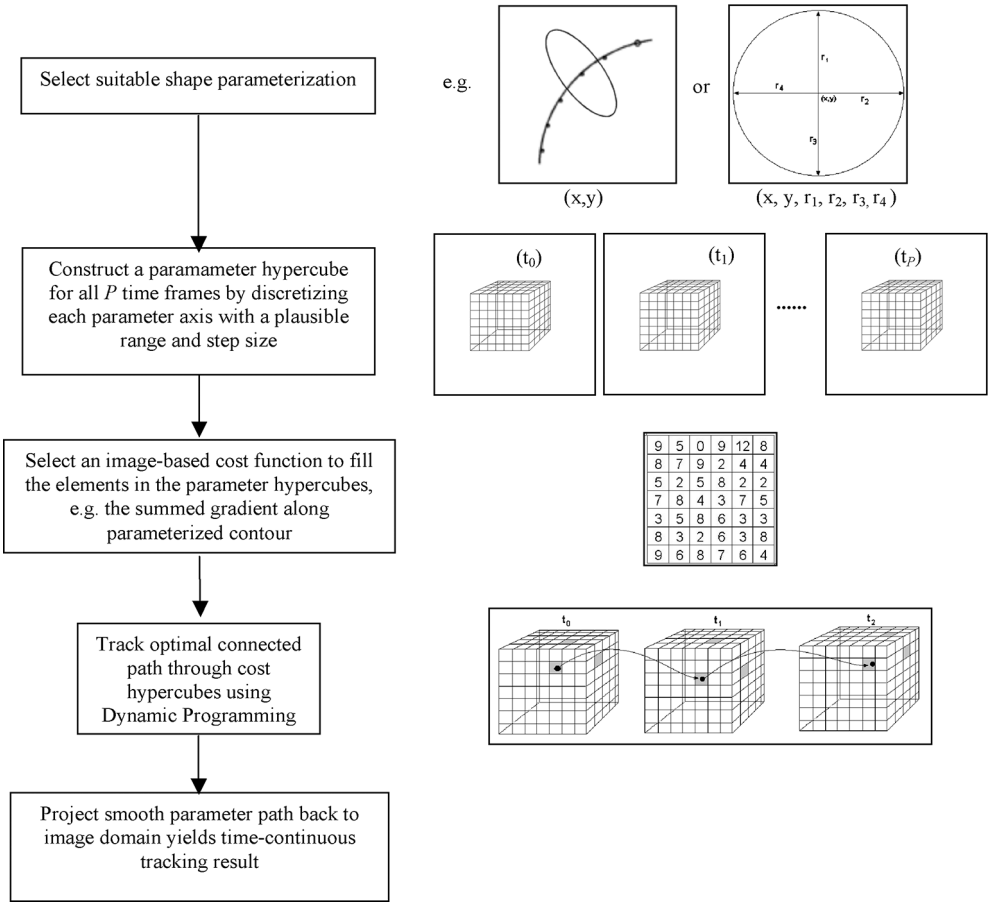

Figure 6.2: General outline of the N-dimensional dynamic programming.

6.3.1 Data material

Cardiac MRI examinations were performed in 18 cardiac patients and 2 healthy volunteers. The patients suffered from several pathologies including heart failure (n = 8), hypertrophic cardiomyopathy (n = 4), transplant follow-up (n = 3), chest pain or angina (n = 3).

Short-axis images of the cardiac left ventricle were scanned using the TrueFISP protocol on a 1.5-T Siemens MR system (Sonata, Siemens Medical Systems, Erlangen, Germany) with a resolution of 256^2 pixels and a field of view ranging from 340 to 420 mm, which resulted in a pixel size varying between 1.33 and 1.64 mm. The inter-slice gap was 2 mm, the slice thickness was 8 mm and the following acquisition parameters were used: TR = 3.1 ms, TE = 1.6 ms, flip angle = 55° and receiver bandwidth = 930 Hz/pixel. In these images, epi- and endocardial contours were drawn by experts in all slices and all phases following the conventions put forward in [23].

To investigate the applicability of the method to higher dimensional tracking problems, an additional velocity encoded aorta flow scan was acquired in a patient with congenital cardiac abnormalities. Images were acquired in an image plane perpendicular to the ascending aorta on a Philips Gyroscan 1.5 T MR system using a phase contrast sequence with a VENC of 3 m/s, field of view 300×253 mm, scan matrix 128×108 reconstructed to 256×256 pixels, pixel size 1.17×1.17 mm (reconstructed) and a slice thickness of 8 mm. The full cardiac cycle was imaged in 30 phases, with TR 14 ms, TE 5.2 ms, flip angle 20° with 2 signal averages.

6.3.2 Short-Axis Cardiac MR Segmentation

An elaborate quantitative evaluation was performed in a study on full-cycle contour detection in short-axis cardiac MR images. During the cardiac cycle, the endo- and epicardial borders undergo small deformations from frame to frame; this makes the proposed dynamic programming very suitable for imposing constraints on the maximally allowed deformations between frames of the border positions, possibly yielding better segmentation results.
Using the proposed dynamic programming approach, the optimal contour set for the cardiac cycle can be found as follows (see the flow chart in Fig. 6.3 for an overview). After initializing manually by drawing a contour in one phase, the contour is resampled to 32 equi-angularly sampled landmarks. Each landmark is parameterized by its coordinates *(x,y)* (Because the papillary muscles were not included in the manual drawing conform clinical standards, 32 landmarks provided sufficient detail to accurately describe the approximately circular contour shapes.). Each landmark is tracked separately over time by defining a mask in each landmark, and a search space around each landmark by setting limits to the displacement parameters dx and dy, which are the allowed shifts for the center of the mask in x and y directions. The mask is positioned onto all allowed positions in the defined search space and a cross-correlation coefficient is calculated for each position with the mask in the reference frame.
Subsequently, for each landmark, the cost hypercubes are filled with the cost values associated with all shifts of the center of the mask. A 3-D search space is created by combining these cost matrices, obtaining a 3-D graph. The first and last frames of the graph are the matrices corresponding to the frame with the manually annotated landmarks, i.e. the initialization frame. For the cost matrix corresponding to the landmarks in the initialization frame the center value is set to zero and all other values are set to high values, as to leave this landmark position unchanged. To find the optimal solution, a connective path is sought through the 3-D graph, starting at the zero element in the first slice and crossing each layer of the graph in only one point.

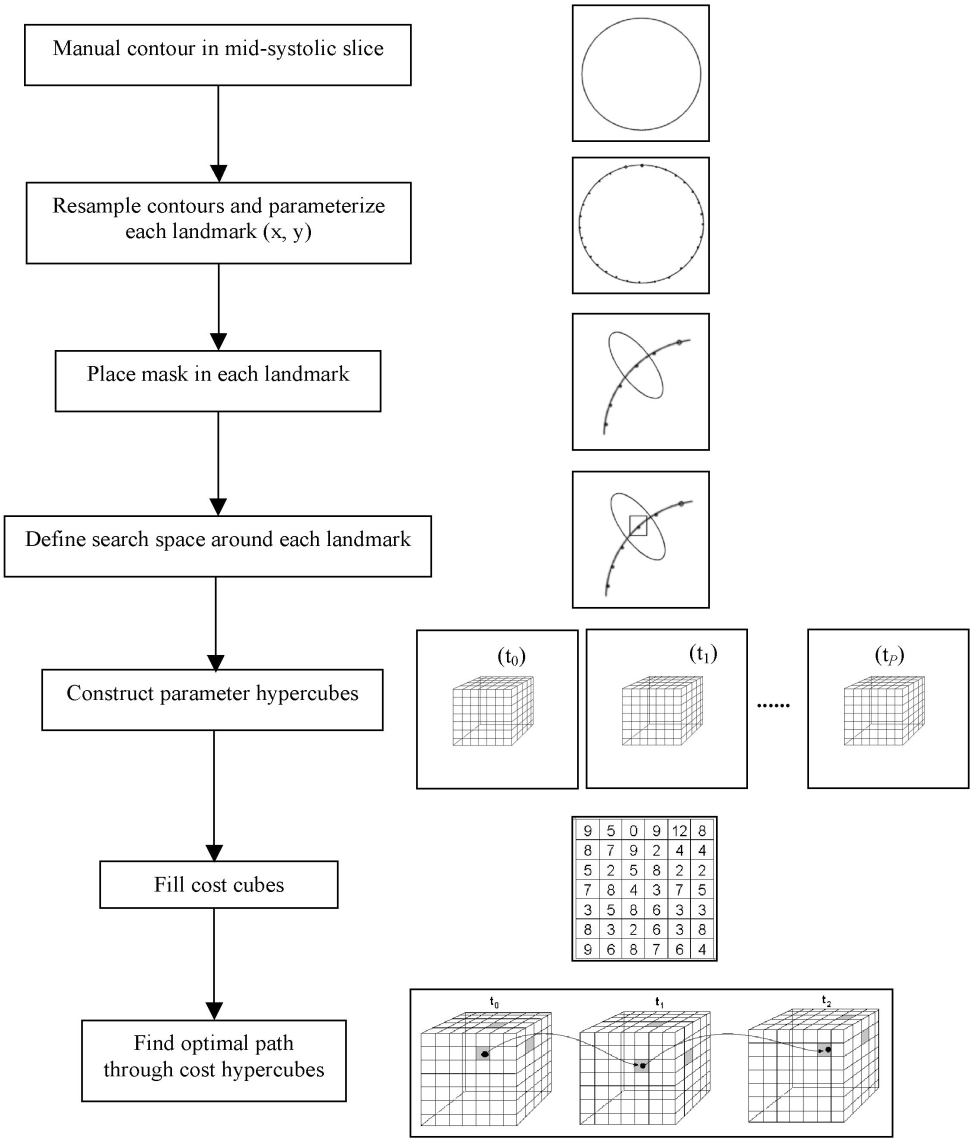

Figure 6.3: Overview of cardiac left ventricle segmentation using multidimensional dynamic programming.

Each path through the graph is a possible solution. The total cost of a path is the sum of the costs of all the nodes constituting the path. The optimal solution is the path with minimal total cost. This optimal path yields translation vectors for each landmark with respect to the manually annotated landmark in the reference frame, thus giving the optimal positions for all landmarks over the full cycle.
While searching the optimal path through the graph, hard constraints can be imposed, e.g. a continuity constraint allowing a maximum side step. Because the sampling rate of the full cycle images is sufficiently high, the inter-frame movement of the borders does not exceed two pixels. Therefore, a maximal side step of two pixels was allowed to obtain time continuity between frames. To assess the effect of the constraints on the side-step parameter, experiments were repeated without side-step constraints. Initialization was performed manually in a mid-systolic phase to enable automatic detection of both end-diastolic and end-systolic frames. This way an automatic calculation of ejection fraction was possible without introducing a bias towards either the ED or ES frame. In all slices between apex and base, endo- and epicardial contours were available for the initialization frame.

Parameter Selection

Several parameters influence the performance of the method and a brute-force search was performed to systematically select a parameter combination yielding good segmentation results. The parameters involved in the brute force search were:

- *Type of cost function*: two types of cost functions were considered. First, cross-correlation of the mask in the current frame with the mask in the reference frame was considered. The cross-correlation coefficients were considered as costs, i.e. the higher the correlations, the lower the cost. Second, the sum of absolute gray value differences between the masks was used. Here, a smaller difference corresponds to a lower cost value.
- *Mask size*: The mask size and shape define the region of interest around each landmark and the amount of information involved in the calculation of the costs. The mask must contain sufficient structure for the cost values to be accurate. However, a too large mask may include papillary muscles or other structures, which are not present in every frame, potentially resulting in wrong landmark positions in some frames. In the detection of endocardial contours, mask clipping was applied. Because in apical slices the endocardial contours may become very small, the mask size is adapted to half of the radius of the endocardial contour in the initialization frame.
- *Mask shape*: The shape of the mask is varied from an ellipse tangent to the contour to a circular shape to an ellipse perpendicular to the contour by changing the parameter value between $-\frac{1}{2}$, 0 and $+\frac{1}{2}$ (see Fig. 6.4).

- *Physical dimensions of the search space*: The parameter limits of the search space were defined by the maximally allowed displacements in x- and y-directions. The size of the search space should be large enough to follow the movement of the myocardium between end-diastolic and end-systolic phases.

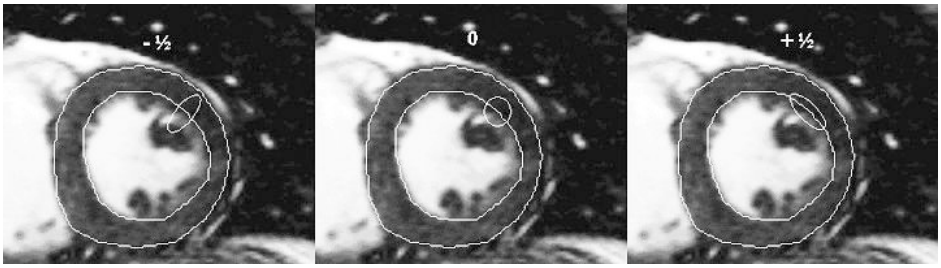

Figure 6.4: Possible settings for the shape of the mask: ellipsoid perpendicular to contour($-\frac{1}{2}$), circular mask (0) and ellipsoid tangent to contour ($+\frac{1}{2}$).

The first parameter involves the selection of cost function, and is the only intensity feature dependent choice. The other parameters describe geometric and kinematic properties of the contracting heart. Therefore, we expect the parameter selection to be largely independent of the scanning protocol, therefore generalizing well towards other cardiac MR acquisition protocols not tested here.

Evaluation Indices

To quantify the matching accuracy of the model, the automatically detected contours were compared with the manually defined expert contours on the basis of the point-to-curve border positioning errors, the ED and ES volumes and the EF. The point-to-curve errors were defined as the shortest distance between an automatically detected landmark and the manually drawn contour, i.e. the distance along the normal to the manually drawn curve. Average and maximum border positioning errors were measured. The ED and ES volumes were calculated as follows. In each slice the surface of the endocardial border, i.e. the blood pool, was calculated and multiplied with the slice thickness. The sum of all slice volumes was calculated to determine the 3-D volume of the cardiac left ventricle. Using the volumes in ED and ES phases of the cardiac cycle, the ejection fraction (EF) was calculated as follows:

$$EF = \frac{V_{ED} - V_{ES}}{V_{ED}} \tag{6.1}$$

where EF is the ejection fraction, V_{ED} the cardiac left ventricular volume in end-diastolic phase and V_{ES} the volume in end-systolic phase. Paired sample T-tests were performed to determine if the errors in border positioning, volumes and ejection fractions were significant. P-values smaller than 0.05 were considered significant.

6.3.3 Aorta Tracking

An additional experiment was performed to investigate the potential of multi-dimensional dynamic programming applied to higher dimensional cases. The area of the aorta was tracked over time to measure the flow [22] in images of a specific slice of the aorta, which are used to measure flow volume. In a time sequence of images, translation and deformation of the aorta occurs.

To this end, the shape of the aorta was parameterized with six parameters (center coordinates [x,y] and four radii r_1 - r_4) as shown in Fig. 6.5. In sequential images, the center coordinates were varied as well as the four radii. A spline was fitted to the endpoints of the radii to obtain an ellipse. With this parameterization a 6-dimensional cost hypercube was constructed. The costs associated with each instantiation of the aorta shape was defined as the cumulative image gradient along the model contour. Ranges were defined for all combinations of the above-mentioned parameters, i.e. all shape instantiations. The associated costs were calculated and stored in the corresponding positions in the hypercube. Next, using conventional backtracking, an optimal path with minimal total cost within time-continuity constraints was sought through the hypercubes.

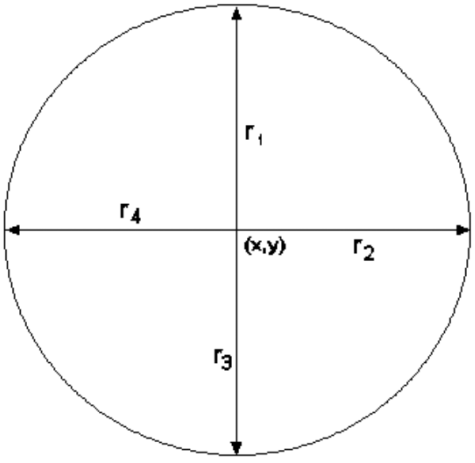

Figure 6.5: Six-dimensional parameterization of a region around the aorta with center coordinates *(x,y)* and 4 radii r_1, r_2, r_3, r_4.

The optimal path yielded translation vectors for the center coordinates and deformation vectors for the radii with respect to the reference frame. The results of the experiments were evaluated visually.

6.4 Results

6.4.1 Parameter Settings

The parameters computed in the parameter selection process are given in Table 6.1. For detection of both endocardial and epicardial contours the cross-correlation based cost function was found to give more accurate results than the cost function based on the sum of absolute differences.

Table 6.1: Optimal settings for parameters obtained with a brute-force search. Mask shape 0 corresponds to a circular mask (see Fig. 6.3) and $-1/2$ corresponds to ellipsoid. Results for endocardial and epicardial contours are shown.

Contour	Dx (pixels)	Dy (pixels)	Mask Size (pixels)	Mask Shape
Epicardial	4	4	15	0
Endocardial	7	7	19	$-1/2$

6.4.2 Segmentation Results

Epicardial and endocardial contours were detected separately. With parameter settings as shown in Table 6.1, the average border positioning error (BPE) over all slices, all phases and all studies was 1.77 ± 0.57 mm (average maximum BPE was 5.21 mm) for epicardial contours and 1.86 ± 0.59 mm (average maximum BPE was 4.51 mm) for endocardial contours. In Table 6.2, the errors in volumes and ejection fractions are shown. From the fitted functions (Table 6.3) can be seen that for the ED and ES volumes there is a very good correlation between the volumes calculated from manually drawn and automatically detected contours. Figure 6.7 shows Bland-Altman plots for ED and ES volumes and ejection fractions.

Table 6.2: Average manual ED and ES volumes and ejection fractions, with average errors made by an automatic dynamic programming based method

	Average manual	Average Error	P-value
ED volume (mL)	171.68 ± 91.10	4.24 ± 4.62	6.14E-4
ES volume (mL)	103.96 ± 95.64	-4.36 ± 4.26	2.05E-4
Ejection Fraction (%)	47.73 ± 19.20	4.82 ± 3.01	8.48E-7

Figure 6.8 shows that if no time continuity constraints are imposed, the segmentations deteriorate and large inter-frame discontinuities and border positioning errors are introduced. As can be seen from the bottom row of Fig. 6.8, single landmarks can make large excursions and lock onto false positions, resulting in bad segmentation results.

Table 6.3: Equations of regression fits for ED and ES volumes and ejection fractions

	Regression Fit	R^2
ED volumes	$y = 0.99x - 2.21$	0.998
ES volumes	$y = 0.98x + 6.55$	0.998
Ejection Fractions	$y = 0.89x + 0.34$	0.984

Typical computation times for full-cycle segmentation of a 3-D short-axis cardiac MR scan (8-12 slices, 20-25 frames) amounted to 4 minutes on a desktop PC with an AMD Athlon 1.8 GHz processor.

6.4.3 Tracking Results

Figure 6.6 shows the result of tracking the aorta in 30 sequential time frames using a shape parameterization with 4 radii and 2 center coordinates.

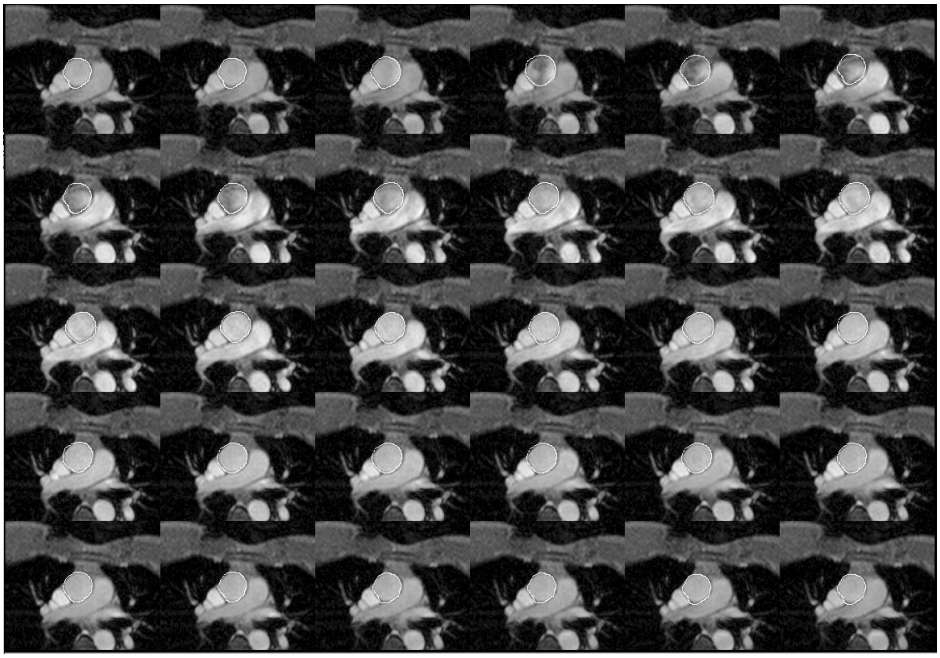

Figure 6.6: Sequential timeframes in an aortic flow scan, in which the motion and deformation of the aorta is tracked over the cardiac cycle. Note the smooth transitions between frames, which is a result of the imposed time continuity.

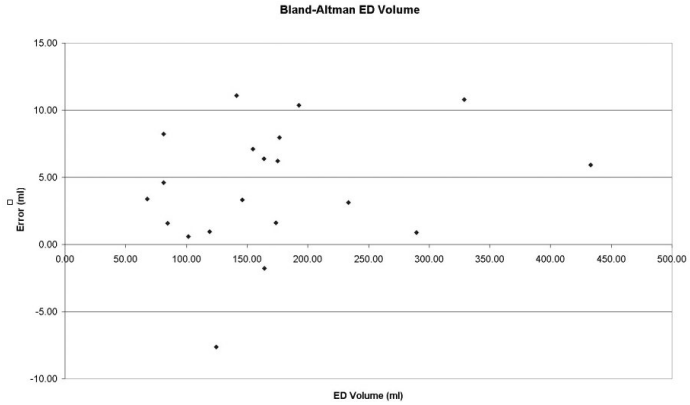

(a)

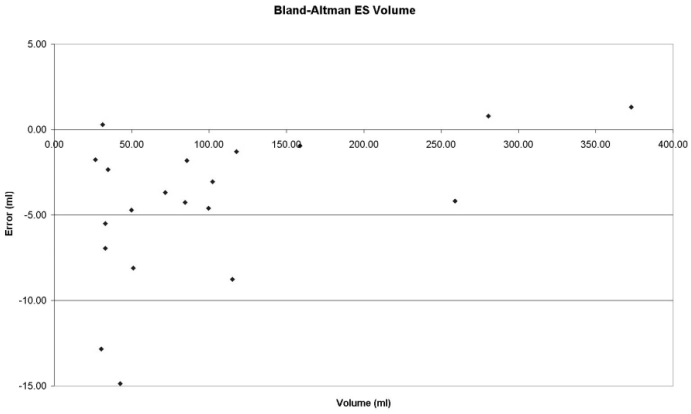

(b)

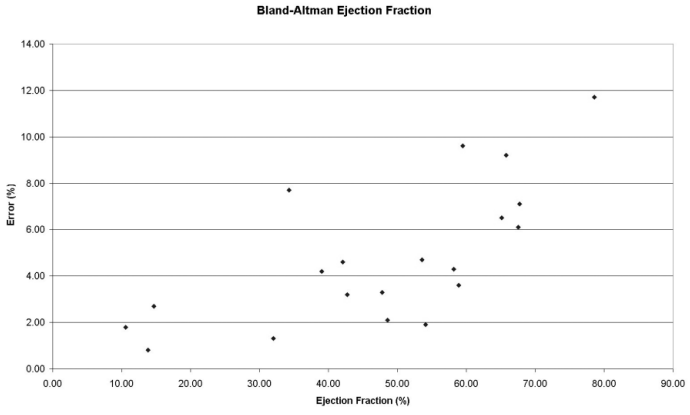

(c)

Figure 6.7: Bland-Altman plots for end-diastolic volumes (a), end-systolic volumes (b) and ejection fractions (c). The errors are the differences between manually annotated data and automatically detected contours (manual - auto).

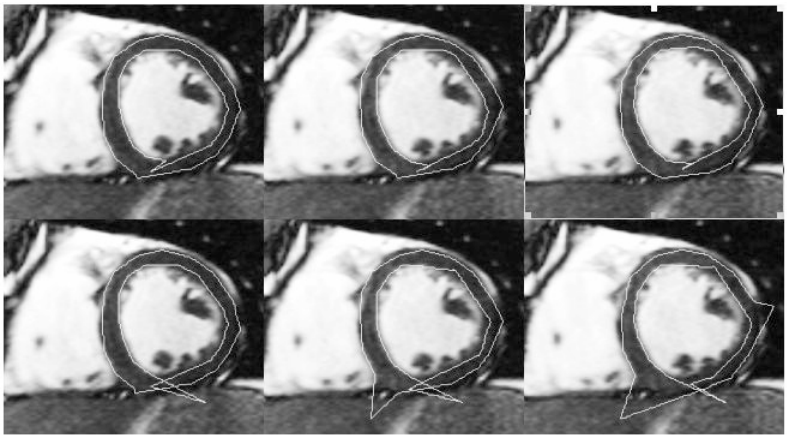

Figure 6.8: The top row shows segmentation results obtained with time-continuity constraint in 3 successive frames. In the bottom row, the same frames segmented without imposing time-continuity are shown.

6.5 Discussion & Conclusions

A dynamic programming based method for time continuous segmentation of endo- and epicardial contours was presented. Conventional 2-D dynamic programming was extended to higher dimensions and applied to two substantially different tracking and segmentation problems to illustrate the method's performance in multiple dimensions.

In the quantitative evaluation, segmentations were performed in 20 studies in all phases and all slices. Contour detection was successful in all included imaging slices and the average border positioning error (BPE) was very good (1.86 mm and 1.77 mm for endo- and epicardial BPE, which corresponds to ± 1 pixel), although slightly less accurate as inter-observer BPE reported in [1]: (1.27 mm and 1.14 mm for endo- and epicardial BPE respectivly). Lötjönen *et al.* [2] report an average segmentation error of 2.57 mm using the probabilistic atlas based method. The method presented by Kaus *et al.* [3] has a mean deviation from manual segmentations of 2.45 mm in end-diastolic phase and 2.84 mm in end-systolic phase, whereas Van Assen *et al.* [1] report 2.24 mm and 2.84 mm errors for endo- and epicardium respectively. Lorenzo-Valdés *et al.* [8] report an average segmentation error of 2.21 mm for the three middle slices of the left ventricle over all time frames. Also the maximum BPE for endo- and epicardial contours (4.51 mm and 5.21 mm respectively) compares highly favorable to the other automated methods (11-15 pixels as reported in [1, 3]), and compares well to inter-observer maximum errors in [1] (4.34 and 3.93 maximum BPE for endo- and epicard respectively). Therefore, we can conclude that border positioning errors presented in this paper compare favorable to these other results reported in recent

literature, and approach inter-observer variabilities due to manual contour drawing. Of these methods, only Lorenzo-Valdés reports full cycle contour detection. The other approaches report results in ED and ES phases only. An important criterion for any automated border detection method for cardiac MR images, is that if morphology is important, accurate regional measurements require the border detection to yield errors at least as good as the inter-observer variability due to manual contour drawing, because a small error can already have a significant impact on regional measurements such as wall thickness and wall thickening. Of the algorithms compared here, the proposed method best approaches this inter-observer BPE.

The automatically determined end-diastolic and end-systolic volumes showed near-perfect correlations with the volumes derived from manual contours. Also, the ejection fractions of automatically segmented and manually drawn studies correlated very well. This is a direct consequence of the small border positioning errors, but although the volume errors are small, they are statistically significant (P-values $<$ 0.05). Bland-Altman plots reveal a slight systematic underestimation of the ED volumes and a slight systematic overestimation of the ES volumes. This, of course, has a negative influence on the ejection fraction estimates. The systematic over- and underestimations are most probably caused by a bias towards the reference frame. Currently, a rectangular search space around the landmarks is used (dx=dy). Defining a different search space shape, e.g. allowing more radial movement, might resolve the systematic bias. The errors, however, are small and not clinically relevant: they are in the same range as inter-observer variations in ventricular volumes and ejection fractions [23], comparing measurements from manually drawn contours from different observers

As can be seen in Table 6.1, a larger search space and mask need to be defined for endocardial contour detection than for epicardial contour detection. Also the border positioning errors are slightly larger for endocardial contours. This is caused by the fact that during the cardiac cycle the movement of the endocardial border has larger amplitude than the epicardial border. Therefore, the texture in the masks used for tracking the endocardial borders demonstrates relatively more changes between end-diastolic and end-systolic phases. Also the fusion of the papillary muscles with the myocardium in end-systolic phases substantially changes the mask texture. These effects deteriorate the cross correlation values, i.e. the cost function outcomes.

The proposed method may possibly be further improved, e.g. by blurring the images before contour detection. Blurring the images reduces noise and better cross correlation values can be obtained. Another improvement might be smoothing of the contours after detection. Currently, all landmarks are detected independently and are connected with each other by straight lines. This in general gives a slight underestimation of the volumes. The underestimation is larger in basal slices and also in end-diastolic images, because the sampling of the contours is less dense in these images. Smoothing the contours after connecting the landmarks might give a better estimate of the volumes, although landmark positions remain unchanged.

Experiments have shown that adding a time constraint to the conventional dynamic

programming approach substantially improved the segmentation results. Without this constraint, single landmarks showed large inter-frame displacements, which led to locking on false edges. Imposing a maximal inter-frame displacement by means of a time constraint, resolved these errors.
In the current approach, endo- and epicardial contours are detected separately. However, the locations of both contours are strongly correlated. Therefore, combining both contours and detecting them simultaneously might yield still more robust results.
For each landmark separate cost matrices are calculated for each time frame and the optimal positions of the landmarks are determined independently from its neighboring landmarks. In some cases this leads to crossing landmarks and spatial discontinuities in the segmentations (see Fig. 6.9).

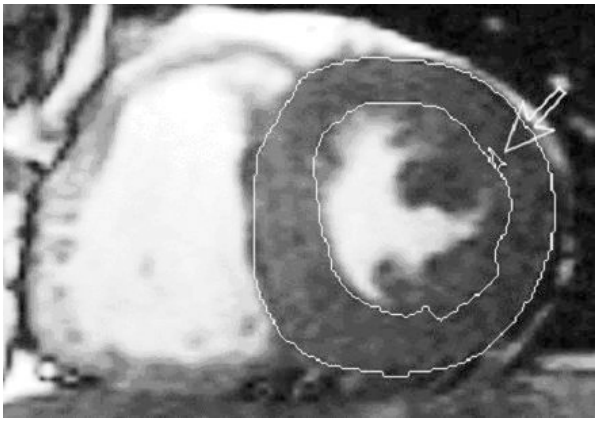

Figure 6.9: Spatial discontinuity caused by crossing landmarks in endo-cardial contour.

These artifacts may be resolved by following the approach in [20] and coupling neighboring landmarks, preventing landmarks from crossing each other. This way, not only time-continuous, but also spatially continuous segmentations can be obtained, which may also lead to a further improvement of the border positioning errors, the volume estimations and ejection fraction calculations.
In our current approach, segmentations were performed on a slice-per-slice basis. Time continuous segmentation results can be obtained for each slice in this manner. However, inter-slice continuity is not guaranteed. By coupling landmarks from neighboring slices with the proposed approach, inter-slice continuity may be obtained as well.
The parameter selection procedure involved systematically deriving a good parameter combination, where most of the parameters were related to geometry and cardiac kinematics, which are independent of the applied scanning protocol. Highest accuracy was obtained with the presented values for the parameters in the tested image sets. However, we expect similar performance in other MR datasets and protocols due to the protocol independence of the tuned parameters.

The aorta tracking experiments have demonstrated the power of the proposed method in a 6-dimensional case study. The proposed approach was used for automatic tracking of the aorta in a time sequence of images and visual inspection showed that a time continuous result was obtained. This example showed that there are no theoretical obstacles for the expansion of the proposed method to high dimensions; however, further evaluation is required to quantitate the performance of dynamic programming in such higher dimensional cases.
The main limitation of the proposed method is its computational complexity, which increases exponentially with the number of parameter dimensions. Finding the optimal path through cost hypercubes is fast; however filling the cost hypercubes may become time consuming. This obviously depends on the dimension of the hypercubes and the type of cost function, e.g. sum of absolute differences, cross-correlation values, etc. In the experiments that were performed, typical computing times in the order of 3-5 minutes per study (on average 20 phases and 10 slices) were found. As the analysis is performed offline and with increasing computer power, this does not impose a major limitation on clinical applicability. In addition, by pruning the search space, substantial additional performance gains can be achieved.
In conclusion, the proposed method has shown great utility in tracking and segmentation of cardiac MR time sequences. The Multi-dimensional Dynamic Programming allows for direct and natural enforcement of constraints, e.g. shape-based constraints or time-continuity constraints. It is not iterative and therefore it is exact and stable. With dynamic programming global optimality of the solution is ensured and multi-dimensional dynamic programming enables detection of time evolution and full cycle time continuous segmentation in a series of images. The reported results compare favorable to the best-reported results in recent literature, underlining the potential of this method for application in daily clinical practice.

References

[1] H.C. van Assen, M.G. Danilouchkine, A.F. Frangi, S. Ordas, J.J.M. Westenberg, J.H.C. Reiber, B.P.F. Lelieveldt, "SPASM: Segmentation of Sparse and Arbitrarily Oriented Cardiac MRI data using a 3D ASM", proc FIMH 2005, Lecture Notes in Computer Science, 3504: 33–43

[2] Lötjönen J, Kivistö S, Koikkalainen J, *et al.* "Statistical shape model of atria, ventricles and epicardium from short- and long-axis MR images", Medical Image Analysis. 2004; 8(3): 371–386

[3] Kaus MR, Von Berg J, Weese J, *et al.* "Automated segmentation of the left ventricle in cardiac MRI", Medical Image Analysis. 2004; 8(3): 245–254

[4] Sanchez-Ortiz GI, Wright GJT, Clarke N, *et al.* "Automated 3-D Echocardiography Analysis Compared With Manual Delineations and SPECT MUGA", IEEE Transactions on Medical Imaging. 2002; 21(9): 1069–1074

[5] Stegmann MB and Pedersen D. "Bi-temporal 3D active appearance models with applications to unsupervised ejection fraction estimation", In Proc. SPIE Vol. 5747, Medical Imaging 2005: Image Processing, Milan Sonka and J. Michael Fitzpatrick (Eds.)

[6] Mitchell SC, Bosch JG, Lelieveldt BPF, *et al.* "3-D Active Appearance Models: Segmentation of Cardiac MR and Ultrasound Images", IEEE Transactions on Medical Imaging. 2002; 21(9): 1167–1177

[7] Üzümcü M, Van der Geest RJ, Sonka M, *et al.* "Multi-View Active Appearance Models for Simultaneous Segmentation of Cardiac 2- and 4-chamber Long Axis MR Images", Investigative Radiology. 2005; 40(4): 195–203

[8] Lorenzo-Valdés M, Sanchez-Ortiz GI, Elkington AG, *et al.* "Segmentation of 4D cardiac MR images using a probabilistic atlas and the EM algorithm", Medical Images Analysis. 2004; 8(3): 255–265

[9] Bosch JG, Mitchell SC, Lelieveldt BPF, *et al.* "Automatic Segmentation of Echocardiographic Sequences by Active Appearance Motion Models", IEEE Transactions on Medical Imaging. 2002; 21(11): 1374–1383

[10] Van der Geest RJ, Lelieveldt BPF, Angelie E, *et al.* "Evaluation of a new method for automated detection of left ventricular contours in time series of Magnetic Resonance Images using an Active Appearance Motion Model", Journal of Cardiovascular Magnetic Resonance. 2004; 6(3): 609–617

[11] Frangi AF, Niessen WJ, Viergever MA. "Three-dimensional modeling for functional analysis of cardiac images, a review", IEEE Transactions on Medical Imaging. 2001; 20(1): 2–25

[12] Bellman R and Dreyfus S, Applied Dynamic Programming, Princeton University Press, Princeton, NJ, U.S.A.; 1962

[13] Dijkstra EW. "A note on two problems in connexion with graphs", Numerische Matematik 1, 1959; 269–271

[14] Sonka M and Fitzpatrick JM (Eds.), Handbook of Medical Imaging, Vol.2: Medical Image Processing and Analysis, SPIE Press, Bellingham, Washington, U.S.A., 2000; 711–794

[15] Xu N, Ahuja N and Bansal R. "Automated Lung Nodule Segmentation Using Dynamic Programming and EM Based Classification", In Proc. SPIE Vol. 4684, Medical Imaging 2002: Image Processing, Milan Sonka and J. Michael Fitzpatrick (Eds.), 2002; 666–676

[16] Yamada H, Merritt C and Kasvand T. "Recognition of Kidney Glomerulus by Dynamic Programming Matching Method", IEEE Transactions on Pattern Analysis and Machine Intelligence. 1988; 10(5): 731–737

[17] Amini AA, Weymouth TE and Jain RC. "Using Dynamic Programming for Solving Variational Problems in Vision", IEEE Transactions on Pattern Analysis and Machine Intelligence, 1990; 12(9): 855–867

[18] Geiger D, Gupta A, Costa LA and Vlontzos J. "Dynamic Programming for Detecting, Tracking, and Matching Deformable Contours", IEEE Transactions on Pattern Analysis and Machine Intelligence, 1995; 17(3): 294–302

[19] Sonka M, Winniford MD and Collins SM. "Robust Simultaneous Detection of Coronary Borders in Complex Images", IEEE Transactions on Medical Imaging, 1995; 14(1): 151–161

[20] Thedens DR, Skorton DJ, Fleagle SR. "Methods of Graph Searching for Border Detection in Image Sequences with Applications to Cardiac Magnetic Resonance Imaging", IEEE Transactions on Medical Imaging, 1995; 14(1): 42–55

[21] Li K, Wu X, Chen DZ, Sonka M. "Efficient Optimal Surface Detection: Theory, Implementation and Experimental Validation", In Proc. SPIE Vol. 5370, Medical Imaging 2004: Image Processing, Milan Sonka and J. Michael Fitzpatrick (Eds.); 620–627

[22] Kondo C, Caputo GR, Semelka R, *et al.* "Right and left ventricular stroke volume measurements with velocity-encoded cine MR imaging: in vitro and in vivo validation", AJR, 1991; 157: 9–16

[23] M.G. Danilouchkine, J.J.M. Westenberg, A. de Roos, J.H.C. Reiber, B.P.F. Lelieveldt, "Operator Induced Variability in Cardiovascular MR: Left Ventricular Measurements and their Reproducibility", Journal of Cardiovascular Magnetic Resonance, 2005; Vol 7(2): 447–457

7

Summary and Conclusions

In tolerance be like a sea

7.1 Summary

Cardiovascular diseases are highly prevalent in the western world. With the aging of the population, the number of people suffering from CVD is still increasing. Therefore, the amount of diagnostic assessments and thus, the number of image acquisitions will increase accordingly. Considering the high quantities of data produced by 3D and 4D imaging modalities, such as CT and MRI, manual contouring and diagnosis currently require much time and attention of the radiologists and cardiologists. This justifies the need for (semi-) automatic segmentation methods; developing these was the focus of the research presented in this thesis. In chapter 1 the goals for this thesis were set as follows:

1. Improvement of local segmentation accuracy by exploring other statistical decomposition methods
2. Increasing segmentation robustness by integrating information from different views and time frames
3. Developing a method for time-continuous segmentation over the full cardiac cycle

The following sections are summaries of chapters 2 - 6 and show that the research presented in this thesis has yielded methods that perform equal to or better than existing techniques.

In chapter 2, the use of ICA instead of PCA for describing statistical variations in the dataset in Active Appearance Models was investigated. It was demonstrated that ICA yields localized shape variations, whereas PCA results in global shape variations. However, the vectors given by PCA are ordered, which was not the case with ICA. Furthermore, PCA yields more compact models than ICA. It is inherent to the PCA method to find directions along which the variance is the greatest and, in this sense, PCA is known to be optimal. Consequently, the first few modes explain most of the shape variations, whereas the later modes are less significant. The ICA method however, maximizes the independence between de vectors and therefore each Independent Component describes an almost equal amount of variance.

Three different datasets were used to evaluate the different methods for calculating and sorting the Independent Components. The first set consisted of 51 expert-drawn contours from 2-chamber long-axis MR images, consisting of 64 landmarks each. The second set consisted of 89 expert drawn contours from cardiac left ventricular X-ray angiography images, each consisting of 60 landmarks. The final set consisted of 150 expert drawn contours from cardiac left and right ventricles as seen in short-axis MR images. This way, the ICA method was tested on different shapes and modalities. The different algorithms for performing ICA that were investigated yielded localized shape variations. However, small differences were noted in size and location of the shape variations between the algorithms. The JADE method for calculating the Independent Components was selected for further implementation in the AAM framework as this method was not initialized randomly and yielded

robust and reproducible results. In addition, several methods for ordering the Independent Components were investigated, as the IC's are not sorted intrinsically. Ordering the IC's according to locality was selected as the best way of sorting, as the results agreed most with what was expected intuitively. Because no golden standard for evaluating the results of the ordering method exists, the results were interpreted visually.

In chapter 3, the accuracy of PCA- and ICA-based AAM segmentations for cardiac short-axis MR images was evaluated. A dataset consisting of 132 routinely acquired short-axis mid-ventricular MR images of the left and right ventricle collected from 44 subjects was used for quantitative evaluation. From this dataset, 44 leave-three-out models were trained. Three images from one patient were left out and a model was trained on the remaining 129 images from 43 patients. The model was then tested on the omitted samples. Both methods showed comparable segmentation accuracy. In case of initialization at the known optimal positions, PCA showed slightly better results and in the case of applying offsets in the initialization, ICA based AAMs showed slightly better results. However, the differences were not statistically significant. A subspace analysis, which was performed to understand the comparable performance of both models, showed that the vectors in the intersection subspace of PCA and ICA describe nearly the same amount of variance as the high-energy PCA modes.

Chapter 4 illustrates the potential of ICA as an analysis tool for extracting local shape deformation. It was demonstrated that the ICA-based infarct detection and localization from short-axis MRI images is a promising technique for computer aided infarct localization. An ICA model was trained on mid-ventricular short-axis MR images from 42 healthy volunteers using the JADE algorithm. Qualitative evaluation was performed on MR images of 6 infarct patients. From these subjects, also delayed-enhancement MR images (DE-MRI) were acquired. Results obtained with the ICA model were compared visually with the DE-MRI acquisitions. In the qualitative comparison for 6 patients, the hypo-kinetic regions showed an excellent correspondence to the hyper-intensity regions of the "gold standard" DE-MRI.

Chapter 5 demonstrates the potential for an automated analysis of global cardiac function from bi-plane long-axis cardiac MR images. Multiview Active Appearance Models were introduced, combining information from different views and time frames to achieve a robust simultaneous segmentation in the 2- and 4-chamber views in end-diastolic and end-systolic phases of the cardiac cycle. Long-axis MR acquisitions from 59 subjects, including patients diagnosed with different pathologies, were used for a leave-one-out validation. Quantitative evaluation of the model performance was realized by comparing the bi-plane area length volumes and ejection fractions of the automatically determined contours and the manually annotated contours. Two types of model initialization were investigated. Initialization in all frames yielded good results in more than 96% of the subjects. The errors between manually annotated and automatically detected contours were not statistically significant. When initializing in the end-systolic frames only, the Multi-View AAM method per-

formed well in more than 92% of the subjects. Though there are more outliers, initializing in the end-systolic frames leads to only a slightly less accurate result; however, this requires half the user interaction. The accuracy of the Multi-View AAM was compared to the variation between multiple observers. With initialization in all frames, the variability of the proposed method is comparable to the interobserver variabilities reported. When initializing in the end-systolic frames only, the error increases slightly due to the fact that the initial position in the end-diastolic phase is further away from the optimal position. This way, however, minimal user interaction is required for initialization. The errors in the bi-plane area length volumes were not significant. For the ejection fractions, the average error and the standard deviation in the errors were relatively small compared to the average manual ejection fraction. The border positioning errors for cardiac long-axis MR images, show excellent correspondence to the accuracy presented in literature. Analysis of cardiac function using present methods is performed off-line. Short-axis acquisitions are still considered as the gold standard for global and regional analysis of cardiac function; however, the method presented in this chapter offers an alternative for rapidly assessing information about global cardiac function, while the patient is still in the scanner. Including all user interaction, global parameters such as EF, stroke volume and cardiac output can be obtained within 20 seconds, enabling online global cardiac function analysis. The proposed method can be generalized towards short-axis MR acquisitions. The combination of both long- and short-axis acquisitions will enable an optimal quantification of both global and regional cardiac function.

In chapter 6 a multi-dimensional dynamic programming based method for semi-automatic time continuous segmentation of endocardial and epicardial contours was presented. Conventional 2D dynamic programming was extended to higher dimensions and applied to two substantially different tracking and segmentation problems to illustrate the methods performance in multiple dimensions. A dataset of 20 studies was available for quantitative analysis of the proposed method for segmentation of the full cardiac cycle. The dataset consisted of short-axis MR images of the left ventricle of 2 healthy volunteers and 18 subjects that were diagnosed with different pathologies. Contours were drawn by experts in all slices and time frames of this dataset. Furthermore, a velocity-encoded aorta flow scan was acquired in one patient with congenital cardiac abnormalities to investigate the applicability of the dynamic programming based method to high dimensional tracking problems. The segmentation was successful in all included image slices and the average border positioning error was very small. The automatically determined end-diastolic and end-systolic volumes showed near-perfect correlations with the volumes derived from manual contours. Also, the ejection fractions of automatically segmented and manually drawn studies correlated very well. The errors between automatically determined and manually calculated volumes and ejection fractions were small and not clinically relevant. Adding a time continuity constraint to the conventional dynamic programming approach substantially improved the segmentation results. Without this constraint, single landmarks showed large inter-frame displacements,

which led to locking on false edges. Imposing a maximal inter-frame displacement by means of a time continuity constraint, resolved these errors. An additional experiment was performed to demonstrate the power of multi-dimensional dynamic programming in a 6-dimensional case study. The proposed approach was used for automatic tracking of the aorta in a time sequence of images and visual inspection showed that a time continuous result was obtained. This example showed that there are no theoretical obstacles for the expansion of the proposed method to high dimensions. The proposed method has shown great utility in tracking and segmentation of cardiac MR time sequences. The Multi-dimensional Dynamic Programming allows for direct and natural enforcement of constraints, e.g. shape-based constraints or time-continuity constraints. It is not iterative and therefore it is exact and stable. With dynamic programming, global optimality of the solution is ensured and multi-dimensional dynamic programming enables detection of time evolution and full cycle time continuous segmentation in a series of images.

7.2 Conclusions and future work

The results presented in this thesis represent a substantial improvement of the automatic segmentation of cardiac MR image sequences. The goals set in the introduction are achieved to a great extend. The use of Independent Component Analysis as an alternative shape decomposition technique did not improve segmentation accuracy, because the information described by the independent components was similar to the variation explained by the largest eigenvectors obtained with Principal Component Analysis. However, the use of ICA did enable automatic infarct detection and localization. In a qualitative comparison, ICA showed great promise for use in Computer Aided Diagnosis, however further research is needed to quantitate these results.

Semi-automatic full cycle time-continuous segmentation of the cardiac left ventricle is achieved by using a multi-dimensional dynamic programming based method. At present, this method needs initialization in one time frame of the cardiac cycle, i.e. contours in all slices in this time frame need to be drawn manually by experts. Fully automatic segmentation of the cardiac cycle could be achieved by combining the Active Appearance Model with the multi-dimensional dynamic programming based method. This way, the latter method can be initialized by performing an AAM based segmentation in one time frame to detect contours in all slices. Thereafter, these contours can be propagated to all other time frames by using the multi-dimensional dynamic programming based approach.

To demonstrate the robustness of the multi-dimensional dynamic programming based method, the parameters used for segmentation were determined over a wide variety of normal subjects and subjects with different pathologies. Similar to training different Active Appearance Models for different groups of subjects, segmentation accuracy could be increased by finding the parameters for this model separately

for each group of subjects. However, the decrease in generality versus the gain in accuracy should be investigated.
Semi-automatic segmentation using the multi-dimensional dynamic programming based method has been applied to the detection of contours of the cardiac left ventricle as seen in MR image sequences. However, no theoretical obstacles exist for applying this method to the right ventricle or cardiac image sequences from other modalities such as CT or ultrasound. Further research in this direction will enable fully automated time-continuous segmentation of the cardiac cycle.
All automated segmentation methods are prone to errors to some extent. With the Active Appearance Models presented in this thesis, these errors can be quantified and reported. In each iteration, the model generates artificial images resembling the image to be segmented. During matching the least squares error between the generated and real images is calculated and used as a measure for the goodness of fit. In case the matching fails, this value exceeds a certain goodness of fit threshold, which can be used as an indicator for a failed segmentation. Slices in which segmentation was unsuccessful can be indicated in the user interface, such that the user can correct these manually. The same method should be investigated in case of segmentation using the multi-dimensional dynamic programming based method. This method is based on the optimization of a (multi-dimensional) cost function. At present the total value of the penalty over all slices and phases is optimized. To enable automatic error detection in this method, the value of the cost function should be evaluated and stored per slice and phase in the cardiac cycle. This way, a correlation between the segmentation result and the value of the cost function per slice and phase could be found. Similar to the AAM, slices in which segmentation failed can then be indicated to the user.
Cardiac MR segmentation algorithms also greatly benefit from the rapid progress in Cardiac MR image acquisition; the scanning protocols are improving, and more and more hospitals have scanners with a magnetic field strength of 3 Tesla. These developments result in images with higher contrast and resolution. The increasing image quality will aid in achieving better segmentation results with the presented methods; therefore, it can be expected that this improved image quality, in combination with knowledge driven algorithms such as the ones developed in this thesis, will enable a robust, fast, and near-fully automatic quantification of cardiac function from MR imaging in the near future.

8

Samenvatting en Conclusies

Either exist as you are or be as you look

8.1 Samenvatting

Cardiovasculaire ziekten komen veel voor in de westerse wereld, en met de toenemende vergrijzing van de bevolking en het toenemende overgewicht stijgt het aantal mensen dat eraan lijdt gestaag. Daarom zal het aantal diagnoses en als gevolg daarvan het aantal beeldacquisities van het hart ook stijgen. Vanwege het grote aantal beelden dat door 3D en 4D beeldvormende technieken zoals CT en MRI wordt gegenereerd, is het handmatig tekenen van de contouren tijdrovend en kost het kwantitatief meten van de hartfunctie veel tijd en aandacht van radiologen en cardiologen. Dit heeft een behoefte gecreëerd voor (semi-) automatische segmentatie methoden om de diagnose te ondersteunen. Dit proefschrift richt zich op de ontwikkeling van dergelijke automatische segmentatiemethoden. In Hoofdstuk 1 zijn de doelstellingen voor dit proefschrift als volgt vastgesteld:

1. Het verbeteren van de lokale segmentatie nauwkeurigheid door middel van nieuwe statistische vormdecomposities
2. Het verbeteren van de segmentatie robuustheid door informatie uit meerdere aanzichten en tijdpunten te integreren in de segmentatie
3. De ontwikkeling van een methode voor tijd-continue segmenatie van de volledige hartcyclus

De volgende paragrafen vatten de hoofdstukken 2 tot en met 6 samen, en onderstrepen dat het in dit proefschrift bescheven onderzoek een aantal methoden heeft opgeleverd, die gelijk aan of beter dan bestaande technieken presteren.
In hoofdstuk 2 is het gebruik van ICA in plaats van PCA onderzocht voor het beschrijven van de statistische variaties in de datasets, zoals die gebruikt worden voor Active Appearance Models. Dit hoofdstuk toont aan dat met ICA lokale vormvariaties verkregen worden, waar PCA in globale vorm-variaties resulteert. Echter, de vectoren die door PCA worden gegenereerd zijn geordend, hetgeen niet het geval is met ICA. Bovendien resulteert PCA in compactere modellen dan ICA. De inherente eigenschap van de PCA methode is dat het richtingen vindt, waarlangs de variantie het grootst is en in dat aspect is PCA optimaal. De eigenvectoren met de hoogste eigenwaarden beschrijven de meest significante vormvariaties, terwijl de lager geordende eigenvectoren ruis beschrijven. ICA daarentegen, maximaliseert de onafhankelijkheid tussen de vectoren en daarom beschrijft elke Independent Component een vrijwel gelijke variantie.
Drie datasets zijn gebruikt om verschillende methoden voor het berekenen en ordenen van de Independent Components te evalueren. De eerste set bestond uit 51 contouren die door experts getekend waren op 2-kamer lange-as MR beelden. De tweede set bestond uit 89 expert-contouren getekend op röntgenbeelden van het linker-ventrikel van het hart. De derde set bestond uit 150 door experts getekende contouren op korte as MR beelden van de linker en rechter ventrikels van het hart. Op deze manier is de ICA methode getest op verschillende vormen en beelden van verschillende modaliteiten. Meerdere algoritmen voor het berekenen

van ICA zijn onderzocht, die allen resulteerden in gelokaliseerde vormvariaties. Echter, kleine verschillen in grootte en positie van de vormvariaties werden geobserveerd. De JADE methode voor het berekenen van de Independent Components is gekozen voor verdere implementatie in het AAM framework, omdat deze methode niet random geïnitialiseerd wordt en robuuste en reproduceerbare resultaten levert. Ook zijn enkele sorteermethoden onderzocht voor de Independent Components, aangezien de IC's intrinsiek niet gesorteerd zijn. De beste manier van sorteren bleek het sorteren op lokaliteit, omdat die resultaten het best overeenkwamen met hetgeen intuïtief verwacht werd. Omdat er geen gouden standaard voor het evalueren van de resultaten bestaat, zijn de resultaten visueel geïnterpreteerd.

In hoofstuk 3 zijn de nauwkeurigheden van de PCA- en ICA-gebaseerde segmentaties voor korte-as MR opnamen van het hart geëvalueerd. De verwachting was dat met ICA wellicht een hogere segmentatie nauwkeurigheid kon worden bewerkstelligd door het lokale karakter van ICA variaties. Om dit te onderzoeken is een dataset bestaande uit 132 routinematig geacquireerde korte-as mid-ventriculaire MR beelden van het linker- en rechterventrikel van 44 patiënten gebruikt voor een kwantitatieve evaluatie. Daarbij zijn 3 beelden van één patient weggelaten en is het model getraind op de overige 129 beelden van 43 patiënten. Het model is vervolgens getest op de geëxcludeerde beelden. Tegen de verwachting in resulteerden beide methoden in vergelijkbare segmentatie resultaten. In het geval van initialisatie op de bekende optimale posities was het PCA-gebaseerde model iets nauwkeuriger. Echter, de verschillen waren statistisch niet significant. Een subspace-analyse, die is uitgevoerd om de vergelijkbare resultaten van de PCA en ICA modellen te verklaren, liet zien dat de vectoren in de overlappende subspace van PCA en ICA nagenoeg dezelfde variantie in de dataset beschrijven als de hoge energie PCA modes. Dit verklaart de vrijwel gelijke segmentatie nauwkeurigheid van beide methoden.

Hoofdstuk 4 illustreert de toegevoegde waarde van ICA boven PCA bij het extraheren van lokale vervormingen. Dit hoofdstuk laat zien dat de ICA gebaseerde infarct herkenning en lokalisatie in korte-as MR beelden een veelbelovende techniek is voor computer gestuurde infarct lokalisatie. Een ICA model is getraind op mid-ventriculaire korte-as MR beelden van 42 gezonde vrijwilligers met behulp van het JADE algoritme. Een kwalitatieve evaluatie is uitgevoerd op MR beelden van 6 infarct-patiënten. Van deze patiënten is ook een delayed-enhancement MRI opname (DE-MRI) gemaakt. De resultaten verkregen met het ICA model zijn visueel vergeleken met de DE-MRI acquisities. Bij de kwalitatieve vergelijking voor 6 patiënten bleek een uitstekende correspondentie tussen de hypo-kinetische regio's, bepaald met behulp van de ICA methode, en de regio's met verhoogde intensiteit in de DE-MRI beelden.

Hoofdstuk 5 beschrijft een automatische analysetechniek voor de bepaling van de globale hartfunctie uit bi-plane lange-as MR beelden. In dit hoofdstuk worden Multiview Active Appearance Modellen geïntroduceerd, die informatie uit verschillende aanzichten en tijdpunten combineren, zodat een robuuste simultane segmentatie wordt verkregen in 2-kamer en 4-kamer aanzichten in eind-diastole en eind-systole

fasen van de hartcyclus. Lange-as MRI acquisities van 59 personen, waaronder patiënten met verschillende hartziekten, zijn gebruikt voor een leave-one-out validatie. Kwantitatieve evaluatie van de werking van het model is uitgevoerd door het vergelijken van de bi-plane area length volumes en ejectie fracties van de automatisch bepaalde contouren en de handmatig getekende contouren. Hierbij zijn twee typen model-initialisaties onderzocht. Initialisatie in alle beelden leverde goede resultaten in meer dan 96% van de gevallen. De afwijkingen tussen handmatig getekende en automatisch bepaalde contouren waren niet statistisch significant. Bij initialisatie in de eind-systole fase alleen, presteerde de Multi-view AAM methode goed in meer dan 92% van de gevallen. Hoewel er meer outliers waren, leidt het initialiseren in eind-systole fasen slechts tot een iets minder nauwkeurig resultaat; echter, hierbij is slechts de helft van de gebruikers-interactie nodig. De nauwkeurigheid van het Multi-view AAM is vergeleken met de variatie in de contouren die door verschillende personen handmatig getekend zijn. Bij initialisatie in alle beelden was de variabiliteit van de voorgestelde methode vergelijkbaar met de interobserver variabiliteit zoals gerapporteerd in de literatuur. Bij initialisatie in eind-systole beelden alleen neemt de afwijking iets toe vanwege het feit dat de initiële posities in de eind-diastole fasen verder verwijderd zijn van de optimale positie. Echter, deze laatste techniek behoeft slechts een minimale interactie van de gebruiker voor de model-initialisatie. De fouten in de bi-plane area length volumes waren niet significant. De gemiddelde fout en de standaardafwijking in de fouten bij de ejectie fracties waren relatief klein vergeleken met de ejectie fracties berekend uit de handmatig getekende contouren. De fouten in de contourposities voor lange-as MR beelden van het hart corresponderen zeer goed met de in de literatuur gepubliceerde waarden.

De analyse van globale hartfunctie met behulp van de in dit hoofdstuk gepresenteerde methode wordt off-line gedaan. Korte-as acquisities worden nog altijd gezien als de gouden standaard voor globale en regionale analyse van het functioneren van het hart. Echter, de methode gepresenteerd in dit hoofdstuk biedt een alternatief om op een snelle manier informatie over het globale functioneren van het hart te verkrijgen, terwijl de patient nog in de MRI scanner ligt. Inclusief alle interactie van de gebruikers, kunnen globale parameters zoals de ejectie fractie, stroke volume en cardiac output verkregen worden binnen 20 seconden, hetgeen een on-line analyse van het globale functioneren van het hart mogelijk maakt. De voorgestelde methode kan gegeneraliseerd worden naar toepassing op korte as MRI acquisities. De combinatie van zowel lange als korte as acquisities zal een optimale quantificatie van de globale en regionale hartfunctie mogelijk maken.

Hoofdstuk 6 beschrijft een op multi-dimensionaal dynamisch programmeren gebaseerde methode voor semi-automatische tijd-continue segmentatie van endocardiale en epicardiale contouren. Het conventionele 2D dynamisch programmeren is uitgebreid naar hogere dimensies en toegepast op 2 substantieel verschillende tracking en segmentatie problemen. Een dataset van 20 studies was beschikbaar voor een kwantitatieve analyse van de voorgestelde methode voor segmentatie van de volledige

hartcyclus. Deze dataset bestond uit korte as MR beelden van het linker-ventrikel van 2 gezonde vrijwilligers en 18 patiënten die gediagnosticeerd waren met verschillende pathologieën. Door experts waren contouren getekend in alle doorsneden en tijdpunten in deze dataset. Bovendien was een fase-contrast aorta flow scan geacquireerd van één patient met een congenitale hartafwijking, zodat de toepasbaarheid van de methode kon worden onderzocht in hoger dimensionale tracking problemen. De segmentatie was succesvol voor alle geïncludeerde beelden en de gemiddelde contour nauwkeurigheid was zeer goed. De automatisch bepaalde eind-diastole en eind-systole volumes lieten een nagenoeg perfecte correlatie zien met de volumes berekend uit handmatig getekende contouren. Bovendien correleerden de ejectie fracties van de automatisch gesegmenteerde en handmatig getekende contouren zeer goed. De afwijkingen tussen de automatisch bepaalde en handmatig berekende volumes en ejectie fracties waren klein en klinisch niet relevant. Het toevoegen van een tijdcontinuïteit randvoorwaarde aan dynamisch programmeren verbeterde de segmentatieresultaten aanzienlijk. Zonder deze randvoorwaarde waren er grote verschillen in de positie van een landmark tussen de opeenvolgende beelden, doordat contourpunten convergeerden naar een foutieve locatie. Het opleggen van een maximale verplaatsing van een contourpunt tussen twee beelden door middel van een tijdcontinuïteits-voorwaarde voorkwam deze fouten. De ontwikkelde methode is daarnaast gebuikt voor het automatisch volgen van de aorta in een tijdserie van beelden. Voor de aorta tracking is 6-dimensionale vormparametrisatie gekozen, en een visuele inspectie liet zien dat een tijdcontinu resultaat hiermede werd bereikt.
Dit voorbeeld illustreert dat er geen theoretische obstakels zijn voor de uitbreiding van deze methode naar meerdere dimensies. Hiermee werd aangetoond dat de beschreven methode toepasbaar is om op een directe manier randvoorwaarden op te leggen gebaseerd op continuiteit in de tijd. Het is een niet-iteratieve methode en het is daarom exact en stabiel. Globale optimaliteit van de oplossing is gegarandeerd met dynamisch programmeren en multi-dimensionaal dynamisch programmeren maakt herkenning van vervormingen in een tijd sequentie en een tijd-continue segmentatie in een serie van beelden mogelijk.

8.2 Conclusies en aanbevelingen

De in dit proefschrift gepresenteerde resultaten representeren een substantiële verbetering van de automatische segmentatie van series van MR beelden van het hart. De doelstellingen die in de inleiding waren gesteld, zijn in grote mate gehaald. Het gebruik van Independent Component Analysis als een alternatieve manier van beschrijven van vormvariaties verbeterde de segmentatie nauwkeurigheid niet, omdat de informatie beschreven door de independent components vergelijkbaar was met de informatie verklaard door de eerste eigenvectoren verkregen met Principal Components Analysis. Echter, het gebruik van ICA maakte automatische lokalisatie en

detectie van infarcten mogelijk. In een kwalitatieve evaluatie bleek ICA veelbelovend in Computer Aided Diagnosis, hoewel verder onderzoek gedaan zal moeten worden naar kwantitatieve resultaten.

Semi-automatische tijd-continue segmentatie van het linker-ventrikel in de volledige hartcyclus is bereikt met behulp van een op multi-dimensionaal dynamisch programmeren gebaseerde methode. Deze methode moet in één fase van de hartcyclus geïnitialiseerd worden, dat wil zeggen dat contouren in alle beelden in deze fase handmatig getekend moeten worden door experts. Volledig automatische segmentatie van de hartcyclus zou mogelijk gemaakt kunnen worden door de Active Appearance Models uit hoofdstuk 5 te combineren met het multi-dimensionaal dynamisch programmeren uit hoofdstuk 6. Zo zou de laatste methode geïnitialiseerd kunnen worden door eerst een segmentatie met een AAM uit te voeren in één fase om contouren in alle vlakken te detecteren. Vervolgens kunnen deze contouren gepropageerd worden naar de andere fasen van de hartcyclus door gebruik te maken van de multi-dimensionaal dynamisch programmeren gebaseerde methode.

Om de robuustheid van het multi-dimensionaal dynamisch programmeren te vergroten, zijn de parameterwaarden voor een optimale werking bepaald voor een grote variëteit van gezonde vrijwilligers en personen gediagnosticeerd met verschillende pathologieën. Analoog aan het trainen van verschillende Active Appearance Modellen voor verschillende pathologieën, zou de segmentatie nauwkeurigheid verbeterd kunnen worden door aparte model parameters te bepalen voor verschillende groepen individuen. Echter, de afname in generaliteit versus de toename van de nauwkeurigheid zal onderzocht moeten worden.

Semi-automatische segmentatie gebaseerd op multi-dimensionaal dynamisch programmeren is toegepast om de contouren van het linker ventrikel van het hart in MR beelden te detecteren. Er zijn echter geen theoretische obstakels om deze methode toe te passen op contourdetectie van het rechter-ventrikel of op beeldseries van andere modaliteiten zoals CT of ultrasound. Verder onderzoek in deze richting zal naar verwachting volledig automatische tijd-continue segmentatie van de hartcyclus mogelijk maken.

In alle automatische segmentatiemethoden kunnen fouten optreden. Bij de Active Appearance Modellen zoals gepresenteerd in Hoofdstuk 5, worden deze fouten gekwantificeerd en gerapporteerd. In elke iteratie genereert het model kunstmatige beelden die lijken op het originele beeld dat gesegmenteerd dient te worden. Gedurende het matchen wordt het verschil tussen het gegenereerde en originele beeld berekend en gebruikt als een maat voor de nauwkeurigheid van de segmentatie. Bij een incorrect segmentatieresultaat komt de waarde van deze foutmaat boven een tevoren bepaalde drempel, hetgeen kan worden gebruikt om een foutieve segmentatie automatisch te identificeren. De beelden waarin de segmentatie niet succesvol is verlopen, kunnen op deze manier ter correctie aan de gebruiker worden voorgelegd. Verder onderzoek is nodig om een vergelijkbare foutendetectie mogelijk te maken in het geval van segmentatie met behulp van multi-dimensionaal dynamisch programmeren. Deze methode is gebaseerd op de optimalisatie van een

kostenfunctie, waar nu de totale waarde van de kostenfunctie over alle vlakken en fasen wordt geoptimaliseerd. Om automatische foutdetectie mogelijk te maken bij deze methode, zou de waarde van de kostenfunctie geëvalueerd en bewaard moeten worden per vlak en fase van de hartcyclus. Op deze manier kan een correlatie tussen het segmentatieresultaat en de waarde van de kostenfunctie per vlak en fase gevonden worden. Analoog aan het AAM, kunnen zo beelden waarin de segmentatie niet als gewenst is verlopen, aan de gebruiker worden voorgelegd.

Algoritmen voor segmentatie van MR beelden van het hart profiteren sterk van de snelle vooruitgang in de MRI acquisitie methoden. Protocollen voor het scannen worden verbeterd en steeds meer ziekenhuizen hebben MRI scanners met een magneetveldsterkte van 3 Tesla. Deze ontwikkelingen resulteren in beelden met een hoger contrast en resolutie. Het ligt in de lijn der verwachting dat de verbeterde beeldkwaliteit in combinatie met kennisgestuurde algoritmen zoals beschreven in dit proefschrift, een robuuste, snelle en vrijwel automatische kwantificatie van de hartfunctie uit MR beelden in de nabije toekomst mogelijk zal maken.

Publications

Peer reviewed papers

M. Üzümcü, R.J. van der Geest, C. Swingen, J.H.C. Reiber, B.P.F. Lelieveldt, "Time Continuous Tracking and Segmentation of Cardiovascular Magnetic Resonance Images using Multidimensional Dynamic Programming", *Investigative Radiology*, 41(1): 52 - 62, 2006.

M. Üzümcü, R.J. van der Geest, M. Sonka, H.J. Lamb, J.H.C. Reiber, B.P.F. Lelieveldt, "Multi-View Active Appearance Models for Simultaneous Segmentation of Cardiac 2- and 4-chamber Long Axis MR Images", *Investigative Radiology*, 40(4): 195 - 203, 2005.

A. Suinesiaputra, **M. Üzümcü**, A.F. Frangi, T.A.M. Kaandorp, J.H.C. Reiber, B.P.F. Lelieveldt, "Extraction of Myocardial Contractility Patterns from Short-Axis MR Images using Independent Component Analysis", MICCAI 2004. Eds: C. Barillot, D.R. Haynor, and P. Hellier. *In: Lecture Notes in Computer Science*, 3216: 737-744, Springer Verlag, Berlin, Germany, 2004.

A. Suinesiaputra, A.F. Frangi, **M. Üzümcü**, J.H.C. Reiber, B.P.F. Lelieveldt, "Detecting Regional Abnormal Cardiac Contraction in Short-Axis MR Images using Independent Component Analysis", Computer Vision Approaches to Medical Image Analysis (CVAMIA) and Mathematical Methods in Biomedical Image Analysis (MMBIA) Workshop 2004, Eds: M. Sonka, I. Kakadiaris, J. Kybic. *In: Lecture Notes in Computer Science*, 3117: 75-86, Springer Verlag, Berlin, Germany, 2004.

M. Üzümcü, A.F. Frangi, M. Sonka, J.H.C. Reiber, B.P.F. Lelieveldt, "ICA vs. PCA Active Appearance Models: Application to cardiac MR Segmentation". MICCAI 2003, Eds: R.E. Ellis, T.M. Peters, *In: Lecture Notes in Computer Science*, 2878: 451-458, Springer Verlag, Berlin, Germany, 2003.

C.R Oost, B.P.F. Lelieveldt, **M. Üzümcü**, H. Lamb, J.H.C. Reiber, M. Sonka, "Multi-View Active Appearance Models: Application to X-ray LV Angiography and Cardiac MRI", Proc. IPMI 2003, *In: Lecture Notes in Computer Science*, 2732: 234-245, Springer Verlag, Berlin, Germany, 2003.

B.P.F. Lelieveldt, **M. Üzümcü**, R.J. van der Geest, J.H.C. Reiber, M. Sonka, "Multi-view Active Appearance Models for Consistent Segmentation of Multiple Standard views: Application to Long and Short-axis Cardiac MR Images", *Computer Assisted Radiology and Surgery (CARS)*, 1256:1141-1146, 2003.

M. Üzümcü, A.F. Frangi, J.H.C. Reiber, B.P.F. Lelieveldt, "Independent Component Analysis in Statistical Shape Models". Medical Imaging 2003: Image Processing, Eds: Milan Sonka, J. Michael Fitzpatrick, *In: Proceedings of SPIE*, 5032:375-383, 2003.

M. Üzümcü, F.M. Vos, A.M. Vossepoel, and G.L. van der Heijde, "Theoretical Analysis of a Spectrophotometric Technique for Measuring Oxygen Saturation in Retinal Vessels". Eds: L.J. van Vliet, J.W.J. Heijnsdijk, T. Kielman, and P.M.W. Knijnenburg, *In: Proceedings of ASCI 2000*, 117-121, 2000.

Abstracts

M. Üzümcü, R.J. van der Geest, J.H.C. Reiber, B.P.F. Lelieveldt, "Time continuous full cycle contour detection in multi-slice multi-phase cardiac MR studies", Eighth Annual SCMR Scientific Sessions (SCMR'05), Society for Cardiovascular Magnetic Resonance, San Francisco, California, USA, 2005.

M. Üzümcü, B.P.F. Lelieveldt, J.G. Bosch, S.C. Mitchell, M. Sonka and J.H.C. Reiber, "Time-Continuous Segmentation of Long- and Short-Axis Cardiac MR Image Sequences using Active Appearance Motion Models", NVPHBV Fall meeting, 2001.

Acknowledgements

This thesis describes the results of research that was performed under supervision of Prof.dr.ir. J.H.C. Reiber and Dr.ir. B.P.F. Lelieveldt at the Division of Image Processing (Laboratorium voor Klinische en Experimentele Beeldverwerking, LKEB), Department of Radiology, Leiden University Medical Center, Leiden, The Netherlands.

Doing a PhD research and writing the thesis has been a period with lots of ups and downs. During this time many people have contributed and supported me in their way and I would like to express my sincere gratitude to them, realizing that it is impossible to mention everyone.

First of all, to Hans van Assen. Hansa, thank you for the great time we had together at the LKEB as colleagues, roommates and friends. For the technical, emotional and entertaining discussions we had during and after work. I have enjoyed our visits to California, Canada, New York and Zaragoza very much. It's amazing that you and Elco Oost succeeded to wake me up at 6 a.m. to watch the sunrise in the Grand Canyon. Elco-san, thank you also for the humor you have spread in our room at the *Poortgebouw*. Mikhail Danilouchkine, Mr. Mike, thank you for your inspiration and motivation. It was fun sharing a room with you and it was even more fun taking a shot at you during the after hours shooting sessions. Julien Milles and Maribel Adame, thank you for being nice colleages and friends and the fun we had together. Avan Suinesiaputra, thank you for the work you did with the use of ICA for detection of cardiac abnormalities.

To Alejandro Frangi, Alex, *muchas gracias* for having me in Zaragoza on multiple research visits. For your great inspiration and ideas and above all thank you for arranging everything for me during my visits. I still have the letter you wrote for me so that I was allowed to park my car at the campus. To Sebastián Ordás, *gracias* for working together on the comparison of AAMs and ASMs and for the good times in Zaragoza. To Salvador Olmos, thank you for introducing me in the subspace analysis and helping me with the implementation of it.

To my brothers Ahmet and Adem, my sister Hatice and my brother in law Süleyman, *teşekkürler* for your love, support and motivation during all these years. *Sizinle gurur duyuyorum*.

To my wife Hayat, *shoukran* for being there for me, for being you and for motivating me to finish the thesis.

Finally, I thank my parents Recep and Selime. Without their unconditional love, unlimited support and encouragement, I wouldn't have succeeded. *Anne ve baba, ne kadar teşekkür etsem azdır; sizlerin sayesinde buralara gelebildim*.

Mehmet Üzümcü
June, 2007

Curriculum Vitae

Mehmet Üzümcü was born in Breda, The Netherlands, in 1976. He graduated from the V.W.O. at the Newman College in Breda in 1994. In the same year, he started his university education at the faculty of Applied Physics of the Delft University of Technology, from which he graduated and received the M.Sc. degree in 2000. His graduation project involved retinal oximetry, i.e. measuring oxygen levels in the retina from digital images. This research was carried out within the Pattern Recognition group of the Delft University of Technology and the Clinical Physics group of the Vrije Universiteit Amsterdam.

From November 2000 until December 2004, Mehmet Üzümcü worked at the Laboratory for Clinical and Experimental Image Processing (LKEB) at the Leiden University Medical Center. He performed research on constrained segmentation of cardiac MR image sequences under supervision of Prof.dr.ir. J.H.C. Reiber, of which the results are presented in this thesis. From January 2005, Mehmet Üzümcü is employed as Senior Physicist in the research and architecture group of Nucletron B.V., Veenendaal, The Netherlands.

His research interests include knowledge-guided, model-based, space and time continuous image segmentation, statistical decomposition methods and computer-aided diagnosis. His current work involves dose calculation and optimization methods in radiation therapy treatment planning.